First-principles study of tungsten trioxide: Structural properties and polaron formation

Hamdi Hanen

A Thesis Submitted for the Degree of Doctor in Sciences

Doctoral School of Physics

University of Liège

Promoter: Philippe GHOSEZ

Septembre 2017

Abstract

Using first-principles calculations, we analyze the structural properties of tungsten trioxide WO_3. Our calculations rely on density functional theory and the use of the B1-WC hybrid functional, which provides very good agreement with experimental data. We show that the hypothetical high-symmetry cubic reference structure combines several ferroelectric and antiferrodistortive (antipolar cation motions, rotations and tilts of oxygen octahedra) structural instabilities. Although the ferroelectric instability is the largest, the instability related to antipolar W motions combines with those associated to oxygen rotations and tilts to produce the biggest energy reduction, yielding a $P2_1/c$ ground state. This non-polar $P2_1/c$ phase is only different from the experimentally reported Pc ground state by the absence of a very tiny additional ferroelectric distortion. The calculations performed on a stoichiometric compound so suggest that the low temperature phase of WO_3 is not intrinsically ferroelectric and that the experimentally observed ferroelectric character might arise from extrinsic defects such as oxygen vacancies. Independently, we also identify never observed $R3m$ and $R3c$ ferroelectric metastable phases with large polarizations and low energies close to the $P2_1/c$ ground state, which makes WO_3 a potential antiferroelectric material. The relative stability of various phases is discussed in terms of the anharmonic couplings between different structural distortions, highlighting a very complex interplay.

On the second hand, the addition of a single electron to the largest supercell of the monoclinic $P2_1/c$ ground state of WO_3 causes the development of a medium polaron inside of this material. We then study and characterize a medium polaron formation in WO_3 from first-principles calculation. We show how the medium polaron in the supercell of WO_3 can change its structural, electronic and dynamical properties.

Résumé

L'oxyde de tungstène (WO_3) est un composé qui a été énormément étudié du fait de la richesse de ses propriétés physiques et de leurs utilisations pour des applications technologiques. En effet, WO_3 est le matériau électrochromique le plus connu grâce à sa capacité de changer de couleur de manière réversible lorsqu'il est soumis à des ondes électromagnétiques ou bien sous l'application d'un champ électrique. Au niveau industriel, les matériaux électrochromiques, dont WO_3 fait partie, sont utilisés principalement dans la fabrication de fentêres à haut rendement énergétique, de verres intelligents, de rétroviseurs anti-reflets, de toits ouvrants, de batteries ou de cristaux photoniques accordables. Il est intéressant de noter que toutes ces propriétés sont liées au dopage et donc directement à la formation de polarons et de bipolarons qui vont influencer les transporteurs de charges. Bien que ce composé ai été largement étudié expérimentalement et théoriquement, il reste encore des questions pertinentes et non résolues concernant les propriétés structurales de WO_3 et la caractérisation des polarons dans WO_{3-x}.

Cette thèse est ainsi dédiée en premier temps, à analyser et comprendre les différentes transitions de phase du WO_3 sur base de calculs ab-initio basés sur la théorie de la fonctionnelle de la densité (DFT) et de reproduire les mesures expérimentales. Plus particulièrement, nous avons montré que WO_3 est un matériau anti-ferroélectrique à l'état fondamental et que c'est possible de le rendre ferroélectrique sous l'application d'un champs électrique. En second temps, nous avons élargi nos précédentes études de WO_3 à l'état pur sans defaut, en explorant théoriquement les effets des lacunes d'oxygène sur les propriétés physiques de WO_3. Nous avons discuté le développement du polaron, qui est due à l'ajout d'un électron extèrieur dans la supercellule de l'état fondamentale de WO_3, en fonction de la taille de la supercellule en utilisant des calculs de premier principe. Nous avons ainsi confirmé des travaux expérimentaux précédents reliés au polaron dans WO_3.

Acknowledgements

I would firstly like to thank Professors Eric Bousquet and Philippe Ghosez without their guidance, support and experience, the work in this thesis would not exist.

I also would like to thank all of the people involved in the collaborative works. In particular, I would like to thank Professor Emilio Artacho for giving me the opportunity to stay in his group at nanoGUNE Cooperative Research Center. I appreciated his cordial welcome and his permanent disponibility for long and fruitful discussions. Thanks to Professor Ekhard K. H. Salje for the fruitful collaboration and accepting to belong to the advising scientific committee of this Ph.D. thesis. I would also like to thank Pablo Aguado for his help and advice throughout my time at nanoGUNE Cooperative Research Center.

I also thank my family and friends for their continued friendship and support. In particular I thank Professor Mohamed Ali Bahri and Dr. Obaid Adami for their support.

I thank also my colleagues at the University of Liège who have helped me with discussion and feedback, Dr. Julien Varignon, Dr. Nicholas Bristowe, Dr. Karan Deep, Dr Thomas Ostler, Dr Nicholas Pike, Dr Bin Xu, Dr Momar Diakhate, Dr. Henu Sharma, Dr. Xu He and Yajun Zhang, to name but a few.

I acknowledge funding from the AVERROES-ERASMUS Mundus project and university of Liège .

Contents

List of Figures

List of Tables

Chapter 1

Introduction

Functional materials play an important role in many technological development challenges. In general, we can find them in all classes of materials such as ceramics, metals, semiconductors, polymers, and organic molecules. They have particular native properties and functions on their own such as ferroelectric, dielectric, piezoelectric, magnetism and energy storage functions. In particular, the perovskite oxides which represent a very large family of composition ABO_3, where A and B are cations, form a unique class of functional materials. They possess typical functionalities that promises important applications. These include, for example, spintronics, magnetoelectricity, multiferroicity and high-temperature superconductivity, many of which are used in various technological applications as magnetoelectronic and spintronic devices, high-sensitivity ac magnetic field sensors and data storage.

The physical and chemical properties of these materials are sensitive to precise processing conditions. A change of environment of the perovskite oxides such as temperature, pressure, electric field, magnetic field and optical wavelength, can effect their functional behaviors.

The physics of the perovskite oxides manifest many aspects which represent an area of interest. The understanding of the fundamental nature of these materials needs a description of their electronic structure and lattice dynamics based on fundamental theories and very basic approximations. Furthermore, the details of the structure of these compounds lead to an improved understanding of their features. Many interesting physical phenomena in the perovskite oxides are essentially driven by the specific features of the corresponding atoms and ions.

Among the large family of the perovskite oxides, tungsten trioxide, WO_3, exhibits perovskite-like structures based on the corner-sharing of WO_6,

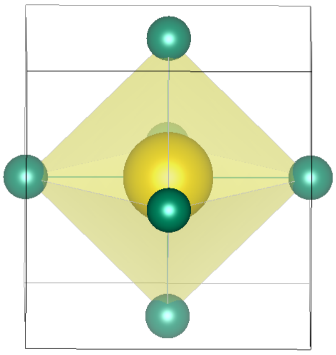

Fig. 1.1: *Cubic structure of WO_3, in which W atom (yellow) is at the center of an octahedra and O atoms (green) are at the corners of this octahedron.*

which offer the advantage of very high structural quality growth. It has been extensively studied due to its very attractive and rich properties for technological applications. WO_3 and its derivatives H_xWO_3 and WO_{3-x} are electrochromic, [13–18] thermochromic, [19, 20] and superconducting. [15, 20–26] It has been envisaged that WO_3 may become one of the best materials for electrochromic applications such as in energy-efficient windows, smart glasses, anti-glare automobile rear-view mirrors, sunroofs, displays, or even tunable photonic crystals [27] and to reduce photocorrosion. [28].

The wide variety of the underlying electronic instabilities for these properties is mirrored by a multitude of related structural instabilities, which were investigated since 1975 [29, 30] and refined later. [1–3, 31–33] All known WO_3 phases are characterized by very large distortions of the archetype perovskite structure so that even the notion of octahedra tilts is to be taken with some caution. The WO_6 octahedra are so largely distorted that the variance of W–O distances in any observed structure is far greater than in most other known perovskite structures. [34–38].

The structural properties of WO_3 can be summarized as follows: it shows no proper melt, surface melting of crystalline material occurs at 1746 K. Crystal growth proceeds typically by sublimation and gas transport at temperatures below 1400K. At the highest temperatures the structures is tetragonal (space group $P4/nmm$) with strong antiferrodistortive (AFD) cation movements so that the WO_6 octahedra are strongly distorted [39] in an anti-polar pattern. Additional rotational octahedral distortions condense in addition to the initial tetragonal displacements when lowering the temperature. They further reduce the symmetry from tetragonal to orthorhombic, monoclinic, triclinic, and finally to a second monoclinic phase. A structural sequence, which contains phases stabilized by temperature, is given in Fig. 1.2 and Fig. 1.3. A monoclinic phase ($P2_1/n$) [2] and a triclinic phase $P\bar{1}$ exist at room temperature. [34, 35]

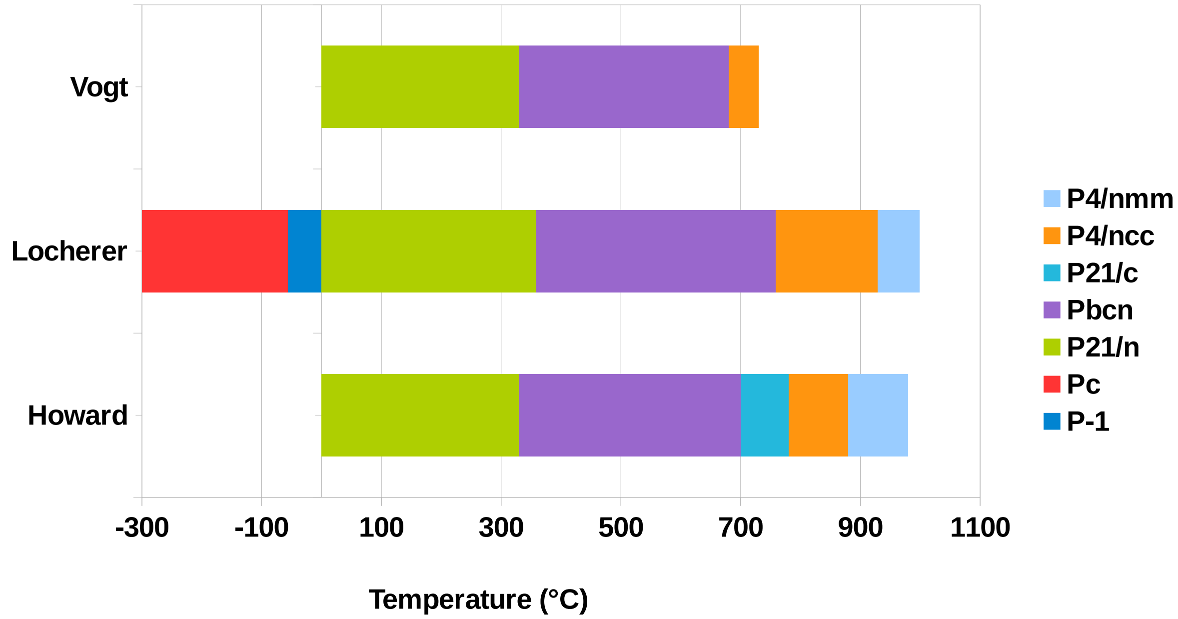

Fig. 1.2: *(Color online) Schematic summary of the temperature phase diagram* WO_3 *as reported by three main experimental sources (Vogt from Ref. [1], Locherer from Ref. [2] and Howard from Ref. [3]*

At higher temperatures, Vogt [1]*et al* and Locherer *et al.* [31] concluded a transition from $Pbcn$ to the $P4/ncc$ phase and Howard [3] observed an intermediate $P2_1/c$ phase. Locherer *et al.* [31] and Woodward *et al.* [36] found an additional transition from $P4/ncc$ to $P4/nmm$ near at 980 K to 1200 K. Below room temperature, Salje *et al.* [32] reported a transition from the triclinic $P\bar{1}$ phase to a polar phase (Pc) with no further transitions down to 5K.

WO_3 occurs (almost) always as oxygen deficient WO_{3-x} with a metal-insulator (MI) transition to a metallic phase for high concentrations of oxygen vacancies or doping with alkali metals. Superconductivity occurs in the metallic phase [21] even if the reduced regions are restricted

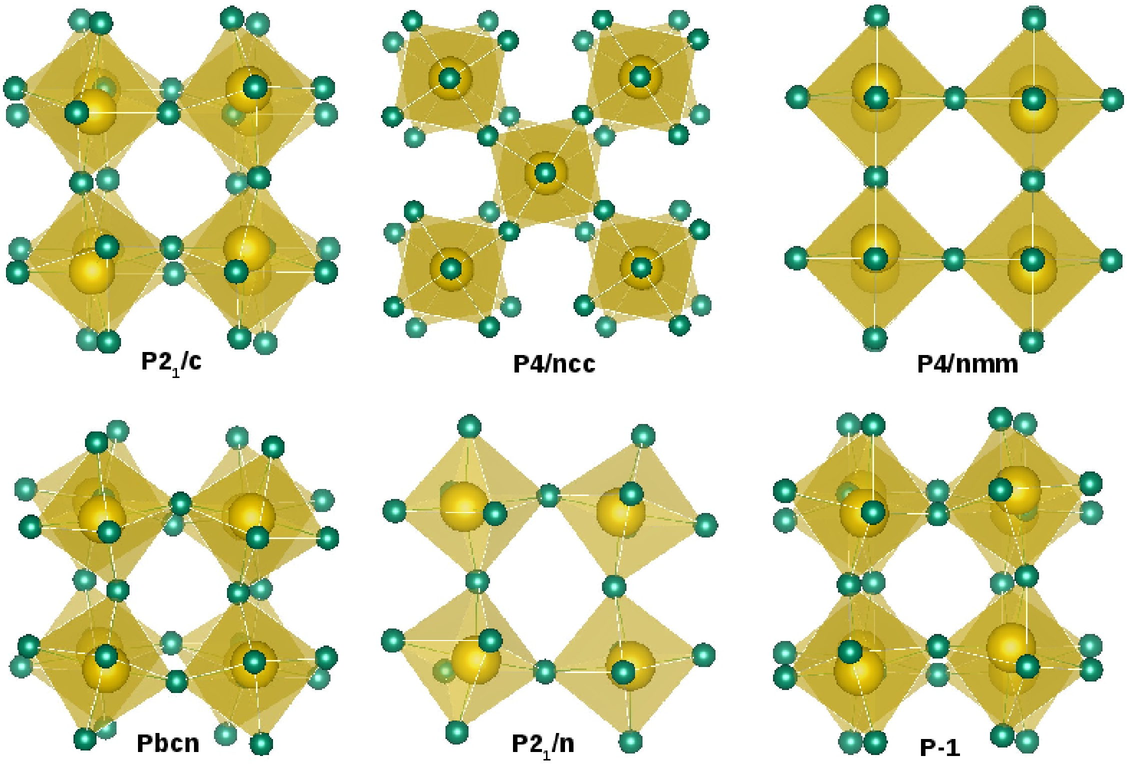

Fig. 1.3: *A structural sequence of WO_3 which shows the octahedral distortions of each phase transiton of this compound*

to nano-scale twin boundaries. Bulk superconductivity in WO_{3-x} was found in a tetragonal phase with space group $P\bar{4}2_1m$. [22]

Despite all the experimental and theoretical investigations of the structural phase transitions of WO_3, a deep microscopic analysis of the phase diagram through the lattice dynamics of WO_3 have been missed. In particular, the ferroelectric ground state of WO_3 has not yet been clearly elucidated. Therefore, it will be important to understand the dynamics behind the main features leading naturally to the notion of structural phase transition and then to the ground state of WO_3.

In this context, our first purpose, will be to present a coherent comprehensive density functional theory (DFT) study of the lattice dynamics, structural and electronic properties of various observed phases of a such technologically important oxide, WO_3. We will discuss the relative stability of these various phases using interaction terms that couple multiple lattice modes. In view of that, we will reveal many new details concerning the structural instabilities of WO_3, which can be derived from a careful analysis of its intrinsic cubic phonon instabilities.

Additionally, we will include alternative low energy structures which have not been experimentally observed. Furthermore, in a discussion where the antiferroelectricity appears as a central concept, we will see that the ferroelectricity is also involved to make $\mathrm{WO_3}$ a potential antiferroelectric material.

The behavior of WO_3 changes when the oxygen deficiencies are involved. The off-stoichiometric WO_{3-x} exhibits a fascinating range of behaviors: from electrochromism [13–18] and thermochromicity, [19, 20]. to high-temperature superconductivity [20, 21, 23–26, 40, 41] and bipolaronic electron transport [42–45]. Hence, the ability to develop such a material requires knowledge from many fields of science and technology. Its potential applications arise from the ability to control its optical properties via an external field or an extrinsic effect [46].

The optical properties of $\mathrm{WO_3}$ can vary significantly due to the presence of oxygen vacancies or doping [47], giving rise to a rich variety of colors, such as, yellow, green and blue [48] and phenomena, e.g. electrochromicity [13] or thermochromicity [19], and thus having a broad range of potential applications that are already mentioned before. Nevertheless, the description of these properties that are due to the presence of the oxygen deficiencies or cation doping in WO_3 are basically assigned to a polaron.

The off-stoichiometric WO_{3-x} plays a key role in the electrochromic phenomena and electrical conductivity of this material. The nonstoichiometric form of WO_{3-x} has been modeled by removing some oxygens from the low symmetry structures of $\mathrm{WO_3}$ in order to elucidate the electrochromic effect. In 2008, Deb [46] suggested for the first time, a model where he associates different charge states to the oxygen vacancy (V_O) depending on the charge transfer of the tungsten(s) pointing towards the defect. Deb associated a 0, +1, and +2 charge state to W^{4+} or $2\mathrm{W}^{5+}$, W^{5+} and W^{6+}, respectively. The 0 charge state is located inside of the the valence band (VB) (0), the +1 charge state is inside the band gap and the +2 charge state is inside the conduction band. Deb thus showed that the energy levels variations associated with these charge states of the oxygen vacancy are involved in the optical transition energy levels, which create a change in the absorption properties of WO_{3-x} and thus in its color. Later, Wang [47] also proposed the same model to explain the electrochromic effect of $\mathrm{WO_3}$ with additional details regarding how to get the different oxidation states of W. They showed, using density functional theory calculations with the Becke-3-Lee-Yang-Parr (B3LYP) hybrid functional (containing 20% of exact exchange), a strong dependence of the crystallographic direction on where the O atom is removed on the W formal oxidation states. Additionally, they observed a semiconductor-to-metal transition by increasing the V_O concentration. In this case, there is a separation between the modified charge states of the tungstens which are located towards the oxygen vacancy and if the two excess electrons are trapped. Recently, N. Bondarenko et al. [49] showed, using the DFT + U and the screened hybrid functional of Heyd, Scuseria, and Ernzerhof (HSE06) (containing 25% of exact exchange), [50, 51] that the formation of the bipolaron in the monoclinic phase WO_3 has two possible configurations W^{5+}-W^{5+} and W^{6+}-W^{4+} which are basically due to either the presence of an oxygen vacancy or doping by lithium atoms (Li). In addition, they also showed that for the Li-doped WO_3 the formation of the W^{5+} polaron and its mobility between different neighboring W sites is possible, whereas the appearance of the W^{4+} state is metastable with the presence of vacancies or is unlikely to form in perfect Li-WO_3. On the other hand, there have been several prior experimental studies on the polaron and bipolarons effect of WO_3, carried out at various experimental methods. Perhaps the most relevant for our study is the work by E.K. H. Salje on the polarons and bipolarons formation in WO_{3-x} [4]. Salje showed the existence of the bipolarons in the Pc phase of WO_{3-x}, which can be photo excited to give two single medium polarons. He then identified and characterized the observed medium polaron by a dominant electron density at the W^{5+} state with the presence of a large probability density away from this specific tungsten. The spread of the trapped electron wavefunction is extended over a two-dimensional layer of the structure of WO_3 which explain the 2D anisotropic shape of the polaron (see Fig. 5.2).

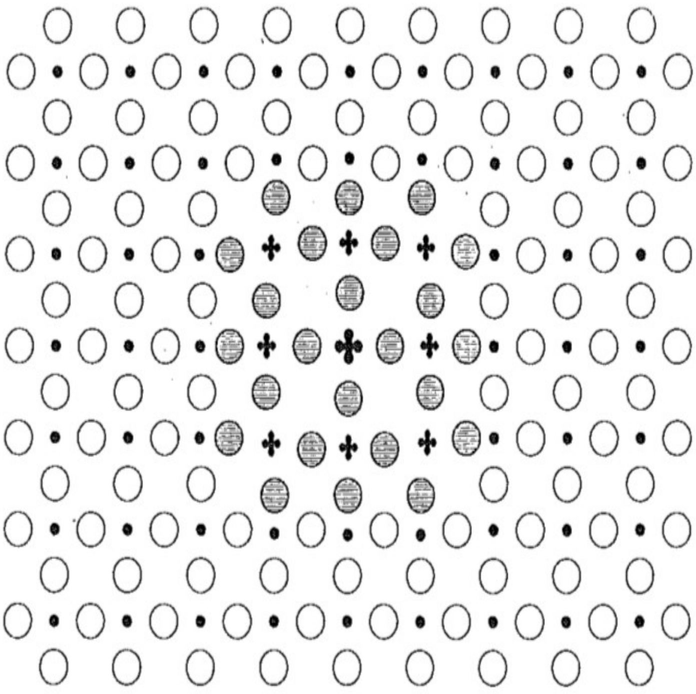

Fig. 1.4: *Sketch of the polaron which extends over 9 tungten sites. Shown is the (ab) plane, the extension of the polaron along the c-axis is one unit cell, ie. the polaron is disc-shaped in the (ab) plane. [4]*

Salje also showed that the formation of polarons of small or intermediate size is specific only for the low temperature ε phase and there is no indication of localized W^{4+} states in this phase. In this context, our second purpose, will be to build on these earlier theoretical and experimental studies for which a deep understanding of the underlying polaron effect of WO_3 from the microscopic origin is still challenging. The analysis and physical notion of a polaron are substantially easier to understand than those of the bipolaron, and they are also essential to understand the physical behavior of the bipolaron, which is generated by an oxygen vacancy. In this thesis, using DFT hybrid functional calculations, we start by analyzing the medium polaron formation process after the injection of one electron in a supercell of the $P2_1/c$ ground state structure of pure WO_3 [5]. We investigate the different possibilities to localize this charge carrier in WO_3, which allows for the development of a medium polaron inside of this compound. We then study and characterize the medium polaron in WO_3. We will show that our simple model calculations including only electronic effects can reproduce some of the physical aspects of the medium polaron behavior experimentally observed in WO_3.

The manuscript is organized as follows: in Chapter 2, we introduce Landau-Devonshire theory as a simple model to describe the phase transitions without much complicated distortions. We also introduce the concept of the soft mode which allows us to describe the structural phase transition as well as we present the properties related to the ferroelectricity. Furthermore, we review the aspects of the fundamental physics of antiferroelectric materials and their properties. In Chapter 3, we describe the theoretical background that has been used to study WO_3. This includes; DFT theory with a special emphasis on the hybrid functional approach, the generic technical details used in the calculations and the tools for symmetric mode analysis. From these general considerations, we present in Chapter 4, the results obtained from our DFT calculations using the hybrid functional B1WC of WO_3. We elucidate the crystal structures and lattice dynamics of WO_3 and, thus, we explore the lattice mode contributions to the phase stability of various polymorphs, and we discuss the properties of each crystal structure of WO_3. In Chapter 5, we study and characterize a polaron formation in WO_3 from first-principles calculation by adding a single electron in a supercell of the monoclinic P2_1/c ground state structure of WO_3 and find a self-trapping of this electron on a few d-orbitals of W, which distorts the crystal structure. In Chapter 6, we conclude this present thesis with a summary of what we have been achieved, highlighting the main contributions. We will put the work into a broader perspective and we will discuss future avenues.

Chapter 2

Crystal Properties and Physics related to WO_3

2.1 Introduction

The description of WO_3 phase transtions needs to introduce the concept of the Landau theory, which provide an explanation of a any system's equilibrium behavior during the process of a structural phase transition. In fact, to analyze the symmetry transformation induced during the process of the phase transition, in 1937, Laudau proposed a phenomenological expression for the free energy of any system as a function of an internal variable of this system. Furthermore the Landau theory is considered as one of the basic theoretical tool for describing and understanding the nature of the phase transitions as a function of a physical quantity which is called the order parameter (OP). This OP should be zero in the highest symmetry phase and non-zero at the phase transition. Therefore, we can determine the equations of the system state by constructing a Landau free energy F as a power series of the order parameter in the vicinity of the transition.

2.2 Landau-Devonshire theory of phase transition

The occurrence of phase transitions between equilibrium states can be driven by many parameters such as temperature, pressure, chemical composition, magnetic or electric field, etc. In particular, for crystal phase transition, the space-group symmetry of the high and low-symmetry phases usually exhibits a group-subgroup relationship. The Landau-free-energy should be invariant by all the symmetry transformations constituting the space group of the high symmetry phase for which we have to keep only the even power of the order parameter in the Taylor expansion of the free-energy, such as:

$$F(\psi,T) = A\psi^2 + B\psi^4 + C\psi^6 + ... \tag{2.2.1}$$

in which ψ is the order parameter that can be macroscopic or microscopic quantity (that can be a thermodynamic quantity). The coefficients of the series-expansion terms of F(ψ,T) can be determined from experiment or from first-principles calculations. From the thermodynamic approach, the free energy is the Gibbs free energy (G) with free mechanical boundary conditions (σ) and with an external field (E) such as :

$$G = U - TS - \eta\sigma - ED = F - \eta\sigma - ED \tag{2.2.2}$$

with σ=0 and E=0, we get

$$F = U - TS$$

Where T is the temperature, S the entropy and U the internal energy. To get a thermal equilibrium (stable phase), the order parameter must minimizes the free energy.

2.2.1 Second order phase transition

Laudau theory is an approach that describe and allow to analyze the equilibrium behavior of a system near the phase transition. The phenomenological expression for the free energy as a Taylor expansion in the order parameter is written as follows:

$$F(\psi) = \frac{1}{2}a\psi^2 + \frac{1}{4}b\psi^4 \tag{2.2.3}$$

where we have truncated the power series at fourth term. Here the coefficient a depends on the temperature and is given by to the Landau-Devonshire theory:

$$a = a_0(T - T_0)$$

T_0 is the temperature where the phase transition occurs with a non-zero value of the order parameter. The other coefficients in the free-energy expansion are independent of temperature. Therefore, the general expression of the free-energy up to the 4th order is :

$$F(\psi) = \frac{1}{2}a_0(T - T_0)\psi^2 + \frac{1}{4}b\psi^4 \tag{2.2.4}$$

For the second order phase transition, the existence of a minimum of F for finite values of order parameter is ensured by the positive sign of the quadratic coefficient b>0. The minimum of F, above and below T_0 occurs at:

$$\psi = 0 \quad , for \quad T > T_0 \tag{2.2.5}$$

$$\psi^0 = [\frac{a_0}{b}(T_0 - T)]^{1/2} \quad , for \quad T < T_0 \tag{2.2.6}$$

The variations of F(ψ) and the OP around the vicinity of T_0 are sketched in Fig. 2.1. Below T_0, F(ψ) is minimized at +/- ψ^0 and the OP has a square-root temperature dependence as a function of $(T_0 - T)$ where we can see that the OP will increase with decreasing temperature from T= T_0 to T=0 K. In this case, the OP varies continuously from T_0. When T> T_0 or T= T_0, the free-energy is shown as a single well as a function of the OP that is the sign of a paraelectric material.

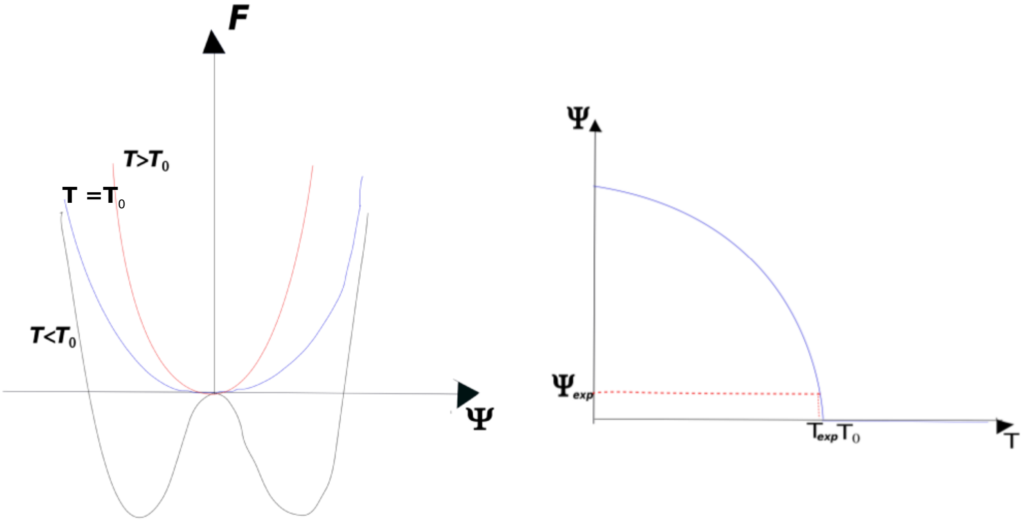

Fig. 2.1: *Second-order phase transition. (***a***) Free energy as a function of the order parameter at* $T>T_0$, $T=T_0$ *and* $T<T_0$; *(b) Order parameter* ψ^0 *as a function of temperature*

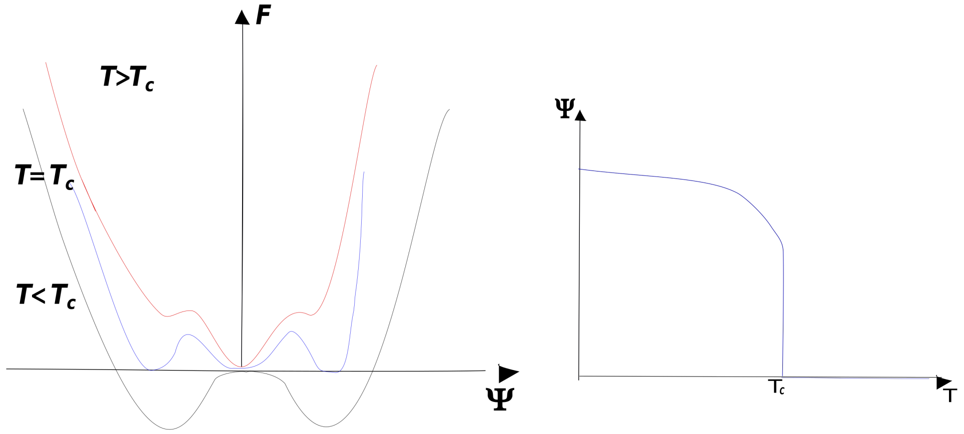

Fig. 2.2: *First-order phase transition.* (**a**) *Free energy as a function of the order parameter at T> T_0, T=T_0 and T< T_0; (b) Order parameter ψ^0 as a function of temperature*

On the other hand, we can also calculate other properties for the second-order phase transition from the free energy:

$$\begin{aligned} F &= U - TS \Rightarrow U = -\frac{1}{2} a T_c \psi^2 + \frac{1}{4}\psi^4 && (2.2.7) \\ \Rightarrow & \qquad S = -\frac{1}{2} a \psi^2 && (2.2.8) \end{aligned}$$

We assume that the internal energy U is independent of temperature. The entropy S is a quadratic function of the order parameter, it will decrease with decreasing temperature. The dielectric susceptibility χ is obtained from the second-order differential of the free-energy with respect to the order parameter:

$$\chi^{-1} = \frac{\partial^2 F}{\partial \psi^2} = a(T - T_0) + b\psi^2 \qquad (2.2.9)$$

When T<T_0,ψ=0 and

$$\chi^{-1} = \frac{\partial^2 F}{\partial \psi^2} = a(T_0 - T) \tag{2.2.10}$$

For T>T_0,

$$\chi^{-1} = 2a(T_0 - T) \tag{2.2.11}$$

The dielectric susceptibility χ diverges at the phase transition (T⟶ T_0) (see Fig. 2.3)

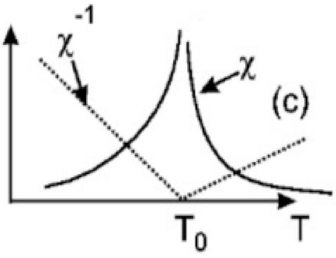

Fig. 2.3: *Dielectric susceptibility χ of the second-order phase transition and its inverse as a function of temperature.*

2.2.2 First order phase transition

For the first order phase transition, the Landau-free-energy expansion will be up the sixth order, such as:

$$F(\psi) = \frac{1}{2}a\psi^2 + \frac{1}{4}b\psi^4 + \frac{1}{6}c\psi^6 \tag{2.2.12}$$

where the quartic coefficient b is negative. The variations of F(ψ) are sketched in Fig. 2.2 from which we can see that the free energy have a minimum at nonzero OP above the transition temperature T_c. For these type of phase transition a special critical point should be found (the so-called Landau Curie point) that corresponds to the discontinuous jump of the order-parameter. This temperature is not the same than the transition temperature T_0 for the second order phase transition in the sense that for any temperature between T_c and T_o the free energy has a local minimum for a zero OP. Since anharmonic effects play a crucial role in the softening process. In this case the critical temperature is given as folows:

$$T_c = T_0 + \frac{3b^2}{16ac}, \tag{2.2.13}$$

and the internal energy at this temperature is written as :

$$U = \frac{aT_c\psi^2}{2} \tag{2.2.14}$$

On the other hand, the dielectric susceptibility is different from the standard Curie-Weiss law provided by the second-order transition at the transition temperature T_c :

$$\chi = \frac{1}{a}(T - T_0) \quad for \quad T > T_c \tag{2.2.15a}$$

$$\chi = \frac{16c}{3b^2} \quad for \quad T = T_c \tag{2.2.15b}$$

$$\chi = \frac{1}{a} + 3b\psi^2 + 5c\psi^4 for \quad T < T_c \tag{2.2.15c}$$

This variation is sketched in Figure 2.4.

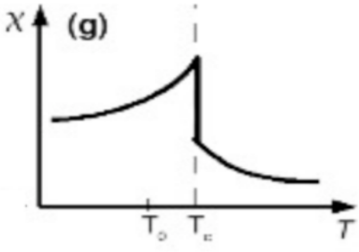

Fig. 2.4: *Dielectric susceptibility* χ *of the first-order phase transition and its inverse as a function of temperature*

2.3 Soft modes

The concept of the soft phonon mode comes from the description of the lattice dynamical mode with anomalously frequency at the Curie point. This particular mode, which is characterized by its eigenvector and frequency, has an anomalous behavior around the structural phase transition of the crystal. Such modes trigger a lattice instability, leading to a structural phase transition either of second or first order. In the second-order transition, the soft frequency actually vanishes at the transition point. However, for the first-order transition, the change of phase occurs before the mode frequency is able to go to zero. When the normal vibrational mode (phonon) of the crystal becomes unstable, that is, whose normal frequency tends to zero as $T \longrightarrow T_0$. On the other hand, in 1954, Born and Huang [52] established that a crystal lattice will become unstable if one of its normal-mode frequencies becomes purely imaginary. Since an anharmonic effects play a crucial role in the softening process, we can then understand the origin of the temperature dependence of the soft mode frequency as:

$$\omega^2 = \omega_o^2 + \frac{k_B/2}{\sum_{k',\nu'} \alpha^{(4)}_{k',\nu'}/\omega^2(k',\nu')} \tag{2.3.1}$$

Where ω_o^2 is the harmonic value that we calculate in the lattice dynamics calculation and $\alpha^{(4)}_{k',\nu'}$ is the coefficient of the fourth-order anharmonic interaction that couples the soft mode to a phonon of wave vector mode $\nu^{'}$ $k^{'}$ and angular frequency $\omega(k^{'},\nu^{'})$. If $\alpha^{(4)}$ is positive, ω^2 increases until it becomes positive when the temperature increases. At the transition temperature $T=T_c$ in which $\omega^2=0$, we can deduce from the Eq.(1.15) that:

$$T_c = \frac{-2\omega^2/k_b}{\sum_{k',\nu'} \alpha^{(4)}_{k',\nu'}/\omega^2(k',\nu')} \tag{2.3.2}$$

Therefore we can write the temperature dependence of the soft mode as:

$$\omega^2 = \frac{|\omega_0^2|}{T_c}(T - T_c) \tag{2.3.3}$$

The variations of the square frequency is sketched in figure 2.5

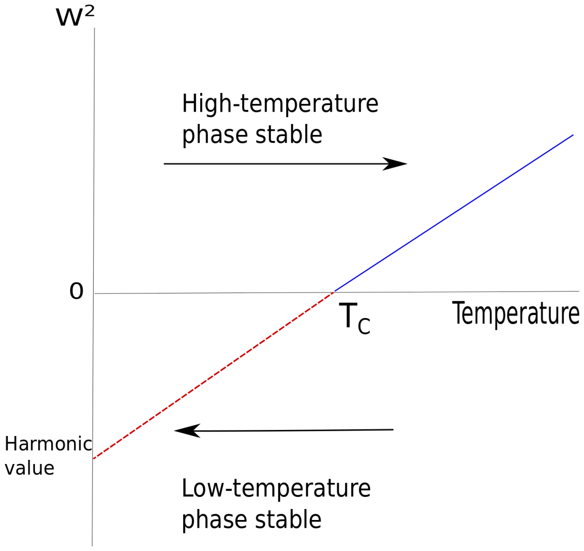

Fig. 2.5: *Schematic representation of the temperature dependence of the square of the frequency of the soft mode. Below the temperature Tc the frequency is imaginary and hence unstable. The frequency at T=O K is the harmonic value*

2.4 Phonon instabilities

The microscopic origin of the structural instabilities of the crystal is mainly related to the vibration of certain normal modes in the high symmetry cubic structure. In particle, the appearance of the ferroelectric phase transition when the temperature is lowered, is mainly due to the softening of a transverse optical (TO) polar zone-center mode during the process of the transformation as explained by Cochan [53]. The soft mode is main characterized by its low frequency. Therefore, we can associated the structural instability to the lattice dynamics. Within, the harmonic approximation, the dynamical equation can be written as:

$$\sum \tilde{D}_{\kappa\alpha,\kappa'\beta}(\boldsymbol{q})\gamma_{m\boldsymbol{q}}(\kappa'\beta) = \omega^2_{m\boldsymbol{q}}\gamma_{(\kappa\alpha)}, \tag{2.4.1}$$

where α and β label the directions, $\omega^2_{m\boldsymbol{q}}$ is the phonon frequency of the mode m at wave vector $\boldsymbol{q}$, $\gamma(\kappa\alpha)$ its associated phonon eigenvector related to the phonon eigendisplacement $\eta_{m\boldsymbol{q}} = \sqrt{M}\gamma_{m\boldsymbol{q}}$ and $\tilde{D}_{\kappa\alpha,\kappa'\beta}$ the dynamical matrix. The dynamical matrix is defined as:

$$\tilde{D}_{\kappa\alpha,\kappa'\beta}(\boldsymbol{q}) = \tilde{C}_{\kappa\alpha,\kappa'\beta}(\boldsymbol{q})/\sqrt{M_\kappa M_{kappa'}}, \tag{2.4.2}$$

where M_κ is the mass of the atom κ and $\tilde{C}_{\kappa\alpha,\kappa'\beta}$ is the Fourier transform of the interatomic force constant (IFC) in real space [54]:

$$\tilde{C}_{\kappa\alpha,\kappa'\beta}(l,l') = \frac{\delta^2 E}{\delta\tau_{\kappa,\alpha}(l)\delta\tau_{\kappa',\beta}(l')} \tag{2.4.3}$$

where l and l' label the unit cell, κ and κ' label the atoms, τ their displacements, while α and β label the directions in which the atoms are displaced.

2.5 Ferroelectricity

The connection between structural distortions and ferroelectricity in the perovskite family of materials is basically the symmetry arguments. The polar displacements of cation and anion sublattices against one another break the symmetry of the perfect high-temperature cubic structure and induces a spontaneous electric polarization. However, for ferroelectricity it must be possible to switch the polarization under an applied an electric field. From the side of the reciprocal space, the ferroelectricity is the result of a polar instability at the Brillouin-zone center in which the cations uniformly move against the oxygen octahedron, which is sketched in Figure 2.6.

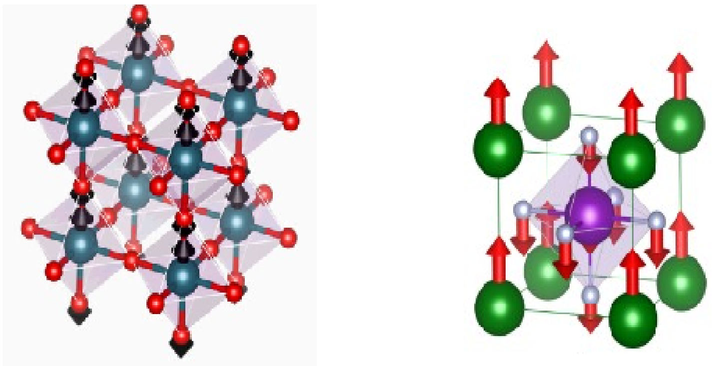

Fig. 2.6: *Schematic view of the polar mode contributing to the distortions of* WO_3 *(left part of the image) [5] and* $NaMnF_3$ *(right part of the image) [6]. Small red and white spheres represent the oxygens and the fluorides, respectively. The large blue, purple and green spheres represent the tungsten, Manganese, and Sodium atoms, respectively.*

2.6 Symmetry-mode analysis of the distorted phases

The study of phase transitions brings together issues of crystal structures, symmetry, bonding, thermodynamics, and lattice dynamics. In particular, the displacive phase transitions associated to the perovskites materials could involve ferroelectric distortions, antiferrodistortive distortions, rotations, and tilts of oxygen octahedra. Therefore, a symmetry-mode analysis of any distorted structure of displacive type leads to understand some interesting physical properties, such as the ferroelectricity and antiferroelectricity. This analysis consists in decomposing the symmetry-breaking distortion present on the distorted structure into contributions from different symmetry-adapted modes. A special software known as AMPLIMODES was created to perform a meaning symmetry-mode analysis of a distorted structure. In fact, during the process of the displacive phase transition the higher symmetry crystal structure of the last phase is a distorted form of the higher symmetry crystal structure of the previous one (parent phase), in which its symmetry is lowered by small displacement of some of the atoms. Thus, given the high- and the low-symmetry structure, AMPLIMODES (see Ref. [55]) finds the atomic displacements that related them, defines a basis of symmetry-adapted modes, and calculates the amplitudes and polarization vectors of the distortions modes of different symmetry frozen in the structure. These distortions modes could be unstable in the parent high-symmetry configuration and are essential for justifying the stability of the distorted structure. We call such modes primary modes because we can find in the same distorted structure an other type of modes that are consider as a secondary modes, which are allowed by symmetry and have a less importance than the primary modes. These secondary modes appear through linear coupling with the primary modes.

The symmetry-mode analysis separates the contributions of the different symmetry modes in a structural distortion. This needs, first, to determine a basis of symmetry modes of the parent phase compatible with the low-symmetry phase, then to decompose the structural distortion as a sum of the contributions of all of them. A group-subgroup relation should exists between the space groups of the parent and observed structures, and the structural distortion that related them.

2.7 Antiferroelectricity

Some of the functional oxides exhibit a variety of interesting physical properties, such as: ferromagnetism, ferroelectricity and multiferroic properties. The antiferroic materials can also exhibit characteristic functional behavior in applied macroscopic field. The antiferroelectric crystal are characterized by an antipolar crystal structure with related ferroelectric polar structure at low free energy. An earlier study of antiferroelectric perovskite oxide, reported by Shirane [7, 10], shows the competition between ferroelectric and antiferroelectric phases is an intrinsic feature of antiferroelectrics.

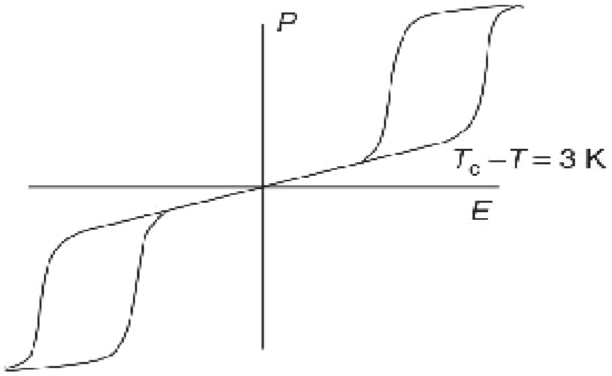

Fig. 2.7: *Double hysteresis loop for* $PbZrO_3$ *, as redrawn in Refs. [7, 8]*

The appearance of a ferroelectric phase through a first-order boundary in the phase diagram is an important indication of antiferroelectricity. The main characteristic property coming from the low-free-energy difference is the electronic-field-induced transition from the antiferroelectric to the ferroelectric state in a double hysteresis loop (see figure 2.7). The application related to this functionality of the antiferroelectric materials are: high energy storage capacitors, electrocaloric refrigerators, high-strain actuators and traducers.

2.7.1 Definition and Characteristic Properties

In the standard reference book by Lines and Glass [56], an antiferroelectric is attained by condensation of a nonpolar lattice mode that " exhibit large dielectric anomalies near to the transition temperature and that can be transformed to an induced ferroelectric phase by the application of an electric field ". In the recent overview article of Landolt and Bornstein [57], the concept of antiferroelectricity is based not only on the crystal structure but also on the dielectric behavior of the crystal. On the other hand a ferroelectric crystal is defined as a crystal that shows an electric polarization, whose direction can be reversed by an electric field. The antiferroelectric crystal is defined as a crystal whose structure can be considered as being composed of two sublattices polarized in antiparallel directions and in which a ferroelectric phase can be induced by applying an electric field. These two definitions of ferroelectrics and antiferroelectrics are often extended to include the possibility that the transition temperature is above the decomposition temperature of the material, or that the critical electric field is above the breakdown field of the material. The antiferroelectric can be described by unit cells with oppositely directed dipoles generated by ionic displacements from a higher symmetry reference structure as shown in figures 2.8

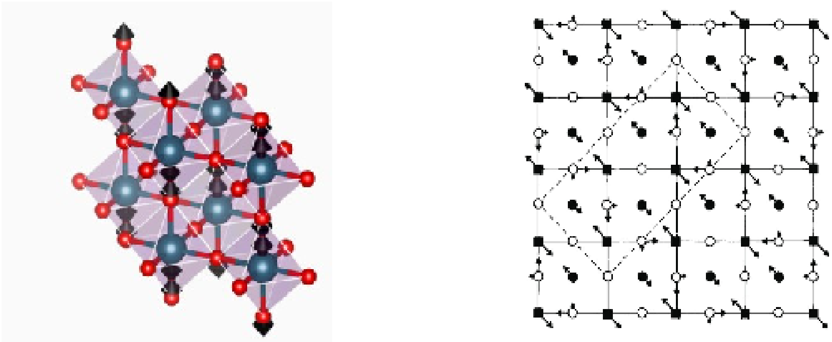

Fig. 2.8: *The left side represents a schematic view of the antipolar mode contributing to the distortions of* WO_3. *[5] Small red spheres represent the oxygens and large blue spheres represent the tungsten atoms. The right side represents the projection of antipolar atomic displacements associated with the* $\sum_2$ *mode at* $q = 2\pi a\ (1/4, 1/4, 0)$ *onto the ab-plane. Squares and circles indicate Pb and oxygen atoms, respectively. Filled and open circles show atoms on the Pb atomic layer and atoms on the Zr atomic layer. [9]*

2.7.2 Landau energy functional formulation

The Landau energy can describe the importance of both structural and energetic aspects of the definition of antiferroelectrics. Kittel [58] has shown the main characteristic properties of antiferroelectrics by introducing the free energy expression:

$$A(P_a, P_b, T) = A_o + f(P_0^2 + P_b^2) + gP_aP_b + h(P_a^4 + P_b^4 + j(P_a^6 + P_b) - (P_a + P_b)E \quad (2.7.1)$$

Where P$_a$ and P$_b$ is the polarization of the two sublattices, and E is the electric field, with g $>$ 0 favoring the antipolar alignment of the two sublattice. This can be transformed into a Landau functional:

$$G_1(P_F, P_A, T) = (1/2)(f+g/2)P_F^2 + (1/2)(f-g/2)P_A^2 + (h/8)(P_F^4 + 6P_A^2P_F^2 + P_A^4) + P_FE \quad (2.7.2)$$

where P$_F$ $= P_a + P_b$ is the macroscopic polarization, and P$_A$ $= P_a - P_b$ is the staggered polarization. The quadratic coefficients depend on the temperature as f(T)=g/2+$\lambda(T - T_c)$, so the quadratic coefficient of P$_A$ vanishes at T$_c$, and $\lambda > 0$ correspond to a low-temperature antiferroelectric phase. The temperature dependences of the quadratic terms in P$_A$ and P$_F$ are linked. The transition can be first or second order depending on the choice of the parameters. For the second order transition, h>0 and the sixth-order terms can be neglected. At T=T$_c$ there is a phase transition from the high-temperature phase to the antiferroelectric phase, below this transition temperature T$_c$ the spontaneous polarization of the sublattices P$_A$ becomes nonzero. The dielectric constant depends on the temperature has its maximum at the Curie temperature and changes slope slightly. For a first order transition, h< 0 and j>0, the sublattice polarization will be discontinuous, same for the dielectric constant at the paraelectric-antiferroelectric transition. [11]

2.7.3 Microscopic Origins of Macroscopic behavior

To connect the macroscopic behavior to microscopic aspect of the crystal structure and energetics of antiferroelectric materilas, we can start by considering simple microscopic model in which we have re-orientable localized electric dipoles on a bipartite lattice, so that the lattice sites can be divided into two sublattices, with each site being neighbored by sites in the other sublattice. The single and the next-nearest-neighbors dipole-dipole interactions favoring anti-alignment and stabilize sublattice polarization give the characteristic hysteresis loop with a jump in polarization from the antiferroelectric state to field-induced ferroelectric state. On the other hand, we can also make macroscopic-microscopic connection through the soft mode theory. On the beginning, we identify the lattice modes of definite symmetry in the structure of the antiferroelectric phase relative to a high-symmetry reference structure, and then we can write the expansion of Landau energy in symmetry invariants [59]. The Kittel-type antiferroelectric model is characterized by a single lattice mode in which the ions involved are divided into two groups with equal and opposite displacements. The wave vector is expected to be at the zone boundary, doubling the unit cell. Moreover, the antiferroelectric phase can be described by a group of coupled modes [60], with a primary unstable antipolar mode accompanied by other distortions such as oxygen octahedron rotation to which coupling is symmetry-allowed, lowering the energy of the phase. As described before, to get an antiferroelectric phase we have to find a low-energy alternative ferroelectric phase, where its distortions come from the same high-symmetry reference structure. This condition of antiferroelectricity provides a small energy difference that will be easy the make the transformation between the two phases via the application of an electric field. The ferroelectric phase can be generated by more general zone-center polar mode and may be accompanied by other modes that are observed to be present in the low-energy alternative ferroelectric phase.

For example, lead zirconate ($PbZrO_3$) is known as a typical antiferroelectric material because of its antiferroelectric grounds state. Moreover, an intermediate ferroelectric phase have been observed between the paraelectric and the antiferroelectric phase. Figure 2.9, shows the existence of the free energy curve of the ferroelectric phase which lies above that of the antiferroelectric phase. An other antiferroelectric phase appears with free energy also very adjacent to that of the original antiferroelectric phase and we can see also that the free energy of the ferroelectric phase is very close to that of the other antiferroelectric phase. By the application of an external field on $PbZrO_3$ a double hysteresis starts to appear only above a critical E_c field. We can see that when the external field increases beyond E_c, the ferroelectric state may become more stable than the antiferroelectric one. Such a situation should be realized if the the free energy curves for $PbZrO_3$ have characteristics as shown in figure 2.9 . Therefore, the free energy of the ferroelectric state, if we compare with those of the antiferroelectric and the paraelectric ones, must be lowered considerably.

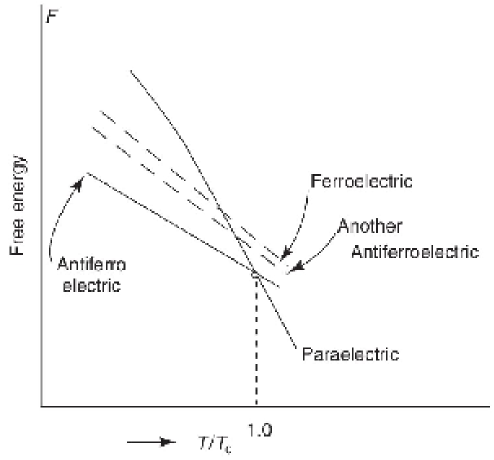

Fig. 2.9: *Schematic free energy curves for antiferroelectric $PbZrO_3$, showing the presence of a low-free-energy alternative ferroelectric phase. (Source: From Ref [10])*

2.7.4 Antiferroelectric materials: Structure and Properties

Untel recently, the most thoroughly studied antiferroelectric oxide is on $\mathrm{PbZrO_3}$. $\mathrm{PbZrO_3}$ has a paraelectric cubic ideal perovskite at high temperature and at a temperature below Tc=505 K, the structure is antiferroelectric orthorhombic phase distorted perovskite structure Pbam [61]. An intermediate ferroelectric rhombohedral R3m phase with electric polarization along [111] have been observed in a very narrow temperature range separating the antiferroelectric and ferroelectric phases [62].

The estimation of the critical electric field required to stabilize the polar phase is $\mathcal{E}_c \sim \Delta E/\Omega_0 P_s$, where ΔE is the energy difference between the two phases. In the recent study of $\mathrm{PbZrO_3}$ [63], depends on which approach that has been used in density functional theory (DFT) calculation, two polars phases R3c and R3m have been found with a small energy difference between them and the Pbam anitpolar phase. With the local-density approximations (LDA) approach, the R3c structure was the polar phase with small energy difference 7

Table 2.1: *Gain energies, polarizations, Volumes and Electric fields for PbZrO3, ZrO2 and WO3*

Material	$PbZrO_3$	ZrO_2	WO_3
Approach	LDA	LDA	Hybrid (BW1C)
FE phase	R3c	Pca2_1	R3m
AFE phase	Pbam	Aba2	P2_1/c
Gain energy (meV/f.u)	7	35	11.43
Polarization(μCcm^{-2})	66.01	36	69
Volume (Å^3)	70.89	32.9	55
Electric field (kV/cm)	239	470	480
Reference	[63]	[63]	[5]
Material	$PbZrO_3$	ZrO_2	WO_3
Approach	GGA-WC		Hybrid (BW1C)
FE phase	R3m		R3c
AFE phase	Pbam		P2_1/c
Gain energy (meV/f.u)	24		14.93
Polarization(μCcm^{-2})	75		71
Volume (Å^3)			52.71
Electric field (kV/cm)	707		638
Reference	[63]		[5]

meV/f.u with respect to the Pbam antipolar phase. To stabilize the R3c phase by applying an electric field from the Pbam antipolar phase, we need 239 kV/cm electric field. In addition, the Generalized gradient approximation (GGA-WC) approach provides the R3m structure as the polar phase with energy difference 24 mev/f.u with respect to the Pbam antipolar phase. Therefore, the transformation between the two phases R3m and Pbam will be via the application of an electric field with 707 meV/cm.

For tungsten oxide WO_3, we have found also two polar phases R3c and R3m with energy slightly above the energy of the antipolar phase P2_1/c, that is the ground state of this compound. The lower energy difference is between the R3m and the P2_1/c phase 11.43 meV/f.u, such as we need 480 meV/f.u electric field to make the transformation between the two phases. For the R3c phase, the energy difference is 14.93 meV/f.u bigger than the R3m phase, then the electric field is 638 meV/f.u.

For ZrO_2, the antipolar phase is Aba2 structure and the polar one is Pca2_1 structure, the energy difference between the two phases is 35 meV/f.u which required to apply 480 kV/cm electric field to make the transformation between these phases.

2.7.5 Analogy between Antiferroelectric and Ferroelectric material

A ferroelectric material is an insulating crystal characterized by a switchable macroscopic polarization P. Indeed, at a given temperature T=T_c, an off-center displacement of the B (coming from ABO_3 perovskite family) cation breaks the centersymmetry structure to generate, in each cell, an electric dipole that makes the spontaneous polarization P. The opposite direction off-center displacement of the B cation will leave the structure unchanged with an spontaneous polarization -P, this means that the free energy of the crystal is invariant by this inversion of the spontaneous polarization. To illustrate this characteristic behavior of ferroelectric materials, from the DFT theoretical point view, a double well of free energy with respect to the spontaneous polarization have been performed to emphasize the switchability of the polarization in the ferroelectric materials (see Figure 2.10).

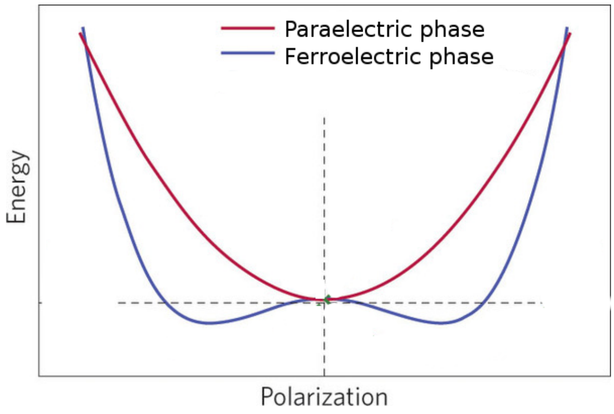

Fig. 2.10: *Illustration of the energy double-well of the ferroelectric phase.*

However, all practical measurement of ferroelectric materials exploit the switchability of the polarization. In fact, when all of the dipole moments are aligned, the ferroelectric material is considered saturated since an increase in applied voltage will not increase the polarization. Furthermore, if the applied voltage is reduced from its maximum positive value to zero, some dipole moments will remain aligned and a remanent polarization is observed which is only the spontaneous polarization. Therefore, the application of a sufficiently strong coercive electric field is still necessary to switch the polarization from P to -P. These two polarizations that are equal in modulus and point along equivalent symmetry directions correspond to the polarization of two enantiomorphic structures. As a practical matter, the magnitude of the spontaneous polarization is defined as the half of the polarization difference between the two ones of the enantiomorphic structures. The transformation between the two enantiomorphic structures polarization is driven by the coercive electric field and that finally provides an hysteresis cycle as experimental output. On the hand, for the antiferroelectric materials, we can consider the Kitel model (as described in the previous subsection), in which the global lattice of the crystal was devised between two sublattices that both have the same magnitude of spontaneous polarization but with opposite directions. By analogy to the definition for a ferroelectric phase, an antiferroelectric phase is obtained through an opposite off-center displacement of the B cation in each sublattices that breaks the centerosymmetry phase of the global structure. However, the total spontaneous polarization is zero. Moreover, from microscopic view, the antipolar lattice mode is the parameter that is involved to stabilize to antiferroelectric phase such as the free energy curve is a double well with respect to the variation of this parameter. In addition, to rely the calculation of the double well of the free energy as a function of the antipolar mode to the experiment measurement, a double hysteresis loop have been observed (see Figure 2.11).

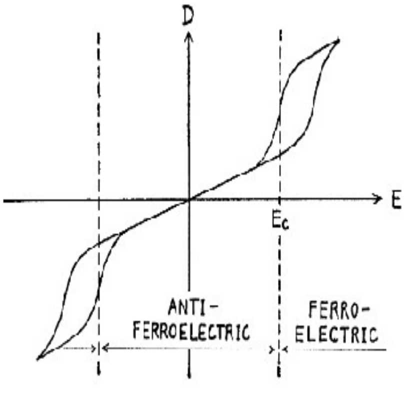

Fig. 2.11: *Tentative explanation of the anomalous hysteresis loops of $PbZr0_3$ at 30 kv/cm. [11]*

For analysis of the shape of this global hysteresis loop, we separated this loop into two hysteresis loop as shown in figure 2.12

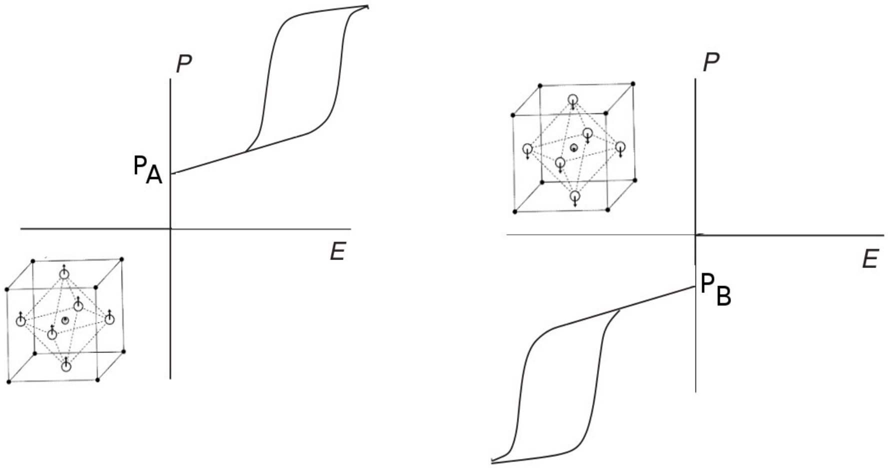

Fig. 2.12: *Illustration of the hysteresis loop for a sublattice.*

from which we can related each one to the measurement of the polarization as a function of an applied electric field to one sublattice that has only one direction of polarization. For the other opposite direction of the polarization, we relate this loop to the second hysteresis loop that involve the negative values of the applied electric field and the polarizations. Hence this typical hysteresis loops may be seen only above an electric field.

2.8 Conclusion

In this chapter, we have reviewed the main crystal properties that are related to the study of WO_3. We have then detailed the Landau theory to explain the process of any structural phase transition from a microscopic viewpoint. Additionally, we have provide a description of the origin of the structural instabilities, which will be used in chapter 4 to investigate the phase diagram of WO_3. In particular, we have analyzed the main characteristics of the antiferroelectric properties, which will be helpful to define any antiferroelectric matarial as WO_3.

Chapter 3

First-principles background

3.1 Introduction

The aim of this chapter is to provide a detailed formalism of the Density Functional Theory (DFT). We report the general equations and approximations, which are the basic tools to investigate the ground-state properties of different class of materials. We introcude then the DFT with some details related to the pratical numerical implementions as they are used in the calculations of the essential properties of WO_3.

3.2 The electronic problem

To study and analyze the structure of matter, we need to solve the electronic Schrodinger equation [64]:

$$\hat{h}_e \Phi(\mathbf{R},\mathbf{r}) = \epsilon(\mathbf{R}) \Phi(\mathbf{R},\mathbf{r}) \tag{3.2.1}$$

for a system of N interacting electrons in the external Coulomb field coming from atomic nuclei. $\Phi(\mathbf{R},\mathbf{r})$ represents the many-electron wave function, and the parameters $\mathbf{R}$ are the nuclei coordinates. The eignenvalues $\epsilon(\mathbf{R})$ depend parametrically on $\mathbf{R}$, and define the energy surfaces. The ground electronic state is the basic feature to study the structural aspects of materials. The electronic Hamiltonian is:

$$\hat{h}_e = -\frac{\hbar}{2m}\sum_{i=1}^{N}\nabla_i^2 - e^2\sum_{I=1}^{P}\sum_{i=1}^{N}\frac{Z_I}{|\boldsymbol{R_I} - \boldsymbol{r_i}|} + \frac{e^2}{2}\sum_{i=1}^{N}\sum_{j\neq 1}^{N}\frac{1}{|\boldsymbol{R_i} - \boldsymbol{r_j}|} \tag{3.2.2}$$

where the first term is the kinectic energy, the second is the electron-nuclear interaction, and the third is the electronic repulsion. The electrons are represented by a wave function .

However, the presence of an electron in a region of space influences the behavior of the other electrons in other regions, so that they cannot be considered as individual entities. Therefore, the wave function of many-electron system cannot be simply written as the product of the wave function of individual electron. On the other hand, the fact that the wave function cannot be factorized involves that the exact solution of Schrodinger's equation needs solving an equation in 3N degrees of freedom. In fact, the exact solution is known only in the case of the homogeneous electron gas, for atoms with a small number of electron, and for a few small molecules. Therefore, the only way forward is devising approximations to solve this problem. Thus, the knowledge of the electronic structure of the system gives access to all the physical properties.

3.3 Quantum many-body theory: chemical approach

In 1928, Hartree proposed the first approach to the many-electron problem. His basic assumption is that the many-electron wave function can be written as a simple product of one-electron orbitals but this is not enough for general electronic systems. He proposed that the electrostatic field felt by an electron in an atom was due to the central potential of nucleus together with the field created by other electrons. this approach was called self-consistent field (HSCF). In the same year, Slater recognizes that the HSCF can be written as equations from a variational principle by postulating a total wave function as the product form

$$\Phi(\mathbf{r}) = \Pi_{i=1}^{N}\varphi_i(\boldsymbol{r_i}) \tag{3.3.1}$$

The application of the variational principle leads to a calculation of the total energy for an ansatz wave function of the form Eq.(2.3), by perform variations with respect to the one-electron orbitals Φ_i. The Hamiltonian of general many-electron system is written as:

$$\hat{H}(\mathbf{R},\mathbf{r}) = \sum_{i=1}^{N} \hat{h}_1(i) + \sum_{i=1}^{N} \sum_{j \neq i}^{N} \hat{v}_2(i,j) \tag{3.3.2}$$

where

$$\hat{h}_1(i) = -\frac{\hbar}{2m} \nabla_{r_i}^2 v_{ext}(\boldsymbol{R}, \boldsymbol{r_i}) \tag{3.3.3}$$

is a one-electron operator that describes the motion of a single electron interacting with all the nuclei in the system, and possibly also other external field, through v_{ext}. The second term takes into account the interaction with the electron and other electron, which represents the Coulomb electron-electron interaction

$$\hat{v}_2(i,j) = \frac{1}{|\boldsymbol{r_i} - \boldsymbol{r_j}|} \tag{3.3.4}$$

Here we have not include spin-orbital coupling. The variational energy is composed of two parts: one arising from the one-electron operator $\hat{h}_1$, and the second one is a two-electron contribution from $\hat{v}_2$. The energy of one-electron is

$$E^{(1)} = \int \Phi(\boldsymbol{r}^*) (\sum_{i=1}^{N} \hat{h}_1(i)) \Phi(\boldsymbol{r}) d\boldsymbol{r}, \tag{3.3.5}$$

If we replace the product wave function (2.6) into (2.7) and after simplification we get :

$$E^{(1)} = \sum_{i=1}^{N} \int \varphi(\boldsymbol{r_i}^*) (\sum_{i=1}^{N} \hat{h}_1(i)) \varphi(\boldsymbol{r_i}) d\boldsymbol{r_i} = \sum_{i=1}^{N} E_{ii}, \tag{3.3.6}$$

we assume that the one-electon orbitals are normalized to one. The two-electron terms contribution to the energy is:

$$E^{(2)} = \int \Phi(\boldsymbol{r}^*) \sum_{i=1}^{N} \sum_{j \neq i}^{N} \hat{v}_2(i,j) \Phi(\boldsymbol{r}) d\boldsymbol{r}, \tag{3.3.7}$$

This expression can be re-written in terms of the partial densities ρ_i(i)=$|\Phi_i(\boldsymbol{r_i})|^2$ of the individual electron:

$$E^{(2)} = \frac{1}{2}\sum_{i=1}^{N}\sum_{j\neq i}^{N}\int\int\frac{\rho_i(i)\rho_j(j)}{|\boldsymbol{r_i}-\boldsymbol{r_j}|}d\boldsymbol{r_i}d\boldsymbol{r_j}E^{(2)} = \frac{1}{2}\sum_{i=1}^{N}\sum_{j\neq i}^{N}\boldsymbol{J}_{i,j}, \tag{3.3.8}$$

where the factor 1/2 discounts for the double counting of J$_{i,j}$ and $J_{j,i}$. Therefore, the total energy of an electronic system within the HSCF approximation is:

$$E_{HSCF} = \sum_{i=1}^{N}E_{ii} + \frac{1}{2}\sum_{i=1}^{N}\sum_{j\neq i}^{N}\boldsymbol{J}_{i,j} \tag{3.3.9}$$

The one-electron orbitals $\Phi^*(\boldsymbol{r_i})$ are taken as independent from $\Phi^*(\boldsymbol{r_i})$. The real and the imaginary parts of orbitals are consider as independent. Moreover, we have to impose appropriate normalization constrains. The variational equation reads:

$$\delta E_{HSCF} - \sum_{i=1}^{N}\varepsilon_i\int|\Phi_i(\boldsymbol{r_i})|d\boldsymbol{r_i} - 1 = 0, \tag{3.3.10}$$

where ε_i are Lagrange multipliers. The corresponding Lagrange equations lead to a set of one-particle Schrodinger equations in an effective, state-dependent potential that takes into account the interaction with the electrostatic field of the other electrons, as

$$(-\frac{\hbar}{2m}\nabla^2 v_{eff}^{(i)}(\boldsymbol{R},\boldsymbol{r}))\Phi_i(\boldsymbol{r}) = \varepsilon_i\Phi_i(\boldsymbol{r}) \tag{3.3.11}$$

with

$$v_{eff}^{(i)}(\boldsymbol{R},\boldsymbol{r}) = v_{ext}(\boldsymbol{R},\boldsymbol{r}) + \int\frac{\sum_{j\neq i}^{N}|\Phi_i(\boldsymbol{r}')|^2}{|\boldsymbol{r}-\boldsymbol{r}'|}d\boldsymbol{r}' \tag{3.3.12}$$

The second term in (2.14) is the classical electrostatic potential felt by particle i, which is due to the charge distribution of all the other electrons. The charge density does not include the charge of the particle i, thus the Hartree approximation is, correctly, self-interaction free. The HSCF approximation leads to write the energy with the correct expression in terms of the eigenvalues:

$$E_{HSCF} = \sum_{i=1}^{N} \varepsilon_i - \frac{1}{2}\sum_{i=1}^{N}\sum_{j\neq i}^{N} J_{ij}. \tag{3.3.13}$$

We can solve the set of N coupled partial differential equations (3.3.11) by minimizing the energy with respect to a set of variational parameters in a trial wave function or, alternatively, by re-calculating the effective potential (3.3.12) using the solution of (3.3.11), and solving the Schrodinger equation again. We have to repeat this procedure until input and ouput wave function are the same, it is said that self-consistency has been achieved.

3.4 The Hartree-Fock approximation

In this case the electrons are treated as distinguishable particles, they have indistinguishable spin-1/2, i.e. fermions, and Pauli's principle states that two fermions cannot occupy the same quantum state because the many-fermion wave function has to be antisymmetric upon particle exchange. Therefore, if two electron are exchanged, the wave function must change sign.

The Pauli's principle is done by proposing an antisymmetrized many-electron wave function in the form of Slater determinant.

3.5 Modern density functional theory

The hopes that the energy of the system can be written exclusively in terms of the electronic density was the big challenge during the past twenty years. In 1964, Hohenberg and Kohn developed the DFT theory that is divided into two parts.

3.5.1 The Hohenberg-Kohn theorem

Theorem 1: The external potential is univocally determined by the electronic density, besides a trivial additive constant.

Proof: In the beginning, we suppose that the external potential is not univocally determined by the density. Therefore, we have to find two potentials v and v' such that their ground state density ρ is the same. We suppose that Φ and $E_0 = \langle\Phi|\hat{H}|\Phi\rangle$ are the ground state wave function and the ground state energy of the Hamiltonian $\hat{H}=\hat{T}+\hat{V}_{ext}+\hat{U}_{ee}$ also $\Phi^{'}$ and $E_0^{'} = \langle\Phi|\hat{H}|\Phi\rangle$ are the ground state wave function and the ground state energy of the Hamiltonian $\hat{H}^{'}=\hat{T}+\hat{V}_{ext}^{'}+\hat{U}_{ee}$. According to Rayleigh-Ritz's variational principle we have:

$$E_0 < \langle\Phi^{'}|\hat{H}|\Phi^{'}\rangle = \langle\Phi^{'}|\hat{H}^{'}|\Phi^{'}\rangle + \langle\Phi^{'}|\hat{H}-\hat{H}^{'}|\Phi^{'}\rangle = E_0^{'} + \int \rho(\boldsymbol{r})[v_{ext}(\boldsymbol{r} - v_{ext}(\boldsymbol{r})]d\boldsymbol{r}, \quad (3.5.1)$$

In this case we have used the fact that different Hamiltonian necessarily correspond to different ground state. On the other hand, we can also exchange the roles of Φ and $\Phi^{'}$ ($\hat{H}$ and $\hat{H}^{'}$), so we obtain:

$$E_0^{'} < \langle\Phi|\hat{H}^{'}|\Phi\rangle = \langle\Phi|\hat{H}|\Phi\rangle + < \Phi|\hat{H}^{'} - \hat{H}|\Phi\rangle = E_0 - \int \rho(\boldsymbol{r})[v_{ext}(\boldsymbol{r}) - v_{ext}(\boldsymbol{r})]d\boldsymbol{r}, \quad (3.5.2)$$

Now, if we add these two inequalities, it gives that $E_0+E_0^{'} < E_0+E_0^{'}$, which is absurd. Therefore, the two different external potentials cannot correspond to the same electronic density for the ground state, unless they differ by a trivial additive constant.

Corollary: Since $\rho(\boldsymbol{r})$ univocally determines v_{ext}, it also determines the ground state wave function Φ, which should be obtained by solving the full many-body Schrodinger equation.

Theorem 2: Let $\tilde{\rho}$ be a non-negative density normalized to N. We define the variational energy E_v, which is a functional of the density because of the previous theorem, in the following way:

$$E_v[\tilde{\rho}] = F_v[\tilde{\rho}] + \int \tilde{\rho}(\boldsymbol{r})v_{ext}(\boldsymbol{r})d\boldsymbol{r}, \quad (3.5.3)$$

with

$$F_v[\tilde{\rho}] = \langle\Phi[\tilde{\rho}]|\hat{T} + \hat{U}_{ee}|[\tilde{\rho}]\rangle. \quad (3.5.4)$$

Here $\Phi[\tilde{\rho}]$ is the ground state of a potential which has $\tilde{\rho}$ as its ground state density, so that $E_O = E_v[\rho]$ verifies

$$E_O < E_v[\rho] \quad (3.5.5)$$

for any system $\tilde{\rho} \neq \rho$, and thus is the ground state energy.

Proof: We have

$$\langle\Phi[\tilde{\rho}]|\hat{H}|[\tilde{\rho}]\rangle = F_v[\tilde{\rho}] + \int \tilde{\rho}(\boldsymbol{r})v_{ext}(\boldsymbol{r})d\boldsymbol{r} = E_v[\tilde{\rho}] \geq E_v[\rho] = E_O = \langle\Phi[\rho]|\hat{H}|\Phi[\rho]\rangle \quad (3.5.6)$$

The inequality follows from Rayleigh-Ritz's variational principle for the wave function, but applied to electronic density. Thus, the variatinal principle states that

$$\delta E_v[\rho] - \mu(\int \rho(\boldsymbol{r})d\rho(\boldsymbol{r}) - N) = 0 \quad (3.5.7)$$

which leads to a generalization of the Thomas-Fermi equation:

$$\mu = \frac{\delta E_v[\rho]}{\delta\rho} = v_{ext} + \frac{\delta F_v[\rho]}{\delta\rho} \quad (3.5.8)$$

If F$[\rho]$ is known, the solution of the full many-body Schrodinger equation will be known. In addition, F$[\rho]$ is a universal functional, which depends only on the electronic density and does not depend explicitly on the external potential. The Hohenberg-Kohn formulation of the F$[\rho]$ is :

$$F_v[\rho] = \langle\Phi[\rho]|\hat{T} + \hat{U}_{ee}|\Phi[\rho]\rangle \quad (3.5.9)$$

where $\Phi[\rho]$ is the ground state many-body wave function. Therefore, these two theorems form the mathematical basis of density functional theory (DFT).

3.5.2 Constrained search formulation

Within the Hohenberg-Kohn theorem, the electronic density determines the external potential. However, the electronic density has to correspond to a ground state antisymmetric wave function, otherwise the density ρ is not true. In 1982, Lavy reformulated DFT theory in such way that the antisymmetric origin of the density is realized. The universal functional F$[\rho]$ given by the expression (3.24) thus redefined by Levy to be :

$$F[\rho] = min_{\Phi\rightarrow\rho}\left\{\langle\Phi|\hat{T} + \hat{U}_{ee}|\Phi\rangle\right\}, \quad (3.5.10)$$

where ρ is any non-negative density such that

$$\int \rho(\boldsymbol{r})d\rho(\boldsymbol{r}) = Nand \int |\nabla^{1/2}\rho(\boldsymbol{r})|^2 d\boldsymbol{r} < \infty, \tag{3.5.11}$$

Therefore, this additional constaint lets the density arises from an antisymmetric wave function.

3.5.3 Ground state in DFT

The knowledge of the universal functional F$[\rho]$ allows us to determine the electronic ground state density and the exact energy. This defines the main features of the DFT theory as a ground state theory. However, the difficulty of solving the full many-body Schrodinger equation is still a practical problem more than a conceptual one. In 1965, Kohn and Sham devised a practical scheme for determining the ground state, where we will discuss in the next subsection.

3.5.4 The Kohn-Sham Equations

The electron-electron interaction is the term that introduces many-body effect. We can expressed the electron-electron interaction in terms of the two-body density matrix $\rho_2(\boldsymbol{r}-\boldsymbol{r}^{'})$ in the following form:

$$U_{ee} = \langle\Phi|\hat{U}_{ee}|\Phi\rangle = \frac{1}{2}\sum_{i=1}^{N}\sum_{j\neq i}^{N}\langle\Phi|\frac{1}{|r_i - r_j|}|\Phi\rangle = \int\int \frac{\rho_2(\boldsymbol{r},\boldsymbol{r}^{'})}{|\boldsymbol{r}-\boldsymbol{r}^{'}|}d\boldsymbol{r}d\boldsymbol{r}^{'} \tag{3.5.12}$$

$$\rho_2(\boldsymbol{r},\boldsymbol{r}^{'}) = \frac{1}{2}\rho_1(\boldsymbol{r},\boldsymbol{r})\rho_1(\boldsymbol{r}^{'},\boldsymbol{r}^{'})g(\boldsymbol{r},\boldsymbol{r}^{'}), \tag{3.5.13}$$

where $\rho_1(\boldsymbol{r},\boldsymbol{r}\ )$ is the one-body density matrix such that its diagonal elements are $\rho(\boldsymbol{r}) = \rho_1(\boldsymbol{r},\boldsymbol{r})$ represent the electronic density and $g(\boldsymbol{r},\boldsymbol{r}^{'})$ defines the two-body direct correlation function that is different from one only when $\boldsymbol{r}$ is sufficiently close to $\boldsymbol{r}^{'}$. We can separate the energetic contributions to the electron-electron interaction into two terms. The first term ignores correlation altogether, as the case $\rho(\boldsymbol{r})$ =1 everywhere. The second term contains both local (on-site) and non-local contributions. The expression for U$_{ee}$ is then re-written as

$$U_{ee} = \frac{1}{2}\int\int \frac{\rho(\boldsymbol{r})\rho(\boldsymbol{r}')}{|r-r'|} d\boldsymbol{r}d\boldsymbol{r}' + \frac{1}{2}\int\int \frac{\rho(\boldsymbol{r})\rho(\boldsymbol{r}')}{|r-r'|}[g(\boldsymbol{r},\boldsymbol{r}') - 1]d\boldsymbol{r}d\boldsymbol{r}' \qquad (3.5.14)$$

The first therm is the classical electrostatic interaction energy correspond to charge distribution $\rho(\boldsymbol{r})$ that is called the Hartree term. The second term represents both the exchange and correlation effects. When the system is uncorrelated, the second term in (2.29) is neglected. In this case the two-body interaction assumes the classical electrostatic from a continous distribution of charge $\rho(\boldsymbol{r})$.

Now, we introduce the exchange interaction that takes into account Pauli's exclusion principle. In fact, this principle forbids the presence of electron with the same spin in the same position. Therefore, the exchange-only part of the pair correlation function verifies

$$g_{X_{r\to r'}}(\boldsymbol{r},\boldsymbol{r}') \to 1/2. \qquad (3.5.15)$$

If we neglected the correlation, the electron-electron interaction corresponds then to the many-body wave function given by a Slater determinant, which ensures that the Pauli's principle is verified. This case correspond to Hartree-Fock theory, in which the electron-electron interaction is written as:

$$U_{ee}^{HF} = \frac{1}{2}\int\int \frac{\rho^{HF}(\boldsymbol{r})\rho^{HF}(\boldsymbol{r}')}{|r-r'|} d\boldsymbol{r}d\boldsymbol{r}' + \frac{1}{2}\int\int \frac{\rho^{HF}(\boldsymbol{r})\rho^{HF}(\boldsymbol{r}')}{|r-r'|}[g_X(\boldsymbol{r},\boldsymbol{r}') - \boldsymbol{1}]d\boldsymbol{r}d\boldsymbol{r}' \qquad (3.5.16)$$

The exact expression for the exchange depletion, or the exhange hole, is (Parr and Yang. 1989):

$$g_X(\boldsymbol{r},\boldsymbol{r}') = 1 - \frac{\sum_\sigma |\rho^{HF}(\boldsymbol{r}-\boldsymbol{r}')|^2}{\rho^{HF}(\boldsymbol{r})\rho^{HF}(\boldsymbol{r}')} \qquad (3.5.17)$$

where the sum is over the two spin projections. The density and the density matrix in (3.23) are determined from the ground state Slater determinant. The correlation hole is calculated as g$_C(\boldsymbol{r},\boldsymbol{r}')$ =g$(\boldsymbol{r},\boldsymbol{r}')$-g$_X(\boldsymbol{r},\boldsymbol{r}')$, that is the remaining part of the correlation function once exchange has been taken into account. This part of the pair correlation function represents a major problem in many-body theory. For the homogeneous electron gas, the exact solution is known numerically (Ceperley and Alder, 1980), However, for the inhomogeneous electron gas, the problem to find the solution is still present. On the other hand, there are many approximations related to the inhomogeneous electron gas, that including slowly varying densities through its spatial gradient, and also expression fort the exchange-correlation energy that takes into account very weak, non-local interactions such as Van der Waals interaction (Zaremba and Kohn, 1976).

Finally, the energy of a many-body electron system can be written as:

$$E = T + V_{ext} + \frac{1}{2}\int \frac{\rho(\boldsymbol{r})\rho(\boldsymbol{r}^{'})}{|r-r^{'}|} d\boldsymbol{r}d\boldsymbol{r}^{'} + E_{XC} \tag{3.5.18}$$

where E_{XC} is defined as the exchange and correlation energy.

$$E_{XC} = \frac{1}{2}\int \frac{\rho(\boldsymbol{r})\rho(\boldsymbol{r}^{'})}{|r-r^{'}|}[g(\boldsymbol{r},\boldsymbol{r}^{'}) - 1])d\boldsymbol{r}d\boldsymbol{r}^{'} \tag{3.5.19}$$

The Hartree and the exchange (Hartree-Fock) terms can be calculated exactly. However, the correlation term is the biggest difficulty. For that, over the last decades, a significant research improvement was produced to find a reasonable good approximations for a large class of systems of interest.

For the kinectic energy T= $\langle\Phi|\hat{T}|\Phi\rangle$ is also an other problem, because its explicit expression in terms of electronic density is not known. In 1965, Kohn and Sham suggested a more general approach. In fact, a system of non-interacting electrons is exactly described by an antisymmetric wave function of the Slater determinant type that is made of one-electron orbitals. Therefore, for a such wave function the kinectic energy can be easily obtained in terms of the one-electron orbitals. Therefore, the ground state density matrix $\rho_1(\boldsymbol{r},\boldsymbol{r}^{'})$ is given by

$$\rho_1(\boldsymbol{r},\boldsymbol{r}^{'}) = \sum_{10}^{\infty} f_i \Phi_i(\boldsymbol{r})\Phi_i^*(\boldsymbol{r}^{'}), \tag{3.5.20}$$

where $\Phi_i(\boldsymbol{r})$ are the one-electron orbitals and f$_i$ are the occupation numbers corresponding to these orbitals. Then, related to Eq(3.35), the exact expression for the kinectic energy of the non-interacting electrons is

$$T = -\frac{\hbar^2}{2m}\sum_{1}^{\infty} f_i\langle\Phi_i|\nabla^2|\Phi_i\rangle. \tag{3.5.21}$$

The idea of Kohn and Sham was to find a system of non-interacting electrons that produces the same electronic density as the interaction system. As a result of this action, the kinectic energy of the interacting system can be calculated exactly via (3.36) However, this energy is not the exact kinectic energy the interacting system due to the fact that the true many-body wave function is not a Slater determinant. Because of this there a correlation contribution to the kinectic energy, which must be included in the correlation energy term.

We assume that a system of non-interacting electrons whose ground state density coincides with that of the interacting system, does exist. We call this system, the non-interacting reference system of density $\rho(\boldsymbol{r})$, and the Hamiltonian associated is

$$\hat{H}_R = \sum_{i=1}^{N}[-\frac{\hbar^2}{2m}\nabla_i^2 + v_R(\boldsymbol{r_i})], \tag{3.5.22}$$

with N the number of electron and v_R is a reference potential that the ground state of $\hat{H}_R$ equals $\rho(\boldsymbol{r})$. Then, in this case, Hohenberg-Kohn's theorem ensures that the ground state energy equals the energy of the interacting system.

This Hamiltonian of non-interacting system has no electron-electron interaction. Then this eigen states can be expressed in the form of Slater determinant

$$\Phi(\boldsymbol{r}) = \frac{1}{\sqrt{N_s!}}[\Phi_1(\boldsymbol{r_1})\Phi_2(\boldsymbol{r_2})...\Phi_{N_s}(\boldsymbol{r_{N_s}})], \tag{3.5.23}$$

where we have chosen the closed shell situation in which the occupation number are 2 < N$_s$ and 0 for i > N$_s$, with N$_s$ is the number of doubly occupation orbitals. Therefore, withi this hypothesis, the density can be rewritten as:

$$\rho(\boldsymbol{r}) = 2\sum_{i=1}^{N_s}|\Phi(\boldsymbol{r})|^2, \tag{3.5.24}$$

while the kinectic term is

$$T_R[\rho] = -\frac{\hbar^2}{2m}\sum_{1}^{N_s} f_i < \Phi_i|\nabla^2|\Phi_i > . \tag{3.5.25}$$

where $\Phi(\boldsymbol{r})$ are the N$_s$ lowest-energy eigenfunctions of the one-electron Hamiltonian

$$\hat{H}_{KS} = -\frac{\hbar^2}{2m}\nabla_i^2 + v_R(\boldsymbol{r_i}), \tag{3.5.26}$$

which are attained by solving the one-electron Schrodinger equation

$$\hat{H}_{KS}\Phi_i(\boldsymbol{r}) = \epsilon_i\Phi_i(\boldsymbol{r}). \tag{3.5.27}$$

Therefore, if we consider the new form T$_R[\rho]$, the universal density functional can be rewritten as

$$F[\rho] = T_R[\rho] + \frac{1}{2}\int\int \frac{\rho(\boldsymbol{r})\rho(\boldsymbol{r}')}{|r-r'|} g(\boldsymbol{r},\boldsymbol{r}')d\boldsymbol{r}d\boldsymbol{r}' + \tilde{E}_{XC}, \tag{3.5.28}$$

where the exchange correlation energy $\tilde{E}_{XC}$ is different from the E_{XC} given by (3.31) that takes into account the kinetic correlation ignored in T$_R[\rho]$. Accordingly, the total Kohn-Sham energy functional E$_{KS}[\rho]$

$$E_{KS}[\rho] = T_R[\rho] + \int \rho(\boldsymbol{r})v_{ext}(\boldsymbol{r}) \tag{3.5.29}$$

By this manner the energy functional is expressed in terms of the N$_s$ orbitals that minimize the non-interacting elecronic kinectic energy under the fixed density constraint.

3.5.5 Extension to spin-polarized system

In this part, we consider the electronic density as composed by two independent spin densities, $\rho = \rho\uparrow + \rho\downarrow$. Each one of these densities is built, with the Kohn-Sham spin orbitals, which fulfill the self-consistent Kohn-Sham equations

$$-\frac{\hbar^2}{2m} + v_{R,s}\Phi_i(\boldsymbol{r}) = \epsilon_{i,s}\Phi_{i,s}(\boldsymbol{r}) \tag{3.5.30}$$

where the subindex s indicates the spin component (↑ or ↓). The same for the reference potentials $v_{R,s}$ that are achieved as an extension of the Eqs. (3.41) and (3.42) to the spin-dependence case

$$v_{R,s} = v_{ext}(\boldsymbol{r}) + \int \frac{\rho(\boldsymbol{r'})}{|r-r'|} d\boldsymbol{r'} + \mu_{XC,s}[\rho\uparrow, \rho\downarrow](\boldsymbol{r}), \tag{3.5.31}$$

with

$$\mu_{XC,s}[\rho\uparrow, \rho\downarrow](\boldsymbol{r}) = \frac{\tilde{E}_{XC,s}}{\delta\rho(\boldsymbol{r})}. \tag{3.5.32}$$

At once, the exchange-correlation energy and the potential depend on the spin-density, that are built via the Kohn-Sham spin orbitals, as

$$\rho(\boldsymbol{r}) = \sum_{i=}^{N_s} |\Phi_i(\boldsymbol{r})|^2, \tag{3.5.33}$$

where N_s is the number of occupied spin orbitals with the spin projection s. The exchange-correlation functionals are given in terms of the total electronic density ρ and the spin-polarization (magnetization) density ζ, which are defined as

$$\rho(\boldsymbol{r}) = \rho_\uparrow(\boldsymbol{r}) + \rho_\downarrow(\boldsymbol{r}) \tag{3.5.34}$$

and

$$\zeta(\boldsymbol{r}) = \rho_\uparrow(\boldsymbol{r}) - \rho_\downarrow(\boldsymbol{r}) \tag{3.5.35}$$

In the expression (3.49) and (3.50), the density affect two different numbers of electrons $N_\uparrow$ and $N_\downarrow$, such that the sum $N= N_\uparrow+N_\downarrow$ is the total number of electrons in the system. Therefore, if we take into count the spin-polarization, we will be in the approach of spin density functional theory (SDFT), otherwise if $\rho_\uparrow = \rho_\downarrow$ we will go back to DFT theory with double occupancy of single-particle orbitals. In the SDFT the total energy is written as

$$E_{KS}[\rho\uparrow, \rho\downarrow] = T_R[\rho\uparrow, \rho\downarrow] + \int \rho(\boldsymbol{r}) v_{ext}(\boldsymbol{r}) d\boldsymbol{r} + \frac{1}{2} \int\int \frac{\rho(\boldsymbol{r'})}{|r-r'|} d\boldsymbol{r'} \tag{3.5.36}$$

with

$$T_R[\rho\uparrow,\rho\downarrow] = -\frac{\hbar^2}{2m}\sum_{s=1}^{2}\sum_{i=1}^{N_s}\langle\Phi_{i,s}|\nabla^2|\Phi_{i,s}\rangle. \tag{3.5.37}$$

The solution of the Kohn-Sham equations must be obtained by an iterative procedure. Therefore, the total energy will be written as follows:

$$\begin{aligned} E_{KS}[\rho\uparrow,\rho\downarrow] &= \sum_{s=1}^{2}\sum_{i=1}^{N_s}\epsilon_{i,s} - \frac{1}{2}\int\int\frac{\rho(\boldsymbol{r})\rho(\boldsymbol{r}')}{|r-r'|}d\boldsymbol{r}d\boldsymbol{r}' \\ &+\tilde{E}_{XC}[\rho\uparrow,\rho\downarrow] - \int\rho(\boldsymbol{r})\mu_{XC}[\rho\uparrow,\rho\downarrow](\boldsymbol{r})d(\boldsymbol{r}), \end{aligned} \tag{3.5.38}$$

which is the same expression for the unpolarized case, with the sum over spin components is replaced by a factor of 2, and the spin-polarized expression for the exchange-correlation potential are replaced by the unpolarized ones.

3.6 Exchange and correlation in DFT: approximations and their performance

From the previous section, we have divided the total energy of an electronic system into a number of different contribution, E[ρ]= T$_R$+V$_{ext}$+E$_H$+E$_X$+$\tilde{E}_C$ which each term can be handled separately. T$_R$ is the non-interacting kinectic energy, E$_H$ is the classical electron-electron interaction of Hartree term, V$_{ext}$ is the interaction of the electrons with external fields, in particular that of the atomic nuclei, E$_X$ is the exchange energy and $\tilde{E}_C$ is the coupling constant averaged correlation term. The second and the third terms are known to be explicit functionals of the electronic density. The first and the fourth terms are known as functionals of the non-interacting orbitals, which are in turn (unknown) functionals of the density. The correlation energy is an unknown functional of the density . Wigner was the first who handled this subject in the circumstance of the homogeneous electrons gas, by proposing a correlation energy per unit volume given by Expression (2.29).

3.6.1 The local density approximation

For a long time, the local density approximation (LDA) is the most used approximation to the exchange-correlation energy. In 1965, Kohn and Sham proposed the LDA approach in which the main idea was to consider a general inhomogeneous electronic system as locally homogeneous and then to use the exchange-correlation hole corresponding to the homogeneous electron gas. The expression for the (non-local) exchange-correlation hole ρ is defined in the following way:

$$\tilde{\rho}^{LDA}(\boldsymbol{r},\boldsymbol{r}') = \rho(\boldsymbol{r})\left\{\tilde{g}^{h}[|\boldsymbol{r}-\boldsymbol{r'}|,\rho(\boldsymbol{r})]-1\right\} \tag{3.6.1}$$

with $\tilde{g}^{h}[|\boldsymbol{r}-\boldsymbol{r'}|,\rho(\boldsymbol{r})]$ the pair correlation function of the homogeneous gas which depends only on the distance between $\boldsymbol{r}$ and $\boldsymbol{r'}$ and must be evaluated for the density ρ that locally assumes the value $\rho(\boldsymbol{r})$. Therefore the exchange-correlation energy can be written as:

$$\tilde{E}_{XC}^{LDA}[\rho] = \int \rho(\boldsymbol{r})\tilde{\epsilon}_{XC}[\boldsymbol{r}]d\boldsymbol{r}, \tag{3.6.2}$$

where the expression for the exchange-correlation energy density $\tilde{\epsilon}_{XC}$ is written in terms of the exhange-correlation hole as :

$$\tilde{\epsilon}_{XC}^{LDA}[\rho] = \frac{1}{2}\int \frac{\tilde{\rho}^{LDA}(\boldsymbol{r},\boldsymbol{r}')}{|\boldsymbol{r}-\boldsymbol{r}'|}d\boldsymbol{r}'. \tag{3.6.3}$$

In practice, the exchange-correlation energy density $\tilde{\epsilon}_{XC}^{LDA}[\rho]$ is can be written as $\tilde{\epsilon}_{XC}^{LDA}[\rho]=$ $\epsilon_{X}^{LDA}[\rho]+\tilde{\epsilon}_{C}^{LDA}[\rho]$, where ϵ_{X}^{LDA} is the exchange energy density given by Dirac's expression :

$$\tilde{\epsilon}_{C}^{D}[\rho] = -\frac{3}{4}(\frac{3}{\pi})^{1/3}\rho^{1/3} = -\frac{0.458}{r_s}a.u., \tag{3.6.4}$$

where $r_s=(3/4\pi\rho)^{1/3}$ is the mean interelectronic distance expressed in atomic units and $\tilde{\epsilon}_{C}^{LDA}[\rho]$ the correlation energy density given by Perdew and Zungen in 1981 by the following expression:

$$\epsilon_{C}^{PZ}[\rho] = \{Aln(r_s)+B+Cr_s ln(rs)+Dr_s\} \tag{3.6.5}$$

Despite the wide use of the LDA approximation to the exchange-correlation energy. This approach has some limitations as the self-interaction present in the Hartree term of the energy is not completely canceled by the LDA exchange-correlation term. Also, the inhomogeneities are not taken into account in the density. To improve the reliability of the consistent approximations to the exchange-correlation energy over the LDA approach, an other exploited approach was developed is called the generalized gradient approximation (GGA). In this approach,we introduce the semi-local inhomogeneities of the density, by expanding the E_{XC} as a series in terms of the density and its gradient.

3.6.2 The generalized gradient approximation (GGA)

The exchange-correlation energy is written as a second order gradient expansion :

$$E_{XC}[\rho] = \int A_{XC}[\rho]\rho(\boldsymbol{r})^{4/3} + C_{XC}[\rho]|\nabla\rho(\boldsymbol{r})|^2/\rho(\boldsymbol{r})^{4/3}d\boldsymbol{r} \tag{3.6.6}$$

which is asymptotically valid for the densities that vary slowly in the space. The GGA approach conserves the correct features of the LDA and combines them with the inhomogeneity features that are assumed to be energetically the most important ones.

Examples of GGA approaches as : the Langreth-Mehl functional, the BLYP functional and the PBE functional.

3.6.3 Hybrid HF-KS approaches

The Hartree-Fock approach was to develop a new approximation which combines the LDA and GGA approaches. These combination of DFT and Hartree-Fock exchange is expressed as follows:

$$E_{XC}^{hyb} = \alpha E_X^{HF} + (1-\alpha)E_X^{DFT} + E_C^{DFT} \tag{3.6.7}$$

where the coefficient α is either chosen to assume a specific value such as $1/2$, or fit to some properties of a molecular database. In this case, the generalized Kohn-Sham equations can be written in the form of the usual KS equations (4.34), but with corrective terms:

$$\left\{\hat{H}_{KS}[\rho] + \Delta\hat{\mu}_X[\{\phi_i\}] + \Delta\hat{\mu}_C\right\}\phi(\boldsymbol{r}) = \epsilon_i\phi_i(\boldsymbol{r}) \tag{3.6.8}$$

which are small, but not important. The generalized Kohn-Sham schemes modifies the functional becoming:

$$F^{\alpha}_{HF-KS} = \langle\Phi|\hat{T} + \alpha\hat{V}_{ee}|\Phi\rangle = F_{KS} + \alpha E_H[\Phi] + \alpha E_X[\Phi] \tag{3.6.9}$$

which is minimized with respect to a wave function Φ of the determinant form, and the rest of the energy is treated within the usual approximation to the Kohn-Sham problem, typically GGA. This scheme contains an unknown, formally exact correlation term that is absent in standard HF. This approach is known as the Hartree-Kohn-Sham scheme (HF-KS). An example of the hybrid approximation, is the B3LYB approach made by Becke in 1993. (The exact exchange-correlation energy is not known explicitly and is consider as the main limitation of the DFT theory)

3.7 Solving the electronic problem in practice

The main mathematical problem in electronic structure theory, at the single particle approximation level, is to self-consistently solve the N coupled, three-dimensional, partial differential equations. In reality, the Hartee-Fock and Kohn-Sham methodologies had simplified the 3N-dimensional many-body problem. In this section, we will analyze the electron-nuclear interaction and the mathematical representation of the single-particle orbitals.

3.7.1 Kohn-Sham and Hartree-Fock equations

The density functional theory was formulated within the Kohn-Sham equation:

$$\{-\frac{\hbar^2}{2m}\nabla^2 + V_{ext}(\boldsymbol{r}) + \int \frac{\rho(\boldsymbol{r}')}{|\boldsymbol{r}-\boldsymbol{r}'|}d\boldsymbol{r}' + \mu_{XC}[\rho]\}\phi_i(\boldsymbol{r}) = \varepsilon_i\phi_i(\boldsymbol{r}) \tag{3.7.1}$$

where the electronic density ρ is given by

$$\rho(\boldsymbol{r}) = \sum_{i=1}^{N} f_i|\phi_i(\boldsymbol{r})|^2, \tag{3.7.2}$$

where N is the number of electrons, and f$_i$ are the occupation numbers corresponding to the one-electron eigenstates. In the case spin-unpolarized insulators or closed shell molecules, f$_i$=2 for the N/2 lowest eigenstates and f$_i$=0 otherwise. For the spin-polarized systems or open-shell molecules the exchange-correlation potential, and the external potential when there are external magnetic field, depends on the spin projection. The external potential v$_{ext}(\boldsymbol{r})$ represents the interaction between the electrons and the nuclei, this expression is as following :

$$v_{ext}(\boldsymbol{r}) = -e^2 \sum_{P} \frac{Z_I}{|\boldsymbol{r} - \boldsymbol{R}_I|}; \tag{3.7.3}$$

For the exchange-correlation potential ν_{XC} is given by the expression(3.65) The solution of the Kohn-Sham equation involves to know how to treat the electron-nuclear interaction first and to find mathematical way to represent the single-particle orbitals.

3.7.2 The electron-nuclear interaction

The equation (3.65), give the expression of the electron-nuclear interaction. Nevertheless, there is a distinction made between two classes of electrons, one for those that can participate in the formation of a chemical bond, named the valence electron, and one other for those that are tightly bound to the nuclei, called the core electron, which do not participate in bonding and can be considered as frozen orbitals. The core electron are not completely insensitive to the molecular or crystal field. In addition, there is a third class of electrons, called semi-core electrons, which are treated similarly to valence electrons, but do not participate actively in chemical bonding.

3.7.3 Pseudopotential methods

Because the different characteristics of the two classes of the electrons, they are handled in a different way. In fact, the core electrons do not participate actively in the chemical bonding then it is possible to eliminate the corresponding degrees of freedom by replacing the atomic nuclei with an effective nucleus that represents the nucleus and its core electrons together. Therefore, the number of the electron treated explicitly is much smaller. Furthermore, the interaction between the valence electron and the ionic core is not the Coulomb interaction because it includes that part of election-electron interaction related to the screening of the nuclear charge by the core electron. As a consequence, the Coulomb interaction must be replaced by a pseudo-potential or effective core potential. In the periodic crystal, the wave functions for free electrons can be expanded in plane waves (PWs).

3.7.4 Classes of basis sets

In order to represent the Kohn-Sham orbitals, two main group of basis set had been developed. (i) Extended basis sets: The basis functions are delocalized, either floating (independent of the nuclear position) or centered at the nuclear positions, it cover all space. This basis are useful for condensed phases such as solids or liquids. (ii) localized basis sets: The basis set are localized,

3.7.5 Atomic pseudopotentials

In the periodic crystal, the wave functions for free electrons can be expanded as plane waves (PWs). The most common pseudopotential approach consists of not allowing the relaxation of core states according to its environment. In 1959, Philips and Kleinman constructed a smooth valence wave function $\tilde{\phi}_v$ that is not orthogonalized to the core states ϕ_c, by combining the core and the true valence wave functions ϕ_v in the following way:

$$|\tilde{\phi}_v\rangle = |\phi_v\rangle + \sum_c \alpha_{cv}|\phi_c\rangle \tag{3.7.4}$$

where $\alpha_{cv} = \langle\phi_c|\tilde{\phi}_v\rangle \neq 0$. This wave function is called pseudo-wave function that satisfies the modified Schrodinger equation:

$$\Big[\tilde{H} + \sum_c (\epsilon_v - \epsilon_c)|\phi_v\rangle\langle\phi_c|\Big]|\tilde{\phi}_v\rangle = \epsilon_v|\tilde{\phi}_v\rangle, \tag{3.7.5}$$

where $\hat{H} = \hat{T} + \hat{V}$, $\hat{V} = (Z_c/r)\tilde{I}$ is the bare nuclear potential, and $\tilde{I}$ is the identity operator. In this way, it's possible to construct a pseudo-Hamiltonian

$$\hat{H}_{PS} = \hat{H} + \sum_c (\epsilon_v - \epsilon_c)|\phi_v\rangle\langle\phi_c| \tag{3.7.6}$$

with the same eigenvalues of original Hamiltonian but a smoother wave function. The potential associated to the pseudo-Hamiltonian is expressed in the following way:

$$\hat{V}_{PS} = \frac{Z_C}{r}\tilde{I} + \sum_c (\epsilon_v - \epsilon_c)|\phi_v\rangle\langle\phi_c| \tag{3.7.7}$$

that is called a pseudopotential.

This pseudopotential behaves differently on wave functions of different angular momentum. The most general form of a pseudopotential is written as:

$$\hat{V}_{PS}(\boldsymbol{r}) = \sum_{l=0}^{\infty} \sum_{m=-l}^{l} v_{PS}^{l}(r)|lm\rangle\langle lm| = \sum_{l=0}^{\infty} v_{PS}^{l}(r)\hat{P}_l \tag{3.7.8}$$

where $\langle\, r|lm\rangle = Y_{lm}(\theta,\phi)$ are spherical harmonics, v_{PS}^{l}(r) is the pseudopotential corresponding to the angular component l, and the operator

$$\hat{P}_l = \sum_{m=-l}^{l} |lm\rangle\langle lm| \tag{3.7.9}$$

is a projection operator onto the lth angular momentum subspace. The expression (2.71) means that when $\hat{V}_{PS}$ acts on the electronic wave function, the projection operators $\hat{P}_l$ select the different angular momentum components of the wave function, which are then multiplied by the corresponding pseudopotential $v_{PS}^{l}(r)$.

3.7.6 Basis sets

In order, to resolve the electronic structure problem within DFT theory, it requires one to choose a mathematical representation for the one-electron orbitals. Therefore, different type of basis sets have been proposed and adapted for electronic structure calculation. In fact, the one-electron wave functions can be expanded on a generic basis set described by the orbitals $|\phi_\alpha\rangle$. The representation of this orbitals in the a real-space is $\langle\, r|lm\rangle$. The Kohn-Sham orbitals are then written as a linear combination of these basis orbitals:

$$\varphi_j(\boldsymbol{r}) = \sum_{\alpha=1}^{M} c_{j\alpha}\phi_\alpha(\boldsymbol{r}), \tag{3.7.10}$$

where j labels the wave function, the sum is over all the basis functions up to the dimension of the basis set M, and $c_{j\alpha}$ are the expansion coefficients of the wave functions j.

In the periodic systems such as solids, the combination of basis orbitals that represents a solution of Schrodinger equation contains the translational periodicity of the supercell. Therefore, the previous expression has to be modified in the following way:

$$\varphi_j^{\boldsymbol{k}}(\boldsymbol{r}) = e^{i\boldsymbol{kr}} \sum_{\alpha=1}^{M} c_{j\alpha}^{\boldsymbol{r}}\phi_\alpha(\boldsymbol{r}) = \sum_{\alpha=1}^{M} c_{j\alpha}^{\boldsymbol{r}}\phi_\alpha^{\boldsymbol{k}}(\boldsymbol{r}), \tag{3.7.11}$$

where $\boldsymbol{k}$ indicates the wave vector in the Brillouin zone, and the modified basis functions are:

$$\varphi_j(\boldsymbol{r}) = e^{i\boldsymbol{kr}}\phi_\alpha(\boldsymbol{r}). \tag{3.7.12}$$

This representation is good enough for basis functions that already respect the periodic boundary conditions, such as plane waves.

An other type of basis set is the Gaussian-type orbitals (GTO). In this case, the GTO have been used to replace the exponentials. Furthermore, the exponents of the Gaussian functions are variationally optimized to be consistent with the corresponding atomic wave functions.

3.8 Conclusion

In this Chapter, we have proposed an overview of the DFT theory and different approximations, which are proposed to give a good description of the main features of any material. We have then paid a particular attention to the development of the approximation formulations that are behind the success of many first-principles investigations of the materials.

Chapter 4

First-principles re-investigation of bulk WO_3

4.1 Introduction

In this chapter, we use first-principles density functional calculations within hybrid-functional method to analyze the structural properties of tungsten trioxide WO_3. Our calculations rely on density functional theory and the use of the B1-WC hybrid approach, which provides very good agreement with experimental data. We show that the hypothetical high-symmetry cubic reference structure combines several ferroelectric and antiferrodistortive (antipolar cation motions, rotations and tilts of oxygen octahedra) structural instabilities. We then condense various possible combinations of these unstable modes, which allow us to reproduce all experimentally observed structures. We also reveal the structural properties of the ground state of WO_3 and role of a calculated polar phase, that has an energy close to that of the ground state, to make WO_3 a potential antiferroelectric material.

4.2 Computational details

Our first-principles calculations have been performed in the context of density functional theory, using the B1-WC hybrid functional [65] as implemented in the CRYSTAL code. [66] We have used the all-electron double-ζ basis sets for the oxygen atoms and small core Detlev Figgen pseudo-potentials, [67] associated with double-ζ valence basis sets for tungsten. We performed full structural relaxations with a convergence criteria on the root-mean-square of the gradient and displacements smaller than 5×10^{-4} hartree/bohr and 5×10^{-4} bohr respectively. The electronic self-consistent calculations were converged until the difference of the total energy was smaller than 10^{-9} Hartree. The phonon frequencies and Born effective charges were computed using frozen phonon numerical differences [68, 69] and the electric polarization through the Berry phase technique. [70] The integration in the Brillouin zone has been performed with a $8 \times 8 \times 8$ grid of k-points for the cubic unit cell and a $4 \times 4 \times 4$ grid for cells doubled in the three directions with respect to the cubic one.

Our choice of an hybrid functional is in line with the results of Wang *et al.* [71], who have shown that hybrid functionals, and specially HSE06, provide good description of the structural and electronic properties of WO_3. In our study, we selected the B1-WC functional that was specially designed for perovskite oxides [65] and was already successfully applied to a variety of other compounds. [72–75]

4.3 Analysis of the experimental phases

Several DFT studies of WO_3 have been performed previously [76–88] essentially focusing on the main and most common phases and on the electronic structure analysis with and without oxygen vacancies. A detailed analysis of the complex structural phase diagram of WO_3 is thus missing while a microscopic knowledge of the origin of these different phases would be extremely valuable to understand the unique properties of WO_3.

In this section we start by characterizing the different phases of WO_3 observed experimentally to validate our approach and we will discuss the possible origin of the Pc phase. We will also analyze the electronic structure of these phases and we will discuss how the B1-WC compares with the previous studies. Further analysis of these phases and other never observed metastable phases (comparison of relative internal energies, symmetry mode analysis of the distortions, coupling of modes) will be reported in 4.4.2.

4.3.1 Structural and crystallographic analysis

In Table 4.1 we compare our calculated crystallographic data of the $P4/nmm$, $P4/ncc$, $Pbcn$, $P2_1/n$, $P\bar{1}$ and $P2_1/c$ phases against the experimental measurements. Because the $P2_1/c$ phase is not observed experimentally at low temperature, we compare it with the closely related experimental *Pc* phase.

Our calculations of the $P4/nmm$ phase are in very good agreement with the observed cell parameters and the atomic positions. The $P4/nmm$ phase is anti-polar and consists of highly distorted WO_3 octahedra where the W–O bonds dimerize in opposite direction along the [110] perovskite direction. This W–O dimerization forms local dipole-moments that are aligned along the [001] direction and anti-aligned along the [110] direction, so that the total dipole-moment cancels. The crystallographic unit cell is elongated along the [001] direction and compressed along the [100] and [010] directions. This antipolar distortion remains present in all the phase discussed below in this Section.

The $P4/ncc$ phase shows additional octahedra rotations around the z axis ($a^0a^0c^-$ in the Glazer notation [89]), which induces a cell doubling along the [001] direction. The calculated c cell parameter and the z component of the atomic positions are in good agreement with experiments while the in-plane displacements are less well reproduced (Tab. 4.1). The calculated a and b cell parameters are smaller than in experiments by 0.1 Å and the deviation from the tetragonal O_2 position are about two times larger than observed. We clearly overestimate the amplitude of the $a^0a^0c^-$ distortion (rotation angle of 13° instead of 7°; see also Fig. 4.6 further discussed in 4.4.2). Although this could be partly intrinsic to the functional, [90] it is worth noticing that our calculations ignore thermal effects while experiments were performed at high temperatures at which distortions might be reduced. [91] Although such a reduction does not seem to appear for the anti-polar motions in the $P4/nmm$ and $P4/ncc$ phases, it might be more substantial for the rotations and we observe that the computed amplitudes of out-of-phase rotations are in much better agreement with experimental data for the low-temperature phases (see further discussed in 4.4.2).

The orthorhombic *Pbcn* phase can be characterized by an additional in-phase octahedra rotation about the crystallographic y axis, yielding a rotation pattern $a^0b^+c^-$. We find a similar overestimate of the octahedra distortions as for the $P4/ncc$ phase while the calculated cell parameters are underestimated with respect to experiments. We note that the anti-polar distortions along the z axis compares well with experiments for $P4/nmm$, $P4/ncc$ and *Pbcn*.

The $P2_1/n$ structure still contains an additional octahedra rotation around the crystallographic x axis, yielding a rotation pattern $a^-b^+c^-$. The calculated cell volume is slightly too small (+0.7%, −0.7% and −1.9% for a, b and c cell parameters respectively) and the oxygen motions related to the octahedra tilt are overestimated (Table 4.1).

The $P\bar{1}$ phase is similar to the $P2_1/n$ phase if one replaces the in-phase rotation by an out-of-phase rotation, yielding a rotation pattern $a^-b^-c^-$. The distortions are anisotropic in all three directions, which causes the cell to be triclinic with the angles α, β and γ close to 90°. The calculated a, b and c cell parameters deviate from experiments by +0.4%, −1.1% and −0.8% respectively.

The $P2_1/c$ differs from the $P\bar{1}$ by the fact that two out-of-phase rotations have same amplitudes, yielding a rotation pattern $a^-a^-c^-$. This phase was never reported at low temperatures but is closely related to the experimental ε (Pc) phase, which only differs from the $P2_1/c$ phase by an additional polar distortions along the c axis. While relaxing the low temperature Pc phase, we observed that the system always comes back in to the higher $P2_1/c$ symmetry. Wijs *et al* using LDA and GGA exchange-correlation functionals [85] found a similar effect. To further assess the dynamical stability of the $P2_1/c$ phase with respect to a potential Pc ground state, we computed the zone-center phonons and did not observe any unstable mode : the lowest polar mode has a frequency of 158 cm^{-1} and is far from being unstable. We also checked whether a soft polar mode can be induced by increasing the cell volume but did not observe any possibility to generate a polar instability. From our calculations, the ground-state structure of intrinsic WO$_3$ corresponds therefore to a $P2_1/c$ phase. Following the argument by Wijs *et al.* [85], we suggest that the polarity in the experimental ε (Pc) phase may be stabilized by the presence of oxygen vacancies or by another extrinsic parameter.

In Table 4.1 we compare our calculated atomic positions and cell parameters of the $P2_1/c$ phase with the experimentally determined Pc phase. The deviations are surprisingly small for lattice parameters (+0.2%, -0.2% and -0.5% for a, b and c) and even smaller for the atomic positions. Comparing the structural parameters obtained with other hybrid functionals PBE0, B3LYP and HSE06 reported by Wang *et al.* [78], we find close agreement with a typical smaller error margin for B1-WC. B1-WC gives a much better agreement for the $P2_1/c$ phase with experimental data than using the three hybrid functionals tested by Wang *et al.*: HSE06, B3LYP and PBE0 with errors of +0.6%, +1.3% and +0.2% on a, +2.1%, +2.5% and +0.6% on b and +0.1%, +3.0%, +1.7% on the c parameter. We notice, however, that the B1-WC often underestimates cell parameters while the three other hybrid functionals overestimate the cell parameters of WO_3.

4.3.2 Electronic structure

In Table 4.2 we compare the calculated electronic structures for the hypothetical cubic, $P4/nmm$, $P4/ncc$, $Pbcn$, $P2_1/n$, $P\bar{1}$ and $P2_1/c$ phases and compare them with the experiments and previous DFT calculations using PBE0, HSE06 and B3LYP hybrid functionals and GW. For the $P2_1/n$ and $P\bar{1}$ phases, experimental data coincide with the B1-WC band gaps. The B1-WC results are similar to those obtained with the HSE06 functional while the PBE0 gives a slightly smaller gap energy and B3LYP larger values. The B1-WC band gap is closest to the results of GW calculations, an agreement also observed for the $P2_1/c$ phase.

Comparing the trend of band gaps between the different phases, we find that both the appearance of anti-polar motions in the $P4/nmm$ phase and out-of-phase rotations in the $I4/mcm$ significantly open the bandgap with respect to the cubic phase. Only the in-phase rotations in the $P4/mbm$ phase seems to play a more minor role and slighly close the bandgap. The calculated electronic gaps are in reasonable agreement with the experimental values for the three low-temperature structures: Eg = 2.85 eV for the room temperature monoclinic phase $P2_1/n$, Eg = 2.98 eV for the triclinic phase $P\bar{1}$ and Eg = 3.28 eV for the monoclinic phase $P2_1/c$. Figure 4.1 shows the density of states (DOS) of these three phases to demonstrate their similarity.

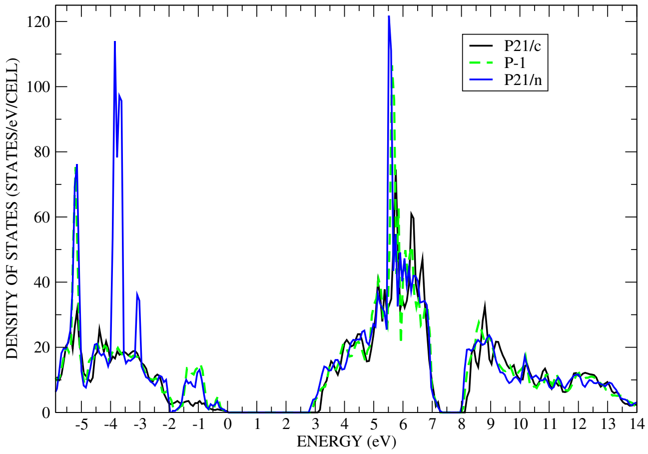

Fig. 4.1: *(Color online) Calculated density of states of the* $P\bar{1}$, $P2_1/n$ *and* $P2_1/c$ *phases with the B1-WC functional.*

Table 4.1: *Calculated lattice parameters in Å and Wyckoff positions of distorted WO_3 phases fully relaxed with the B1-WC functional. For each phase, we specify the space group and the experimental parameters are reported for comparison.*

$P4/nmm$	Present			Exp. [3]		
	a	b	c	a	b	c
	5.299	5.299	3.930	5.297	5.297	3.929
	x	y	z	x	y	z
W_1 (2c)	1/4	1/4	-0.0640	1/4	1/4	-0.0660
O_1 (2c)	1/4	1/4	0.4900	1/4	1/4	0.4900
O_2 (4d)	0	0	0	0	0	0
$P4/ncc$	Present			Exp. [3]		
	a	b	c	a	b	c
	5.168	5.168	7.870	5.278	5.278	7.849
	x	y	z	x	y	z
W_1 (4c)	1/4	1/4	0.2849	1/4	1/4	0.2832
O_1 (4c)	1/4	1/4	0.0057	1/4	1/4	0.0030
O_2 (8f)	0.0570	-0.0570	1/4	0.0250	-0.0250	1/4
$Pbcn$	Present			Exp. [1]		
	a	b	c	a	b	c
	7.284	7.528	7.684	7.333	7.573	7.740
	x	y	z	x	y	z
W_1 (3d)	0.2510	0.0260	0.2800	0.2520	0.0290	0.2830
O_1 (3d)	-0.0010	0.0430	0.2150	-0.0020	0.0320	0.2210
O_2 (3d)	0.2930	0.2590	0.2590	0.2830	0.2690	0.2590
O_3 (3d)	0.2870	0.0100	0.0060	0.2800	0.0130	0.0020
$P\bar{1}$	Present			Exp. [34]		
	a	b	c	a	b	c
	7.334	7.446	7.612	7.309	7.522	7.678
	α	β	γ	α	β	γ
	88.652°	91.022°	91.012°	88.810°	90.920°	90.930°
	x	y	z	x	y	z
W_1 (2i)	0.2603	0.0172	0.2826	0.2566	0.0259	0.2850
W_2 (2i)	0.2540	0.5210	0.2183	0.2502	0.5280	0.2158
W_3 (2i)	0.2397	0.0228	0.7793	0.2438	0.0313	0.7817
W_4 (2i)	0.2456	0.5268	0.7216	0.2499	0.5338	0.7190
O_1 (2i)	0.0015	0.0395	0.2074	0.0007	0.0386	0.2100
O_2 (2i)	0.5022	0.5406	0.2115	0.5038	0.5361	0.2181
O_3 (2i)	0.0026	0.4582	0.2897	0.0076	0.4660	0.2884
O_4 (2i)	0.5012	-0.0398	0.2906	0.4972	-0.0362	0.2878
O_5 (2i)	0.2892	0.2571	0.2836	0.2851	0.2574	0.2870
O_6 (2i)	0.2081	0.7575	0.2174	0.2204	0.7630	0.22232
O_7 (2i)	0.2098	0.2569	0.7232	0.2186	0.2627	0.7258
O_8 (2i)	0.2927	0.7575	0.7772	0.2840	0.7583	0.7679
O_9 (2i)	0.2911	0.0383	0.0060	0.2943	0.0422	-0.0002
O_10 (2i)	0.2889	0.5389	0.4941	0.2971	0.5446	0.4982
O_11 (2i)	0.2108	0.4767	-0.0061	0.2096	0.4820	-0.0072
O_12 (2i)	0.2090	-0.0242	0.5063	0.2088	0.9830	0.5051
$P2_1/n$	Present			Exp. [3]		
	a	b	c	a	b	c
	7.359	7.486	7.544	7.303	7.538	7.692
	α	β	γ	α	β	γ
	90°	91.311°	90°	90°	90.855°	90°
	x	y	z	x	y	z
W_1 (4e)	0.2720	0.0074	0.2790	0.2528	0.0260	0.2855

Table 4.2: *Electronic band gap (in eV) of different phases of* WO_3 *as calculated in the present work with the B1-WC hybrid functional. We compare our results with previous hybrid functional calculations (PBE0, HSE06 and B3LYP), GW calculations and experimental measurements.*

	B1-WC	GW	PBE0	HSE06	B3LYB	Exp1	Exp2	Exp3
Ref.		[92]	[78]	[78]	[78]	[93]	[94]	[79]
cubic	1.50		2.25	1.67	1.89			
$P4/mbm$	1.27							
$I4/mcm$	1.48							
$P4/nmm$	2.12		2.28	1.71	1.85			1.75
$P4/ncc$	2.15							
Pcnb	2.65		3.35	2.57	2.89		3.21	2.35
$P2_1/n$	2.85	2.90	3.67	2.80	3.13	2.75	3.25	2.60
$P\bar{1}$	2.98	3.00	3.67	2.94	3.17			
$P2_1/c$	3.28	3.30						

4.4 Origin of the WO_3 phases

The results presented so far give us confidence that the B1-WC functional reproduces well the experimental measurements so that we can now focus on the structural instabilities of the hypothetical $Pm\bar{3}m$ cubic parent phase and explain how their condensation give rise to the various known phases of WO_3. This also allows us to identify novel ferroelectric metastable phases. In each case, we analyze the crystallographic structure through a decomposition of the distortions with respect to the cubic parent phase in terms of symmetry-adapted modes.

4.4.1 Unstable modes of the cubic reference

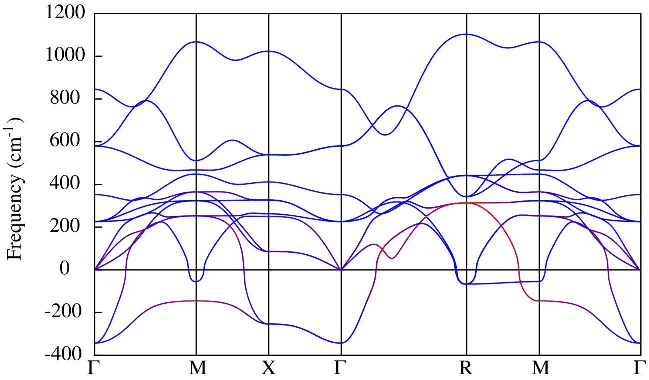

Fig. 4.2: *(Color online) Phonon dispersion curves of cubic* WO_3 *(negative frequencies refer to imaginary frequencies, i.e. to unstable modes). The coordinates of the high symmetry points are as follows:* Γ *(0,0,0), X* $(\frac{1}{2},0,0)$*, M* $(\frac{1}{2},\frac{1}{2},0)$ *and R* $(\frac{1}{2},\frac{1}{2},\frac{1}{2})$*. Thanks to the band2eps postprocessing script of ABINIT, [12] the color of the bands is assigned to each point through the contribution of each atom type to the corresponding eigenvector: red for the tungsten atom and blue for the oxygens.*

Fig. 4.2 shows the calculated phonon dispersion curves of hypothetical cubic WO_3. Two branches of instabilities (imaginary frequencies plotted as negative numbers in Fig. 4.2) coexist in the Brillouin zone.

The first unstable branch has its largest imaginary value at Γ. The Γ unstable mode has the irreducible representation (irrep) Γ_4^- and corresponds to a polar mode. It suggests that the cubic phase of WO_3 is mostly unstable via this polar instability and might be ferroelectric, which we will see later is not exactly the case. The polar instability at Γ propagates toward the X and M points with weak dispersion while it strongly disperses towards the R point. Aside from Γ, the modes of this branch are anti-polar. The dispersion of this unstable branch is very similar to the one reported in $BaTiO_3$ and corresponds to a ferroelectric instability requiring a chain-like correlation of displacements in real space. [95]

The second branch of unstable modes appears between M and R points with smaller amplitudes and a nearly absent dispersion between these two points. The label of the M and R point unstable phonon modes are M_3^+ and R_4^+ and they correspond to rotations of the oxygen octahedra. The dispersion of this branch is comparable to what is observed for similar modes in $SrTiO_3$ or $PbTiO_3$ and linked to a planar character of the correlations of the atomic displacements in real space. [95]

Fig. 4.3 represents a schematic view of the eigenvectors related to the main instabilities of cubic WO_3. The polar mode at Γ (Γ_4^-, 373i cm^{-1}) shows motion of W against the O atoms, which is the source of a large electrical polarization. The anti-polar modes at the X (X_5^-, $256i$ cm^{-1}) and M points (M_3^-, $147i$ cm^{-1}) are associated to opposite displacements from unit cell to unit cell along the [100] and [110] directions respectively. [1] The M_3^+ (62i cm^{-1}) and R_4^+ (69i cm^{-1}) unstable modes correspond rotations of the oxygen octahedra about the central W atom with consecutive octahedra along the rotation direction moving respectively in the same or opposite directions. Using the Glazer notation, [89] the M_3^+ mode corresponds to $a^0a^0a^+$ and the R_4^+ mode to $a^0a^0a^-$.

---

[1] In the cubic cell, the [100], [010] and [001] directions are degenerate. The same applies for the [110], [101] and [011] directions.

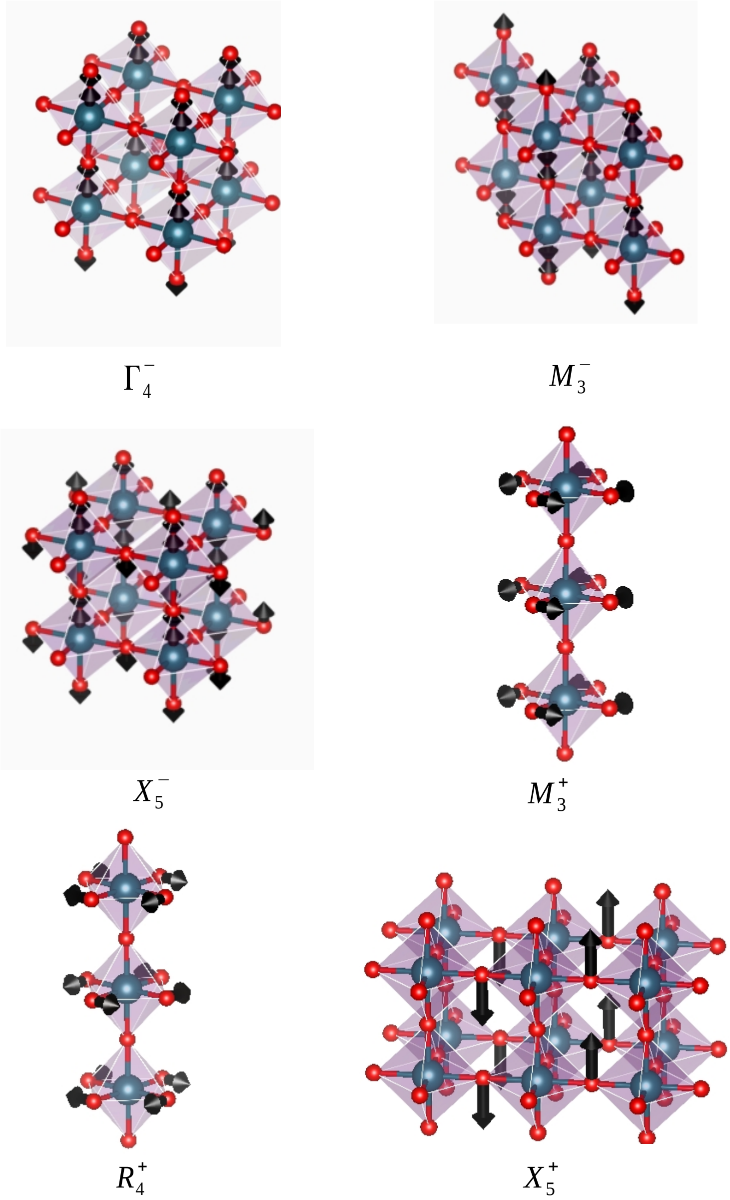

Γ_4^- M_3^-

X_5^- M_3^+

R_4^+ X_5^+

Fig. 4.3: *(Color online) Schematic view of most important modes contributing to the distortions of WO$_3$. Small red spheres represent the oxygens and large blue spheres represent the tungsten atoms. All the modes are unstable but the X_5^+ mode, which is discussed in section 4.4.2.4.*

4.4.2 Condensation and coupling of modes

Starting from the previous unstable modes, we now investigate how their individual and combined condensations in the hypothetical cubic structure give rise to various phases. We then compare their energies and analyze the amplitudes of distortions.

4.4.2.1 Condensation of modes of the unstable polar branch

We first consider the condensation of unstable Γ_4^-, X_5^- and M_3^- modes. Fig. 4.4 shows the energy gain of the corresponding relaxed phase with respect to the cubic phase. We tested several condensation schemes: (i) condensation of the polar Γ_4^-mode along one ($P4mm$), two ($Amm2$) and three ($R3m$) directions ; (ii) condensation of the X_5^- along one ($Pmma$) and two ($P2_1/m$) directions; (iii) condensation of the M_3^- mode along one direction ($P4/nmm$).

We observe that the energy gain of the polar instabilities is large and that the Γ_4^- polar mode drives a larger gain of energy (red columns in Fig. 4.4) than the anti-polar X_5^- and M_3^- modes (green columns in Fig. 4.4). The space group related to the condensation of the M_3^- mode corresponds to the high temperature phase observed experimentally ($P4/nmm$).

Condensation of the Γ_4^- mode along two and three directions produce energy gains larger than its condensation in a single direction so that Γ_4^- mode alone will drive the system polar along the [111] direction with an energy difference between the $Amm2$ and $R3m$ phases of 6 meV. We calculated the polarization amplitude in the three $P4mm$, $Amm2$ and $R3m$ phases using the Berry phase technique and obtain 54, 69 and 69 μC.cm^{-2}. These polarization values are comparable to those observed in robust ferroelectrics such as $PbTiO_3$. They can be explained by the opposite motions of W and O atoms, associated with strongly anomalous Born effective charges (11.73 e for W and -8.78/-1.62 e for $O_{\|}/O_{\perp}$ in good agreement with previous calculations in Ref. [96]).

4.4.2.2 Condensation of modes of the oxygen rotation unstable branch

Fig. 4.4 (blue columns) shows the energy gain given by the condensation of the M_3^+ and R_4^+ modes along one direction ($I4/mbm$ and $I4/mcm$), the R_4^+ mode in three directions ($R\bar{3}c$) and the orthorhombic $Pnma$ phase where the R_4^+ mode is condensed in two directions and the M_3^+

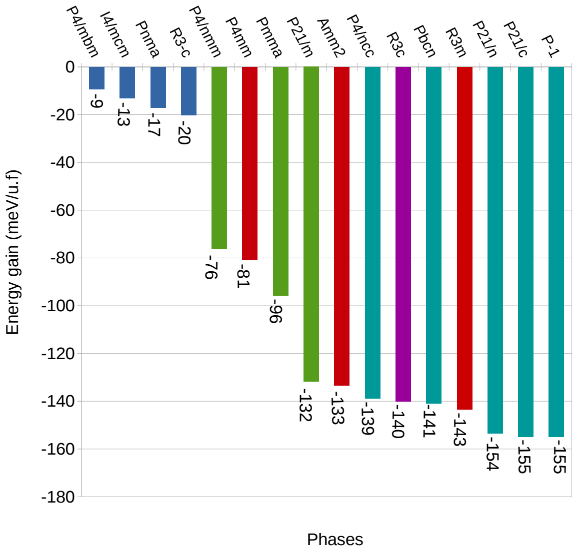

Fig. 4.4: *(Color online) Calculated energy gain (in meV/f.u.) with respect to the cubic phase of different phases of* WO_3*. Red columns are the FE phases arising for the condensation of the polar unstable mode, blue columns are the phases arising from the condensation of the oxygens octahedral rotation unstable modes, green columns are the phases arising from the condensation of anti-polar modes, magenta column represents a phase combining FE and anti-polar modes and cyan columns represent phases combining oxygen octahedral rotations and anti-polar modes. For clarity, the exact value of the energy gain is written in each case.*

mode in one direction ($a^-a^-c^+$). These distortions lower the energy much less than the polar and antipolar motions. This observation is in line with the modest amplitude of the related phonon instabilities : the energy curvatures at the origin are less negative for the octahedral rotations than for the polar motion. Nevertheless the amplitude of octahedral rotations are 10.7 and 11.7 degrees in $I4/mbm$ and $I4/mcm$, respectively. Such large distortions associated to a weak instability highlight relatively small anharmonicities, which might be explained by the absence of A cation with respect to regular ABO_3 perovskites. [97]

4.4.2.3 Combinations of modes

Beside the $P4/nmm$ phase, none of the previous single irrep mode condensations correspond to observed phases. Thus, we now explore the condensation of combined octahedral rotations and polar/anti-polar modes. We depict in Fig. 4.4 the energy gain given by the joint condensation of polar and oxygen rotation modes along three directions ($R3c$, in purple color) and of anti-polar and oxygen rotation modes ($P4/ncc$, $Pbcn$, $P2_1/n$, $P2_1/c$ and $P\bar{1}$, in cyan color).

Combining the polar distortion of the low energy $R3m$ phase with additional oxygen rotation modes does not further reduce the energy. Instead, it yields a $R3c$ phase slightly higher in energy but with a slightly amplified polarization of 71 μC.cm^{-2} and a slightly reduced oxygen rotation (with respect to the $R\bar{3}c$). This emphasizes an unusual competition between these two types of distortions in WO_3 with respect to regular perovskite compounds, where in WO_3 the $R3c$ phase forms a local minimum between the $R\bar{3}c$ and $R3m$ phases.

At the opposite, the mixing of the anti-polar mode M_3^- with oxygen rotation modes can drive larger energy gains so that the ferroelectric $R3m$ phase is not the ground state. This is in agreement with experimental observations where the observed phases at all temperatures contain anti-polar motions. Amongst investigated phases, the $P2_1/c$ phase appears as the most stable but only marginally, as we observe that the $P2_1/n$, $P2_1/c$ and $P\bar{1}$ phases are all extremely close in energy (energy gains of 153, 155 and 155 meV respectively, see Fig. 4.4). Consequently, within the precision of our calculations, we cannot unambiguously assess which one is the ground state. Nevertheless, as discussed in Section 4.3.1 and further exemplified in the next Section, the $P2_1/c$ phase is in excellent agreement with the experimental Pc ground state, except for a tiny polar distortion. Our calculations highlight that, in fact, the $P2_1/n$ and $P\bar{1}$ phases observed at higher temperatures are also extremely close in energy.

We further notice that the ferroelectric $R3m$ phase, although never observed experimentally, is also relatively close in energy to the ground state (about 11 meV/f.u.). Following Rabe, [11] the non-polar (or eventually weakly polar in the experimental Pc phase) ground-state of WO_3 combined with an alternative low-energy ferroelectric phase obtained by polar distortions of the same high-symmetry reference structure makes it a potential antiferroelectric compound. Indeed, applying an electric field, it might be possible to open a typical double hysteresis loop from a field-induced first-order transition from the $P2_1/c$ ground state to the $R3m$ polar phase. Estimating the critical electric field required to stabilize the $R3m$ phase from $\mathcal{E}_c \sim \Delta E/\Omega_0 P_s$, [63] where ΔE is the energy difference between the two phases (11.43 meV/f.u.), P_s the spontaneous polarization of the polar phase (69μC.cm^{-2}) and Ω_0 its unit cell volume (55Å), we get the relatively modest value $\mathcal{E}_c \sim 480$ kV/cm. For the polar phase $R3c$ we need to apply a greater electric field $\mathcal{E}_c \sim 638$ kV/cm to stabilize this phase. This allows us to estimate that the critical field has similar value with respect to other antiferroelectric material, $\mathcal{E}_c \sim 470$kV/cm for ZrO_2 [63] and $\mathcal{E}_c \sim 239$kV/cm for $PbZrO_3$. [2] Although this might not be

---

[2] Value calculated from the energies and polarization reported for the $R3m$ and $Pbam$ phase by S. Amisi in his PhD thesis

easy to check experimentally on real samples that are typically oxygen deficient and highly conductive, the calculations reveal that stoichiometric WO_3 exhibits all the features of an antiferroelectric compound.

4.4.2.4 Symmetry adapted mode analysis of the distorted phases

To quantify the distortions that appear in the various phases we project the structural distortions onto symmetry adapted modes of the cubic phase using AMPLIMODE software. [98] The results in Fig. 4.5 show the amplitudes of the modes in the fully relaxed phases from the calculations but non-observed experimentally. In Fig. 4.6 we show the amplitudes of modes in both the fully relaxed and observed phases, which can be compared.

In the following we discuss the competition/cooperation character of the mode distortions. In perovskite oxides, it is established that the oxygen rotations are in competition with the ferroelectric displacements but less attention has been given to the combinations of other types of mode. Often, this cooperation or competition comes from the biquadratic energy term in the free energy expansion with respect to two order parameters. In WO_3, we observe that the combination between the Γ_4^- mode and the R_4^+ mode along the [111] direction in the $R3c$ phase has the tendency to reduce the amplitude of the oxygen rotations with respect to the $R\bar{3}c$ phase (the R_4^+ mode is 13% smaller in the $R3c$ phase than in the $R\bar{3}c$ phase, see Fig. 4.5) while the polar mode is unaffected. As discussed in the previous section, the combination of the Γ_4^- and R_4^+ modes forms a local minimum ($R3c$ phase) of higher energy than the $R3m$ phase. This means that the polar distortions are in competition with the oxygen rotations as reported for perovskite oxides, with the difference that the polar mode amplitude is unaffected and that the $R3c$ phase is locally stable (the system does not relax into the lowest energy $R3m$ phase). The strain can also play an important role,[3] but when performing the same calculations at fixed cell parameters (fixed to the cubic ones), we find that the $R3c$ phase still forms a local minimum of higher energy than the $R3m$ phase. This unusual energy landscape can come from the marginal gain of energy of the oxygen rotations while large amplitudes of rotation are present.

On the other hand, the association of the oxygen rotations with the antipolar M_3^- mode is cooperative. When we compare the amplitude of the R_4^+ and M_3^- modes of the $P4/nmm$,

---

[3] The volume of the cubic, $R\bar{3}c$, $R3m$ and $R3c$ phases are 54.01Å^3, 50.89Å^3, 55.35Å^3, 52.71Å^3

$I4/mcm$ and $P4/ncc$ (Fig. 4.5 and Fig. 4.6) we find that when both the R_4^+ and M_3^- modes are present together in the $P4/ncc$ phase, their amplitude is slightly higher (4% larger) than when condensed alone ($P4/nmm$ and $I4/mcm$ phases). Their combination, however, drives a sizeable gain of energy: the $P4/ncc$ phase is 63 meV and 126 meV lower in energy than the $P4/nmm$ and the $I4/mcm$ phases, respectively. This means that the combination of the oxygen rotations with the antipolar M_3^- mode is much more cooperative than the combination with the polar mode Γ_4^-.

The $Pbcn$ phase can be understood as a distorted $P4/ncc$ phase with additional M_3^+ oxygen rotations along [010]. The resulting tilt pattern is $a^0b^+c^-$ with a small energy gain of 2 meV with respect to the $P4/ncc$ phase and a reduction of mode amplitudes M_3^-, R_4^+ and M_3^+ (16%, 7% and 22% reduction of the M_3^-, R_4^+ and M_3^+ modes with respect to the phases where they are condensed alone, *i.e.*, $P4/nmm$, $I4/mcm$ and $P4/mbm$, respectively). The M_3^+ mode competes with the R_4^+ and M_3^- modes in the sense their combination reduces their amplitude, but they cooperate to lower the energy of the system.

In the case of the monoclinic $P2_1/n$, $P2_1/c$ and triclinic $P\bar{1}$ phases, the combination of the M_3^- mode with several oxygen rotations ($a^-b^+c^-$ for $P2_1/n$, $a^-a^-c^-$ for $P2_1/c$ and $a^-b^-c^-$ for $P\bar{1}$) lowers the energy of the crystal and with an increase of the mode amplitude with respect to the phases where these modes are condensed independently. For example, the antipolar M_3^- mode has his amplitude increased by 11%, 10% and 19% in the $P2_1/n$, $P2_1/c$ and $P\bar{1}$ phases respectively. This means that the dominant R_4^+ oxygen rotations cooperate with the antipolar M_3^- mode to promote the ground state of WO_3.

We note that in the $P4/nmm$, $P4mm$, $Amm2$, $R3m$, $I4/mcm$, $I4/mbm$, $R\bar{3}c$, $P4/ncc$ and $R3c$ phases the mode decomposition shows only the primary modes we have condensed. This is different with the $Pnma$ phase in which an additional mode X_5^+ appears with a small amplitude in the mode projections while we have condensed only the primary R_4^+ and M_3^+ modes (see Fig. 4.5). This additional mode appears by anharmonic coupling between the R_4^+ and M_3^+ modes such that the symmetry of the $Pnma$ structure allows the X_5^+ mode to develop even though the X_5^+ mode is not unstable by itself. [99] Similarly, we observe the apparition of several additional modes in the $Pbcn$, $P2_1/n$, $P2_1/c$ and $P\bar{1}$ phases, which we discuss in the next section.

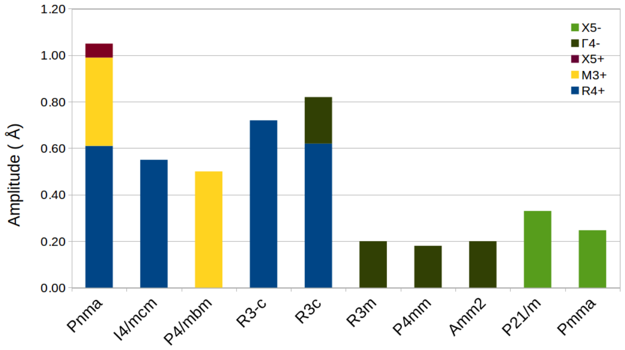

Fig. 4.5: *(Color online) Symmetry adapted mode decomposition of distorted phases of WO$_3$ explored in our study but not observed experimentally.*

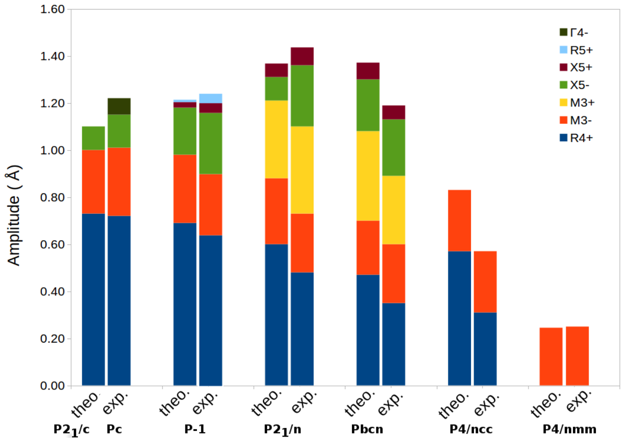

Fig. 4.6: *(Color online) Symmetry adapted mode decomposition of distorted phases WO$_3$; Comparison between experiments and our calculations with the B1-WC functional are shown.*

4.4.2.5 Energy invariants

The different phases arise from the condensation of one or several unstable modes (primary modes) of the cubic parent structure but, in some cases, also include the further condensation of stable modes (secondary modes) with significant amplitudes. Often, the appearance of such secondary modes of large amplitude can be traced back in their linear coupling with the primary modes. [100, 101] This can be rationalized from the existence in the energy expansion of the $Pm\bar{3}m$ phase of invariant terms of the form $\gamma Q_s \prod_{i=1}^{N} Q_p^i$ where Q_s is the amplitude of the secondary mode s and Q_p^i the amplitude of the primary mode i. Depending on the number of primary mode involved, these coupling terms can be bilinear, trilinear, quadrilinear, etc.

To clarify the origin of secondary modes in several low symmetry phases of WO$_3$, we restrict ourself here to the search of such multi-linear invariant terms in the energy expansion around its cubic phase by using the INVARIANTS software. [102] In the last column of Table 4.3 we report these linear invariants up to the fourth order obtained for the $Pnma$, $Pbcn$, $P2_1/n$ and $P2_1/c$ phases. The letters represent the mode amplitudes (Q^i) in the directions specified in the third column where the bold letters refer to the primary modes in the structure (Q^i_p) and the normal letters to secondary modes (Q^i_s).

In the $Pnma$ phase, we find that the X_5^+ mode appears through a trilinear coupling with the oxygen rotation modes R_4^+ and M_3^+ (**ab**c invariant in Table 4.3). This additional X_5^+ mode is also found in $Pnma$ of ABO_3 perovskites [103, 104] where the eigenvector corresponds to anti-polar motions of the A cation. In WO_3 the A-cation is absent and X_5^+ corresponds to similar anti-polar motions but of oxygen instead of the A-site (see Fig. 4.3).

In $Pbcn$ the primary M_3^-mode condenses along z, the R_4^+ mode along z and the M_3^+ mode along y and four additional secondary modes: X_5^- and X_5^+ with a large amplitude and M_5^+ and M_4^+ with a small amplitude as well as an additional component of the M_3^- mode about the x direction. If we restrict ourself to the strongest X_5^- and X_5^+ modes we find that both are coupled with the R_4^+ and M_3^+ modes through a trilinear coupling (**ab**e and **ab**f invariants in Table 4.3) but also through a quadrilinear coupling with the R_4^+ mode and the two components of the M_3^- mode (**ad**ce and **ad**cf invariants in Table 4.3). We can thus explain the appearance of the X_5^+ and X_5^- modes through a trilinear coupling with the oxygen octahedral rotations and the appearance of the second x component of the anti-polar M_3^-mode through a coupling with the secondary X_5^+ and X_5^- modes and the primary R_4^+ mode. The final structure can thus be seen as anti-polar through the M_3^- mode along z with a canting of its direction toward the x axis and through the X_5^- mode along the y direction, the whole distortions being associated with the $a^-b^+c^-$ pattern of oxygen rotation distortions.

The transition from $Pbcn$ to $P2_1/n$ can be seen as being induced by the condensation of the R_4^+ mode along the remaining direction for the oxygen rotation octahedral distortions to $a^-b^+c^-$. This means that we find the same mode coupling as in the $Pbcn$ phase plus some extra ones due to the additional mode condensation. Because we do not induce a new irrep, the couplings are the same (i.e. trilinear and quadrilinear between the primary R_4^+ , M_3^+ and M_3^- modes and the secondary X_5^- and X_5^+ modes) but in different directions from the $Pbcn$ phase: we observe the X_5^- and X_5^+ modes in two directions instead of one. Other modes also appear in the symmetry adapted mode analysis but with smaller amplitudes (M_4^+, M_5^-, M_5^+

and M_2^+), which we do not include in the invariant analysis.

$P\bar{1}$ and $P2_1/c$ are very similar in the sense that for both structures we can envisage the condensation of R_4^+ modes in three directions and the M_3^-mode in one direction. The difference is that in the $P2_1/c$ phase the R_4^+ mode is primary with the same amplitude in two directions and a different amplitude in the third direction ($a^-a^-c^-$where the M_3^-mode is primary in the z direction) while in the $P\bar{1}$ phase the condensation of the R_4^+ mode has different amplitudes in three directions ($a^-b^-c^-$). In $P2_1/c$ the presence of the X_5^- and M_5^- secondary modes can be explained by trilinear coupling with the R_4^+ and M_3^- primary modes (**ac**d+**bc**d and **ab**e invariants in Table 4.3) in a similar way as in the $P2_1/n$ phase.

This analysis shows that the low symmetry phases of WO_3 are complex and involve numerous multilinear couplings of modes if one expands the energy with respect to the cubic phase. We note that, amongst possible couplings, the coupling with the secondary X_5^- mode is most important in all low symmetry phases.

Going further, in order to test whether symmetry arguments can lead to the the polar Pc phase using anharmonic couplings, we have tested if there exists any bi-, tri-, quadri-linear coupling involving a polar mode at the Γ point. We did not find any couplings with the R_4^+ , M_3^+ or M_3^- modes. We thus conclude that it is not possible to generate polarity in WO_3 in the limit to these primary modes, which are the ones appearing in other experimental phases.

4.5 Conclusions

In this study, we have performed a first-principles study of WO_3 using the B1-WC hybrid exchange-correlation functional which appears to yield good overall agreement with experiments regarding electronic and structural properties together.

Starting from the inspection of the phonon dispersion curves of an hypothetical cubic structure taken as reference, we have identified two main branches of instabilities and characterized various phases arising from the condensation of one or more unstable modes. Although the dominant phonon instability is associated to a zone-center polar mode, we found a non-polar $P2_1/c$ ground state arising from the combination of cooperative anti-polar distortions and oxygen octahedra rotations. This phase is very similar to the experimentally reported polar

Pc ground state, except for the absence of a tiny polar distortion. Our calculation does not show however any tendency of the $P2_1/c$ phase to evolve to a Pc phase suggesting that WO_3 is likely not intrinsically ferroelectric. Instead the ferroelectric character might arise from extrinsic defects such as oxygen vacancies. The $P2_1/c$ phase is anti-polar and defects could easily produce a slightly unbalanced anti-dipole structure, yielding a weak net polarization. In this sense, off-stoichiometric WO_3 might be better described as a *ferrielectric* compound. [105] The ground state is determined by two antiparallel movements of W off-centerings which exactly compensate each other in the $P2_1/c$ phase. The displacements are almost identical in the Pc phase, but the two displacements do not fully compensate each other. We suspect that such weak ferrielectricity can be induced by defects such as oxygen vacancies.

At the level of our calculations, the $P2_1/c$ ground-state is almost degenerated in energy with the $P2_1/n$ and $P\bar{1}$ phases observed at higher temperature. Also, we discovered the existence of a never observed and low-energy ferroelectric $R3m$ phase with a large polarization. Although this might not be of direct interest due to the conductive character of usual off-stoichiometric samples, the proximity with the $P2_1/c$ ground-state of this structurally-unrelated $R3m$ polar phase toward which the system could be switch through a first-order transition under moderate electric fields, makes WO_3 a potential antiferroelectric material.

Table 4.3: *Symmetry adapted modes decomposition and linear couplings of modes of the* $Pnma$, $Pbcn$, $P2_1/n$, $P2_1/c$ *and* $P\bar{1}$ *phases. From the left to right columns, we show the mode label (Irrep.) of the symmetry adapted mode, the direction of the mode condensation, the corresponding subgroup, the amplitude of the distortion in the calculated and in the experimental cases (the modes with an amplitude lower than 0.005 Å are not shown) and the linear coupling invariants of the most relevant modes where the letters correspond to the one given in the direction column (we highlight in bold the primary modes).*

Space group	Irrep.	Direction	Subgroup	Amplitudes (Å)		Linear Invariants
				Calc.	Exp.	
$Pnma$	$\mathbf{R}_4^+$	(**a**,**a**,0)	$I4/mma$	0.61	—	**ab**c
	$\mathbf{M}_3^+$	(0,0,**c**)	$P4/mbm$	0.38	—	
	X_5^+	(0,a,0,0,0,0)	Cmcm	0.06	—	
$Pbcn$	$\mathbf{R}_4^+$	(0,0,**a**)	$I4/mcm$	0.47	0.35	**ab**e, **ad**ce **ab**f, **ad**cf
	$\mathbf{M}_3^+$	(0,**b**,0)	$P4/mbm$	0.39	0.30	
	$\mathbf{M}_3^-$	(c,0,**d**)	$Ibam$	0.23	0.25	
	X_5^-	(0,0,e,-e,0,0)	$Pmma$	0.22	0.25	
	X_5^+	(0,0,0,0,f,f)	$Pmma$	0.07	0.06	
$P2_1/n$	$\mathbf{R}_4^+$	(0,**a**,**b**)	$C2/m$	0.60	0.48	**ae**g+**bd**f
	$\mathbf{M}_3^+$	(**c**,0,0)	$P4/mbm$	0.34	0.37	**ac**h+**ac**i-**bc**h+**bc**i
	$\mathbf{M}_3^-$	(0,**d**,**e**)	$Ibam$	0.27	0.25	**acd**g−**bce**f
	X_5^-	(f,-f,0,0,g,g)	$Pmmn$	0.09	0.26	**ade**h+**ade**i+**bde**h−**bde**i
	X_5^+	(0,0,h,i,0,0)	$P2_1/m$	0.06	0.08	
$P2_1/c$	Γ_4^+	(**a**,-**a**,-**b**)	Cm	0	0.067	**ac**d+**bc**d
	$\mathbf{R}_4^+$	(-**b**,**a**,-**a**)	$C2/c$	0.73	0.72	
	$\mathbf{M}_3^-$	(**c**,0,0)	$P4/nmm$	0.27	0.3	
	X_5^-	(0,0,0,-d,0,0)	$Cmcm$	0.10	0.14	

Chapter 5

Density-functional study of the medium polaron formation in WO_3

5.1 Introduction

In this chapter, using DFT hybrid functional calculations, we start by analyzing the medium polaron formation process after the injection of one electron in a supercell of the $P2_1/c$ ground state structure of pure WO_3 [5] and find a self-trapping of this electron on a few d-orbitals of W, which distorts the crystal structure. We then investigate the different possibilities to localized this charge carrier in WO_3 by increasing together the size of the supercell of the $P2_1/c$ ground state structure and α mixing parameter mixing (see chapter3). These allow the development of a medium polaron inside of WO_3 for which we analyze the anisotropic formation process of this polaron in the $P2_1/c$ supercell. We then study and characterize the medium polaron in WO_3. We will show that our simple model calculations can reproduce some of the physical aspects of the medium polaron behavior experimentally observed in WO_3.

5.2 Computational details

The standard DFT theory provides an efficient ab initio method for accurate studies of the ground-state properties of various material. In this work, we focus on the effect of DFT exchange-correlation hybrid functional for describing the electron-electron interaction leading to an accurate description of the polaron in WO_3. The total electron-electron interaction energy is given by [8]

$$E_{ee} = E_H + E_x + E_c, \tag{5.2.1}$$

where E_H is the classical Hartree interaction energy between the electrons in the system. E$_x$ and E$_c$ are the exchange and correlation energy. However, E$_H$ contains the self-interaction of the electrons, which can be eliminate by the exchange energy [106]. Within the LDA and GGA approximations, the self-interaction energy was not completely canceled [107] while the hybrid functional gives a better correction of this unphysical energy by combining the DFT and Hartree-Fock exchange [64] as

$$E_{xc}^{hyb} = \alpha E_x^{HF} + (1-\alpha)E_x^{DFT} + E_c^{DFT}, \tag{5.2.2}$$

where $E_x^{HF(B1)}$ is the exact Hartee-Fock (HF) exchange energy and E$_x$ and E$_c$ are the exchange and correlation energy, respectively, given by the standard DFT theory, and α coefficient is the mixing parameter. In particular, a B1-WC hybrid functional [108] has been built by mixing exact Hartee-Fock with GGA-WC exchange as follows:

$$E_{xc}^{B1WC} = \alpha E_x^{HF} + (1-\alpha)E_x^{GGA-WC} + E_c^{GGA-WC}, \tag{5.2.3}$$

where E$_x^{GGA-WC}$ and E$_c^{GGA-WC}$ are the exchange and correlation energy proposed by Wu and Cohen [109] and the α coefficient is the mixing parameter which is set to 0.16. This functional was specially designed to provide a good description of the structural, electronic, and ferroelectric properties of perovskite oxides [108] compared with experimental data. For our static calculations which neglect zero point motions, to trap one electron in the system, we need to increase the fraction of exact HF exchange which is tuned by the mixing parameter α. Here we will vary this α mixing parameter between 0.16 and 0.25, in keeping with previous results. The default value for the results presented below is α=0.2. We use the CRYSTAL code [66], where the B1-WC hybrid functional is implemented.

Additionally, we have used the all-electron double-ζ basis sets for the oxygen atoms and small core Detlev Figgen pseudo-potentials, [67] associated with double-ζ valence basis sets for tungsten.

We performed structural relaxations by relaxing the atomic positions with a fixed cell volume to the P2$_1$/c grand state phase of pure WO$_3$. The convergence criteria is restrained on the root-mean-square of the gradient and displacements smaller than 5×10^{-4} Hartree/Bohr and 5×10^{-4} Bohr respectively. The electronic self-consistent calculations were converged until the difference of the total energy was smaller than 10^{-9} Hartree. All calculations were performed using spin-polarized.

In order to investigate the effect of an additional dopant charge on the physical behaviors of WO$_3$, we have used four supercells, which two of them; $2 \times 2 \times 1$ (S2) and $2 \times 2 \times 2$ (S3) supercells of the ground state monoclinic P2$_1$/c phase (S1) $(\sqrt{2}, \sqrt{2}, 2)$ [5] that contain 16 and 32 W centers, respectively, and the other two; $4 \times 4 \times 2$ (S4), and $6 \times 6 \times 2$ (S6) supercells of the cubic Pm3m phase (S0) that contain 32 and 72 W centers, respectively. All of these supercells and the unit cell are illustrated in Fig. 5.1.

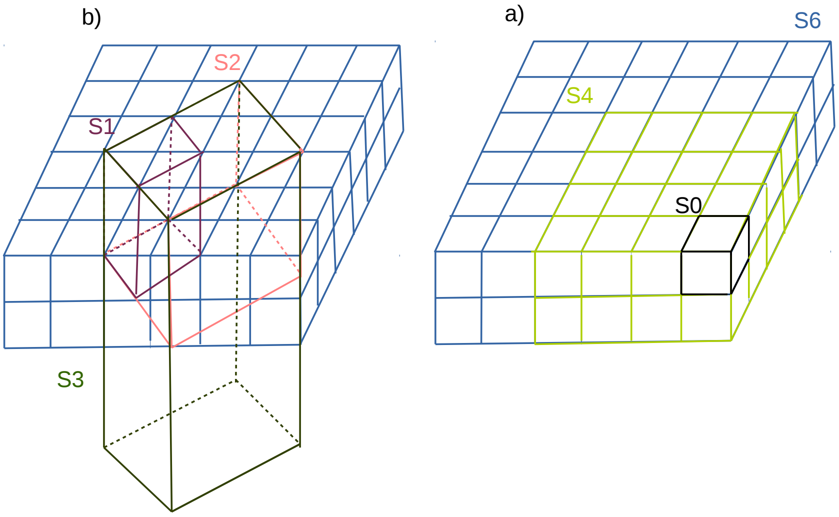

Fig. 5.1: *Illustration of the S2, S3, S4, S6 supercells, which are used of the calculations of the polaron. Each unit cells or supercells are drawn with a particular color.*

The integration in the Brillouin zone has been performed on a $6 \times 6 \times 3$ grid of k-points for the monoclinic P2$_1$/c phase$(\sqrt{2}, \sqrt{2}, 2)$, $4 \times 4 \times 2$ and $4 \times 4 \times 5$ grids for the S2 and S3 supercells, respectively, and a $2 \times 2 \times 5$ grid for the S4 and S6 supercells.

Additional charge was added by the injection of extra electron into the system, with charge neutrality over space being ensured by a corresponding homogeneous positively-charged background.

5.3 Analysis of an anisotropic formation process of medium polaron in WO_3

To analyze the formation process of the medium polaron, we start by relaxing the S3 supercell of the $P2_1/c$ ground state structure of WO_3.

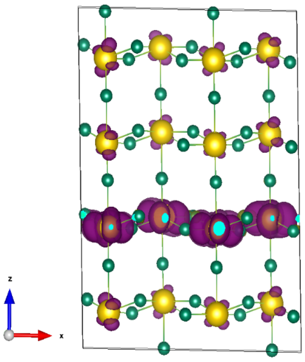

Fig. 5.2: *Spin-density distribution of medium size polaron in the S3 supercell of WO_3, which shows the anisotropic formation of the polaron in WO_3.*

Figure. 5.2 shows that the spin-density distribution of the additional charge for the S3 supercell is localized on only one layer among the four layers. This means that the extension of the polaron is localized on only one (ab) plane, which confirms the anisotropic shape of the polaron in WO_3. Therefore, we perform the calculations of supercells extended along [110] direction of the $P2_1/c$ ground state structure of WO_3.

In order to investigate the effect of the localization of the additional dopant charge in the S6 and S4 supercells of WO_3 on the atomic displacements with respect to the pure $P2_1/c$ ground state structure, we project the structure on the (001) plane. figure. 5.3. In Figure. 5.3, we show the atomic displacements that are intensified on a special zone of the two supercells. The tungsten displacements line up along two lines (the [100] and [010] directions), which cross at the tungsten holding the maximum amount of the doped electron (polaron). This alignment of dipoles that connect the periodic images of the polarons, may generate a net polarization. The oxygen displacements appear to be distorted octahedral rotations, from which we can see that the amplitude of the rotation of the octahedron around the doped electron has

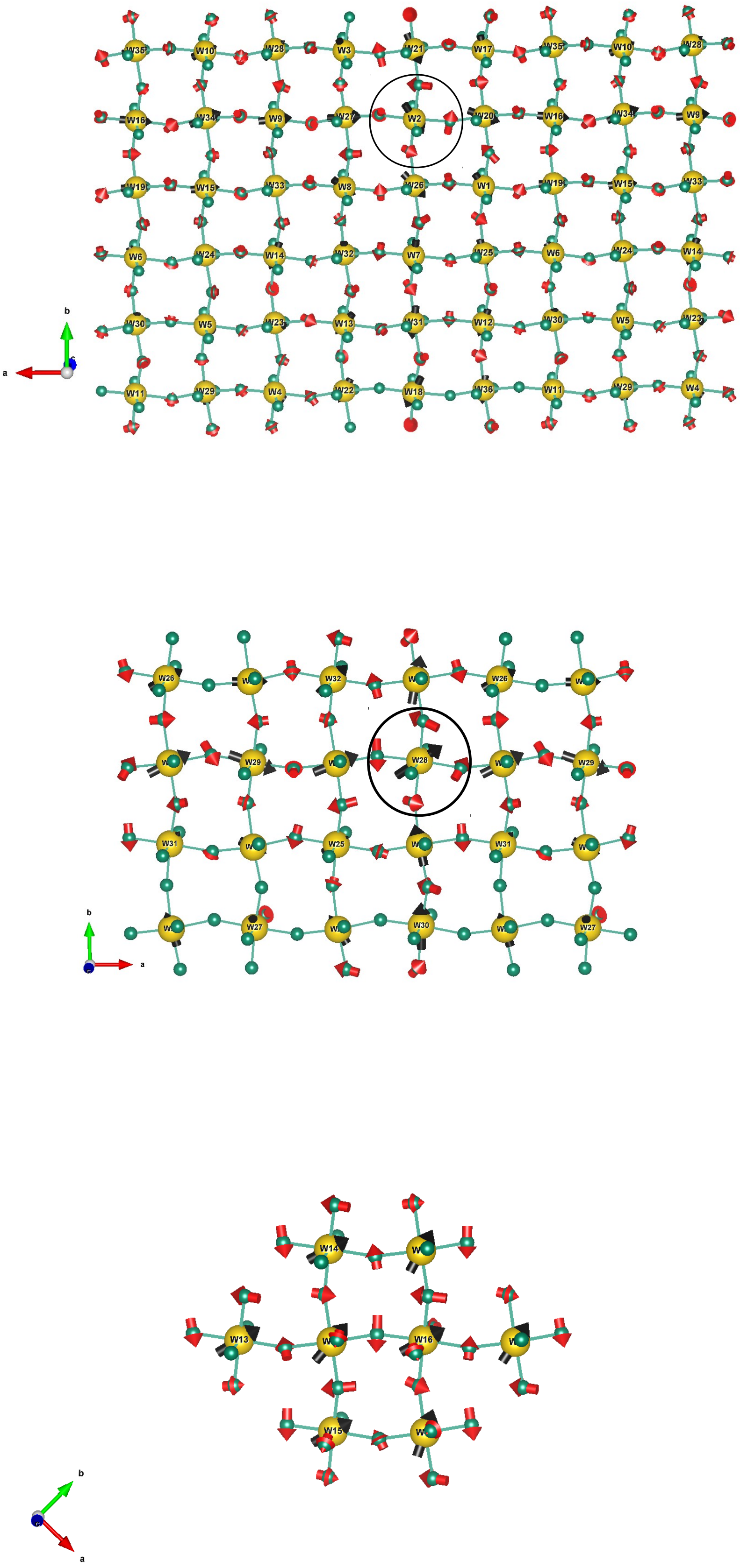

Fig. 5.3: *Polaron formation in the $P2_1/c$ phase using S6, S4 and S2 supercells. We show the displacements of the atoms induced by the presence of an extra electron with respect to the undoped supercell presented previously. The black circles indicate where the polaron is located.*

the largest amplitude compared with other octahedral rotations. This distortion of the octahedron holding the maximum of the doped electron depends on the effect of this charge carrier on the tungsten that keeps a part of this charge with its first nearest neighbor oxygens. One way expect that, due to the Coulomb repulsion between the extra electron partially localized on one particular tungsten and its first neighbors oxygens, we expect that this charge carrier push the oxygens away and thus the local volume of the octahedron increase (CF theory). However, the calculated volume of the octahedron maintaining the extra electron is 19.53Å^3 and for the same one without an extra electron, is 19.74 Å^3. Thus, the volume decreases by 1.1%. This may be due to the strong hybridization between the d orbitals of the tungsten and p orbitals of the oxygens, which decrease the bond length between the tungsten and oxygens.

On the other hand, the octahedron around the doped electron is strongly distorted. Table I, shows the W-O bonds and different O-W-O angles for the octahedron having the extra electron and for the same octahedron but without the extra electron (see Fig. 5.4).

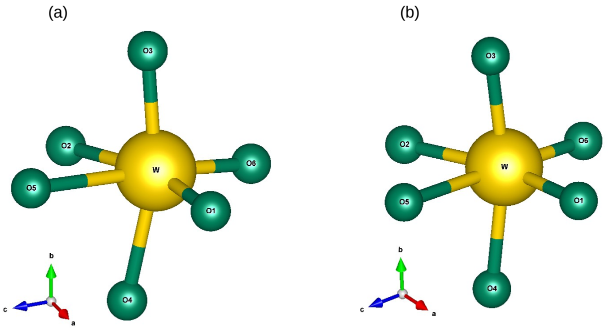

Fig. 5.4: *(a) Coordination of the octahedron holding the maximum of the doped electron compared to the same octahedron without the extra electron (b). The volume of the octahedron (a) decreases compared to (b) due to the localization of the extra electron on the central tungsten position.*

We see that along the [100] direction, the WO bond lengths decreases by around 3%, while along the [010] direction, the bond lengths increase by around 3%, with respect to the $P2_1/c$ phase. Along the [001] direction the WO bond lengths change slightly by around 0.5%. The total distortion is of the Jahn-Teller type. For the O-W-O angles, the oxygens situated on the (ab) plane rotate around the z axis with different angles, which varies between 1 and 2 degrees. Nonetheless, along the [001] direction, the two O5z-W-O5z and O6z-W-O6z angles change only slightly namely by 0.5 degrees. This means that the distortions related to the octahedron having the maximum of the electron are localized in the ab plane, which indicates that the deformation of the polaronic octhaheron is anisotropic.

We conclude that the process of the formation of medium size polaron in WO_3 is an anisotropic process, we can see that the polaron is disc-shaped in the ab plane. We also observe that it localizes on a particular octahedron inside of the W-d_{xy} orbital and finally, it changes the shape of the octahedron only in the ab plane.

Table 5.1: *Bond distances and angles for the octahedron holding the maximum of the doped electron in the S6 supercell. The oxygen position notations are as shown in Fig. 5.4. The subscripts x,y,z are added for convenience to indicate the orientation of the corresponding WO-bond in the crystal.*

Oxygen position	WO-bond (without polaron)(Å)	WO-bond (with polaron)(Å)	difference %	α (deg)
$O1_x$, [100]	1.99168	1.93706	-2.74	2.3655
$O2_x$, [100]	2.002	1.94093	-3.05	1.0707
$O3_y$, [010]	1.81085	1.86789	3.15	1.2334
$O4_y$, [010]	1.82093	1.86841	2.61	2.5623
$O5_z$, [001]	2.13427	2.13085	-0.16	0.5311
$O6_z$, [001]	1.76166	1.75410	-0.43	0.4229

5.4 Electronic properties of the polaron in WO_3

WO_3 is a transition-metal oxide in which the tungsten has a partially filled d sub-shell according to its electronic configuration [Xe] $4f^{14}5d^46s^2$. To form the chemical compound of WO_3 crystal, a sharing of valence electrons between oxygen ([He] $2s^22p^4$) and tungsten has been realized to give rise to the anion O^{2-} and cation W^{6+} which has an empty d sub-shell. The five degenerate d-orbitals ($d_{x^2-y^2}$, d_{z^2}, d_{xy}, d_{xz} and d_{yz}) undergo a splitting. During the process of chemical bonding, each tungsten ion is surrounded by six oxygens giving it octahedral symmetry. The oxygen ions approach the metal ion along the x, y, and z axes. Therefore, the electrons in the d_{z^2} and $d_{x^2-y^2}$ orbitals (which lie along these axes) feel a greater repulsion. As a consequence, having an electron in these orbitals requires more energy than it would to put an electron in one of the other orbitals. This causes a breaking of degeneracy of the d orbitals and, thus, the five d-orbitals split into a lower triplet, t_{2g} (d_{xy}, d_{xz} and d_{yz}) and a doublet, e_g (d_{z^2} and $d_{x^2-y^2}$). This splitting is known as crystal field splitting.

If we add an extra electron in such a degenerate system, it will naturally distort to stabilize one level respect to the other according to the John-Teller theorem. The associated electronic state occupies one of the lowest triplet states, which caused a splitting at the energy levels of the t$_{2g}$ orbitals. The three lower-energy orbitals are collectively referred to the t$_{2g}$ levels, though the trapping of an extra electron on one particular W further splits the t$_{2g}$ orbitals as the extra electron sits on the d$_{xy}$ orbital which further lowers its energy. Fig. 5.5 illustrates the crystal field splitting and splitting related to the localization of the extra electron on cubic WO$_3$.

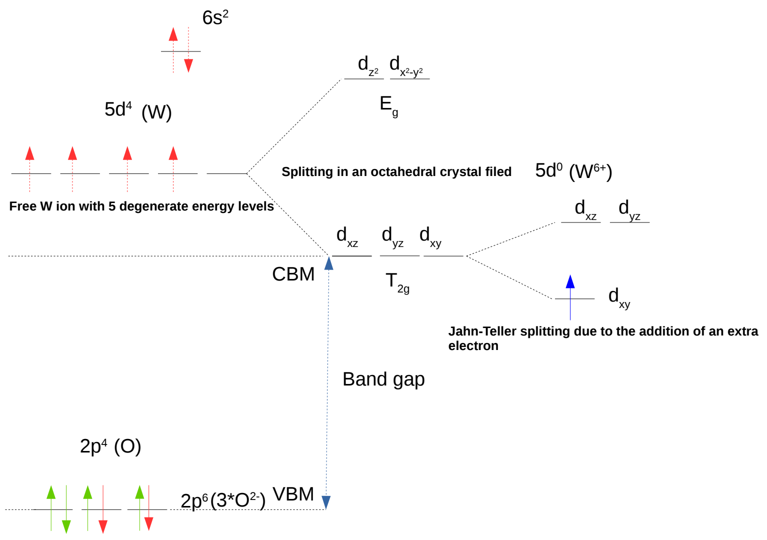

Fig. 5.5: *Illustration of the effect of an octahedral crystal field on the energy levels of a 5d^4 transition metal ion. The degeneracy of the orbitals is further lifted by a Jahn-Teller effect through an elongation of the axial bond.*

In the P2$_1$/c phase, the situation is more complicated as the degeneracy of the t$_{2g}$ states is already broken. Still we observe a strong coupling with the lattice that will be further discussed in the next section. Furthermore, Fig. 5.6 shows the spin-polarization (or magnetization) density of the polaron calculated for the S6 superrcell. The polaron is extended over 9 tungsten sites presented in a disc shaped in the ab plane, which shows the anisotropic distribution of the polaron. In the middle of this disc, one particular tungsten has the largest spin-polarization density. This indicates that the polaron is identified by a dominant spin-polarization density at this specific tungsten site but it still has a large probability density away from the center of the disc.

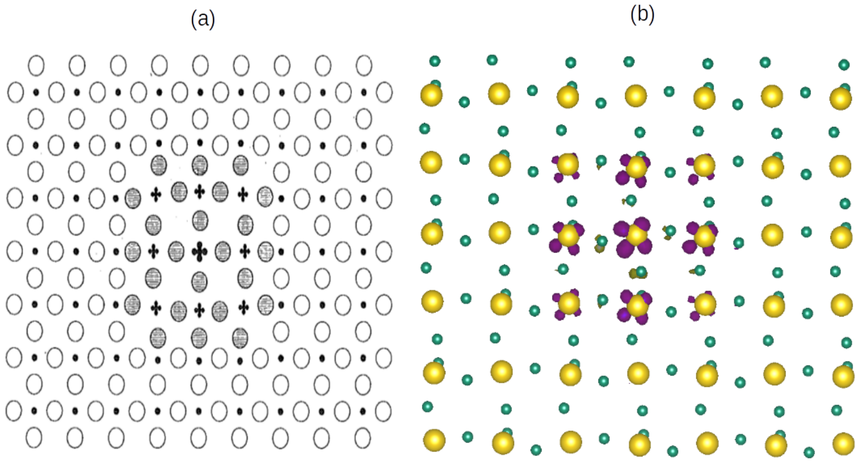

Fig. 5.6: *left figure, sketch of the polaron which extends over 9 tungten sites. Shown is the (ab) plane, the extension of the polaron along the c-axis is one unit cell, ie. the polaron is disc-shaped in the (ab) plane [4]. On the right figure we show our calculated spin density distribution of the polaron in the S6 supercell, which also shows a disc-shaped of the polaron in the a-b plane with the electron localized on the W-d xy orbitals.*

In Fig. 5.7 we show the total and d orbitals projected density of states around the tungsten holding the majority of the extra electron in the S4 supercell. By comparing with the $P2_1/c$ phase of pure WO_3 we find that the doping of one electron and its localization inside the system change the density states close to the Fermi level. Indeed, we can see in the band gap a narrow energy distribution associated with the extra electron state, which indicates the localization of this charge. This localization leads to an opening of a small electronic gap (0.05 eV) that separates the bottom of the conduction band from the Fermi level.

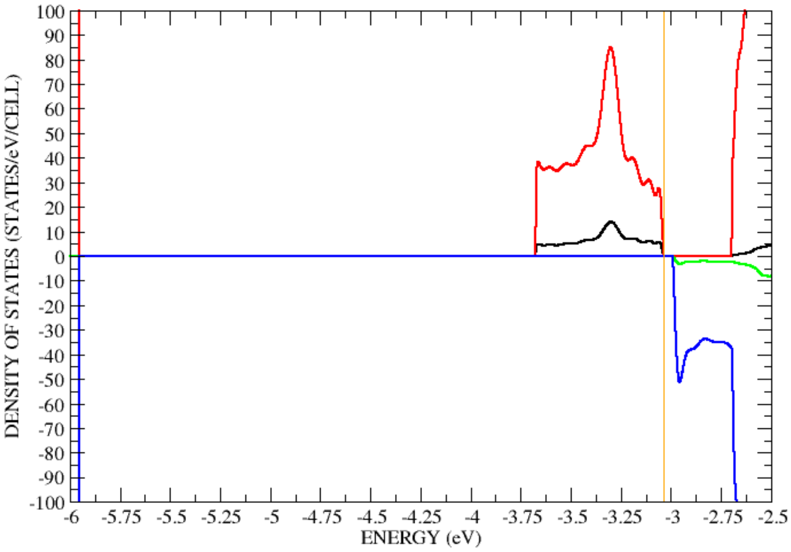

Fig. 5.7: *Calculated total and d orbitals projected density of states of the S4 supercell .*

5.5 Symmetry adapted mode analysis of the distorted supercells

We use the symmetry adapted mode decomposition, which is implemented in the AMPLIMODE software [55], to describe the structural distortions for S2 , S4 and S6 supercells of the monoclinic P2$_1$/c and cubic structures of WO_3, which are relaxed with different values of HF exact exchange mixing values. To quantify the structural distortions which appear in these structures, we project them onto symmetry adapted modes first for a parent the monoclinic P2$_1$/c structure and then for cubic structure. These two parent structures will define two complete basis for the atomic distortions of the distorted supercells.

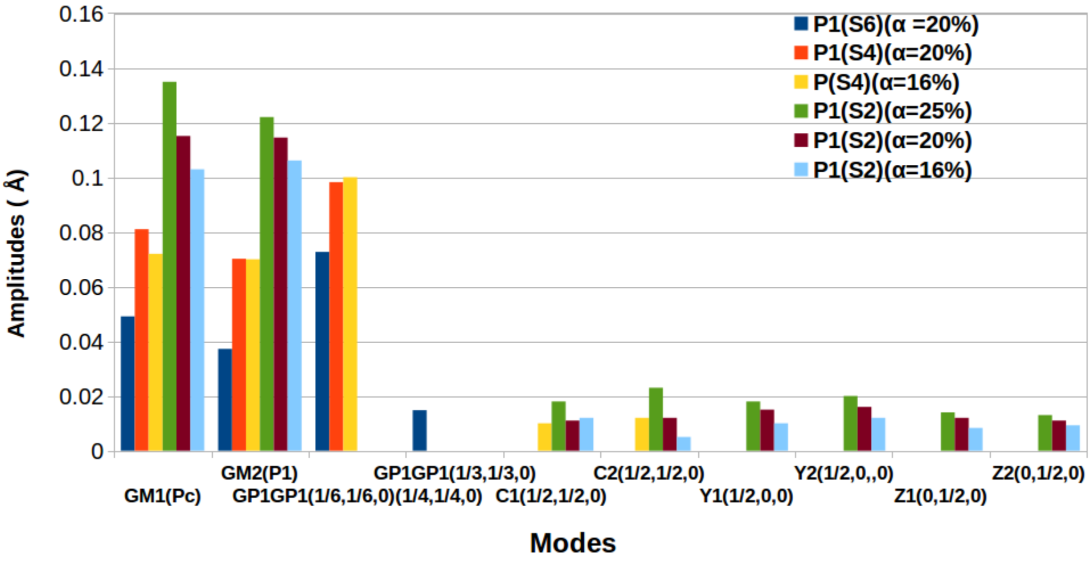

Fig. 5.8: *Symmetry adapted mode decomposition of distorted S2 , S4 and S6 supercells of the monoclinic* $P2_1/c$ *structure of* WO_3*, in which the pure monoclinic* $P2_1/c$ *structure modes are taken as a complete basis for the atomic distortions of these supercells.*

The projections of the structural distortions which correspond to the S2, S4, and S6 supercells relaxed with different HF exact exchange values, onto symmetry adapted modes, are given by Fig. 5.8 for the monoclinic $P2_1/c$ phase of WO_3. The graph shows the mode amplitude variations as a function of different supercell sizes and values of HF exact exchange mixing parameter.

The first thing to notice is the appearance of several of new phonon modes; GM1, GM2, GP1GP1 (1/4,1/4,0), GP1GP1 (1/6,1/6,0), GP1GP1 (1/3,1/3,0), C1, C2, Y1, Y2, Z1 and Z2, which are induced by the doped electron. The occurrence of these phonon modes depends on the supercell size, whereas their amplitudes depend on the HF exchange value.

The $\Gamma1$ phonon mode is a zone-center phonon mode but is not a polar mode. Its atomic displacements are given in Fig. 5.9, which shows oxygen octahedral rotations along [001] direction. This phonon mode can be quantified as an order parameter that can appear in the Landau free energy expansion. The $\Gamma1$ mode is invariant by all the symmetry transformation associated to the space group of the high-symmetry $P2_1/c$ structure and thus it will not break the symmetry. The atomic displacements corresponding to this mode represent the sum of all variations of the atomic displacement of the $P2_1/c$ phase due to the localization of the electron in the supercell of WO_3. Fig. 5.8 shows that the amplitude of the $\Gamma1$ mode depends

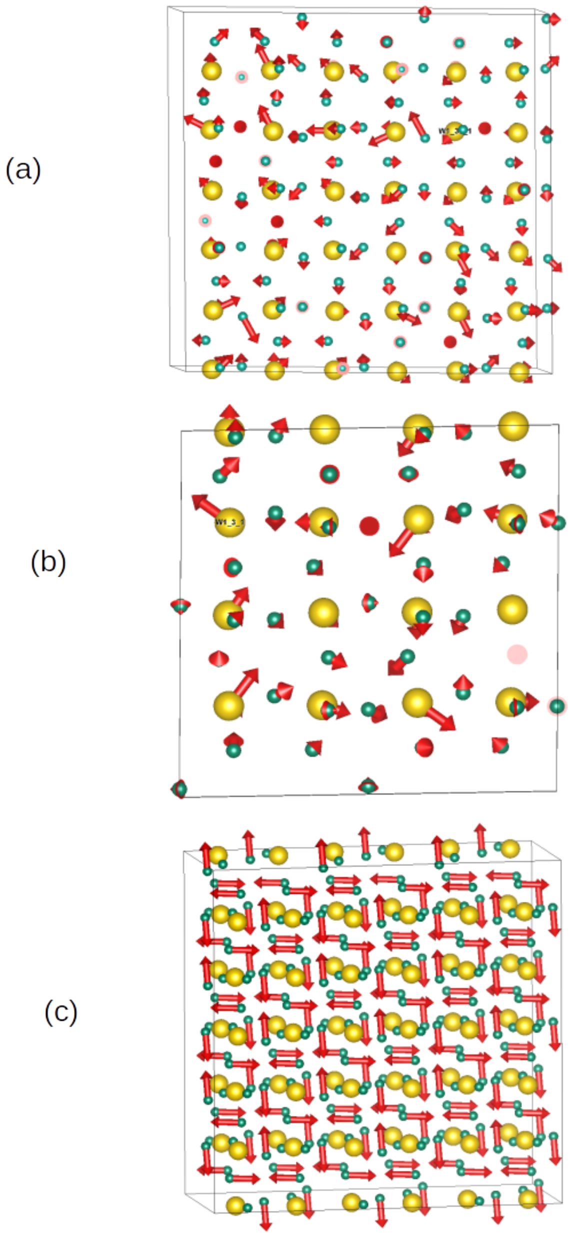

Fig. 5.9: *(a) GP1GP1 mode displacements in the S6 supercell, (b) GP1GP1 mode displacements in the S4 supercell and (c) GM1 invaraint mode displacements of the S6 supercell. All the displacements are given by the red arrows.*

at the same time on the size of the supercell and the percentage of the FH exchange: the smaller size of the supercell is, the bigger the HF exchange value is and the larger the $\Gamma 1$ amplitude is. It reaches its maximum value for the S2 supercell with 25% of HF exchange. A symmetry adapted mode decomposition of the structural distortions associated to the S2 , S4 and S6 supercells , for which the cubic structure is taken as a reference structure, is used to describe how the system changes its degrees of freedom due to the addition of an

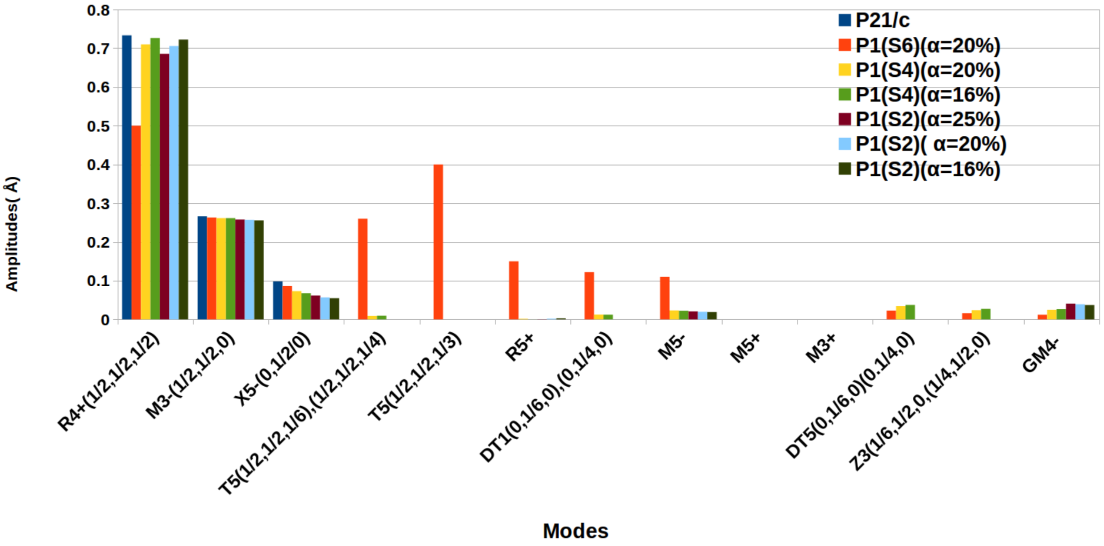

Fig. 5.10: *Symmetry adapted mode decomposition of distorted S2 , S4 and S6 supercells and bulk of the monoclinic $P2_1/c$ structure of WO_3, in which the cubic modes are taken as a complete basis for the atomic distortions of these supercells and bulk structure.*

extra electron with respect to the undoped case. Fig. A.1 shows the amplitudes of the modes in the relaxed S2, S4, and S6 supercells with distinct values of Hartree-Fock exact exchange (normalized with respect to the primitive unit cell of the high-symmetry cubic structure). The R_4^+ rotation pattern (the Glazer tilt pattern $a^-a^-c^-$) and M_3^- antipolar modes are the condensed modes (primary modes) of the pure $P2_1/c$ structure without an extra electron, whereas the presence of an other antipolar X_5^- mode (secondary mode) can be explained by trilinear coupling with the R_4^+ and M_3^- primary modes [5]. For the S2 supercell, the mode amplitude of the R_4^+ decreases by 1.5, 3.92 and 6.95 % with respect to the pure $P2_1/c$ structure for 16, 20 and 25% of HF exchange, respectively and for the S4 supercell, the mode amplitude of the R_4^+ decreases by 0.95, 3.19% with respect to the pure $P2_1/c$ structure for 20 and 25% of HF exchange, respectively. R_4^+ reaches its maximum reduction for the S6 supercell namely compared with previous smaller sizes of supercell, by 31.82% with respect to the pure $P2_1/c$ structure for 20% of HF exchange. This may be explained by an electronic effect coming from the partial localization of the extra electron, which is able to induce an oxygen octahedra rotate in the opposite sense with respect to those of the $P2_1/c$ phase in pure WO_3. This effect depends on the size of the supercell and also HF exchange. In the case of the largest supercell, the development of the polaronic state is more important than for the other smalls, and thus the oxygen rotations reduction obtain the largest value. The amplitude of the M_3^- antipolar mode remains almost constant around 0.26 Å for all the supercells with different values of HF exchange. For the X_5^- antipolar mode, its amplitude increases slightly by increasing either the HF exchange or size of the supercell but stays relatively small. The Γ_2 phonon mode is a polar mode, which has a displacement that depends on the size of the supercell. For the S2 and S4 supercells the atomic displacements related to this mode are identical (see Fig. 5.11).

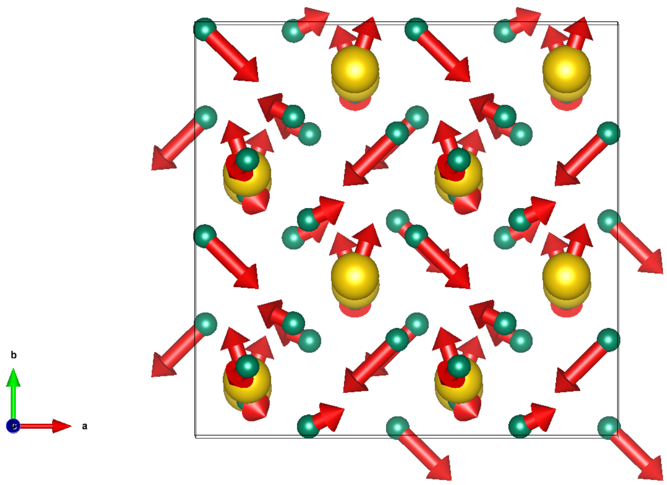

Fig. 5.11: *GM2 polar mode of the S2 supercell.*

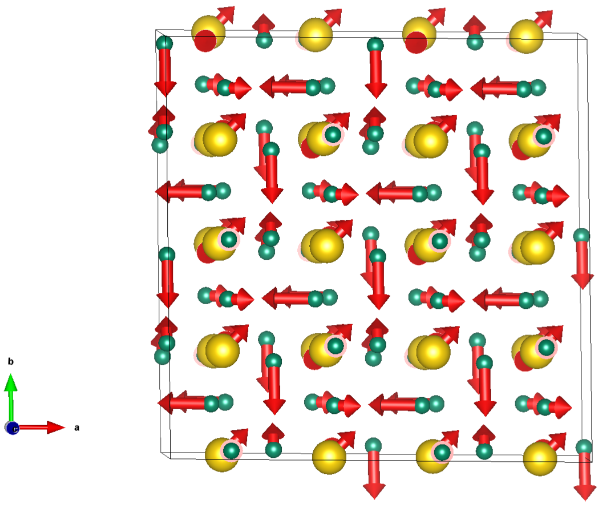

Fig. 5.12: *GM2 polar mode of the S4 supercell.*

For the S6 supercell, the Γ_2 atomic displacements are similar to those of the previous supercells but only some oxygens move along [110] direction as shown in Fig. 5.12.

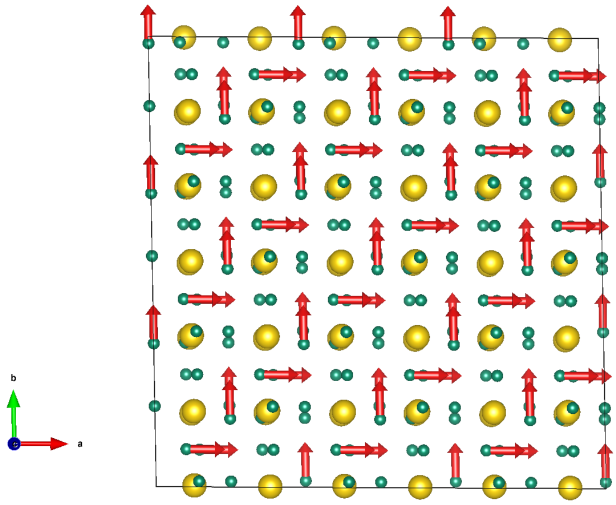

Fig. 5.13: *GM2 polar mode of the S6 supercell.*

The amplitude of the Γ_2 mode depends also at the same time on the supercell size and the HF exchange. More the size of the supercell is smaller and the HF exchange value is greater, more the Γ_2 amplitude is higher. For the S4 and S6 supercells, the amplitude of the Γ_2 mode decreases by 43 and 70% with respect to the S2 supercell.

The GP1GP1(1/4, 1/4, 0) and GP1GP1 (1/6, 1/6, 0) modes are the triggered modes following polaron development in the S4 and S6 supercells, respectively. The coordinates of these modes in the Brillouin zone indicate that they are not of high symmetry points. They have one irreducible representation with only the identity symmetry element, which yields the space group P1. Fig. 5.8 shows that the amplitude of these modes are much bigger than those of the Γ modes. The latter amplitudes decrease when the new triggered modes appear. In particular, the amplitude of the GP1GP1 mode decreases from the S4 to S6 supercell by 26%, while a new GP1GP1 mode at (1/3, 1/3 ,0) appears with smaller amplitude. For the atomic displacements related to these two modes, Fig. 5.9 shows the same atomic motions for the two modes, and, thus we may expect that these two modes couple with the electron. We conclude then that the localization of the charge activates a similar phonon at $q \propto (1/N, 1/N, 0)$ (N is the size of the supercell with respect to the pure cubic bulk structure), which tends to Γ by increasing N.

5.6 Conclusions

We have succeeded to determine a medium polaron in a region comparable to what is observed experimentally. To do that, we have increased slightly the mixing parameter α between 0.16 and 0.25 which might compensate the absence of zero point motions in our static calculations. The localization of the charge activated different distortions have been analysed with AMPLIMODE. On this basis, we have found that the dominant distortions involve the oxygen and tungsten motions at q $\propto$ (1/N, 1/N, 0) (N is the size of the supercell with respect to the cubic bulk structure of pure WO_3). Furthermore, we have identified two zone-center phonon modes; the Γ_1 mode, for which the atomic motions lead to relaxation of the $P2_1/c$ phase after the addition of an extra electron, and the Γ_2 mode, which is a polar mode that alows only some oxygens to move to break the inversion symmetry for the largest supercell S6. The presence of this polar mode lets us to predict that maybe doped WO_3 with one electron may be a ferroelectric material. This effect needs much more investigations to be validated.

At the level of our calculations, we have only focused on the symmetry mode analysis given by the AMPLIMODE software, which give us information about the symmetry of the phonon modes in the differents supercells of the $P2_1/c$ structure, but not on the phonon dispersion curves. This basic information can help us to analyze the electron-phonon coupling due to the localization of the polaron. Hopefully, we will be able to calculate the real polaron phonon modes in the future to understand the electron-phonon coupling and its properties behind.

It would be interesting for future to apply an electric field along different directions on the layer where the medium polaron is localized to see how this quasiparticle will move.

Chapter 6

Concluding Remarks and Perspectives

In the present thesis we presented first-principles studies of various metastable phases of pure bulk WO_3 and of medium polaron formation in this material. The main results are summarized as follows.

In Chapter 3, using first-principles density-functional calculations, we provided a detailed microscopic investigation of a variety of the structural phase transitions of WO_3. In the beginning, we calculated the electronic band gap of different phases of WO_3 with the B1-WC hybrid functional, which gives us very good agreement comparing with previous hybrid functional calculations (PBE0, HSE06, and B3LYP), GW calculations, and experimental measurements. This allowed us to continue to study of the structural properties of WO_3 using this functional. Therefore, we analyzed the intrinsic cubic phonon instabilities of this material, which gave us all the unstable modes in the cubic high-symmetry configuration and that are fundamental for explaining the stability of the distorted structures. We found the coexistence of different type of antiferrodistortive instabilities (antipolar cation motions, rotations, and tilts of oxygen octahedra) in all the phase transitions, that either compete with each other or cooperate together to lower the energy of the system. We clarified that the most dominant distortion in the ground state of WO_3 is the antipolar cation motions, which give rise to a $P2_1/c$ ground state structure. However, we also identified never observed R3m and R3c ferroelectric metastable phases with large polarizations and low energies close to the $P2_1/c$ ground state. This makes WO_3 a potential antiferroelectric material while a tiny polar distortion was experimentally observed at low temperature but not found in our calculation. We proposed that the absence of this small ferroelectricity in the ground state of WO_3 may be due its native defects that are associated to the oxygens vacancies and which are not taken into account in our DFT calculations.

In Chapter 4, we built upon previous work in which a fully first-principles scheme was used to study the properties of WO_3, but this time with the addition of a single electron in the monoclinic $P2_1/c$ ground state structure. The addition of this extra electron causes a local deformation in the supercell, which creates the self-trapping of this charge and that stabilizes a medium polaron in the supercell of WO_3. We then described the essential physical behavior of WO_3 in the presence of a medium polaron. These include the characterization of the medium polaron in the supercell of WO_3. We therefore reported a DFT study of the structural, electronic and lattice dynamic properties of the medium polaron in WO_3. We showed how our simple model calculation, can reproduce some aspects of the observed polaron behavior.

This present work gives a microscopic understanding of the origins of the observed structural phase diagrams of WO_3. In particular, a detailed understanding of the antiferroelectricity was provided to empathize the main underlying behavior of antiferroelectric materials at which WO_3 represents an ideal example for that. Furthermore, we have shown that making a medium polaron in the S6 supercell of WO_3 can produce large changes of the physical behavior of this material such as the structural, electronic, and lattice dynamic properties. Particularly, we observe the appearance of new phonon modes that are activated due to the localization of a medium polaron. The analysis of these activated polaron phonon modes will give us a basic idea about the electron-phonon coupling due to the single-electron interacting with the lattice deformation. Additionally, the appearance of an unexpected polar distortion in the polaron structure of WO_3 indicates that this martial may be becomes ferroelectric when we dope it with an electron. To assumme the possibility to develop the ferroelectricity inside of the doped WO_3 with electron, we need much more investigations.

Furthermore, if the presence of one single electron in the supercell of WO_3 changes its physical properties then what could happen if we consider the real defects which are the oxygen vacancies in WO_3? Here we get two extra electrons that will be given by one oxygen deficiency, which makes the bipolaron. Therefore, it will be of interest to study the bipolaron in WO_3 because we expect new functional properties.

Appendix A

Symmetry adapted mode analysis of the distorted supercells and Energy invariants

A.0.0.1 Symmetry adapted mode analysis of the distorted supercells: cubic reference

The results in Fig. A.1 show the amplitudes of the modes in the relaxed S2 , S4 , and S6 supercells with distinct values of Hartree-Fock exact exchange (normalized with respect to the primitive unit cell of the high-symmetry cubic structure).

The R_4^+ rotation pattern (the Glazer tilt pattern $a^-a^-c^-$) and M_3^- antipolar modes are already the condensed modes (primary modes) of the pure $P2_1/c$ structure without an extra electron, whereas the presence of an other antipolar X_5^- mode (secondary mode) can be explained by trilinear coupling with the R_4^+ and M_3^- primary modes [5].

Fig. A.1 shows that for the S2 supercell, the mode amplitude of the R_4^+ decreases by 1.5, 3.92 and 6.95 % with respect to the pure $P2_1/c$ structure for 16, 20 and 25% of HF exchange, resepectively. For the S4 supercell, the mode amplitude of the R_4^+ decreases by 0.95, 3.19% with respect to the pure $P2_1/c$ structure for 20 and 25% of HF exchange, respectively. However, for the S6 supercell the R_4^+ reaches its maximum reduction, compared to previous smaller sizes of supercell, by 31.82% with respect to the pure $P2_1/c$ structure for 20% of HF exchange. This may can be explained by an electronic effect coming from the partially localization of the extra electron, which is able to make the oxygen octahedra rotate on the opposite direction with respect to those of the pure $P2_1/c$ phase. This effect depends on the size of the supercell and

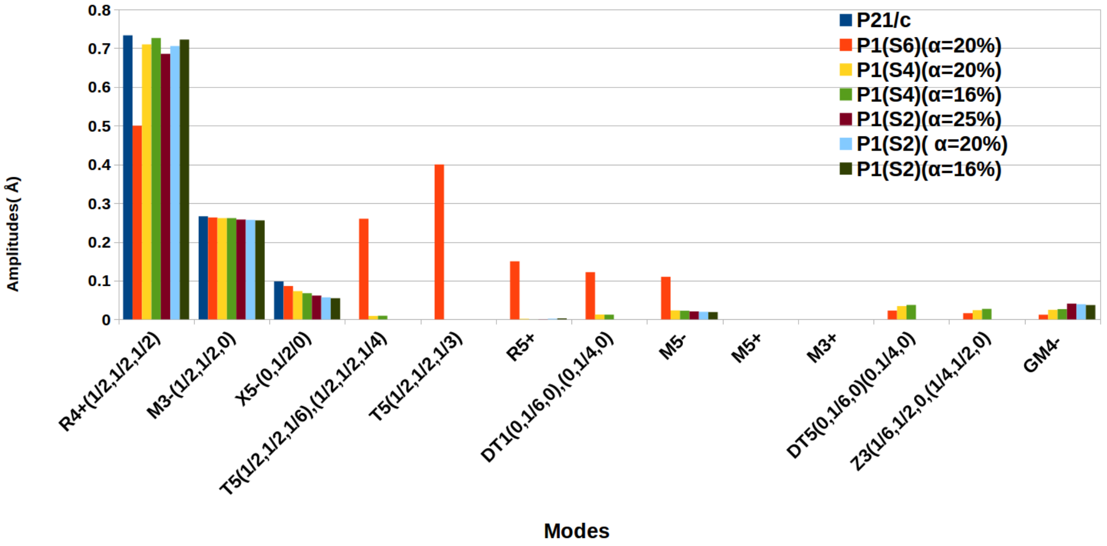

Fig. A.1: *Symmetry adapted mode decomposition of distorted S2 , S4 and S6 supercells and bulk of the monoclinic $P2_1/c$ structure of WO_3, in which the cubic modes are taken as a complete basis for the atomic distortions of these supercells and bulk structure.*

also the HF exchange. In the case of the largest supercell, the development of the polaronic state is more important than for the other smalls, and thus the oxygen rotations reduction achieves its largest value.

However for the M_3^- antipolar mode, its amplitude remains almost constant around 0.26 A for all the supercells with different values of HF exchange. For the X_5^- antipolar mode, its amplitude increases slightly by increasing either the HF exchange or size of the supercell but it's stay relatively small.

Despite the persistence of the frozen phonon modes in the $P2_1/c$ supercell, new modes are triggered during the process of the development of the polaron. The most important ones are those that appear in the S6 supercell at which the polaron has enough space to be built. In this supercell, two modes with the same irreducible representation T5 at two different points in the Brillouin zone (1/2, 1/2, 1/6) and (1/2, 1/2, 1/3) occur with the largest amplitudes compared to the rest of the activated modes. The amplitude of the T5 mode with the coordinates (1/2, 1/2, 1/3) is bigger than the M_3^- frozen phonon mode by 50%, whereas the amplitude of the T5 mode with the coordinates (1/2, 1/2, 1/6) is smaller than the T5 mode with the coordinates (1/2, 1/2, 1/3) by 35%. However, the amplitude of the T5 mode with the coordinates (1/2, 1/2, 1/4) in the Brillouin zone of the S4 supercell is small 0.009A. The atomic displacements associated to these three modes of the same irreducible representation T5 are given by Fig. A.2

and Fig. A.3, which show a similarity in the displacements that are driven only by the oxygens for the three modes. This may mean that the T5 modes are in the same phonon branch.

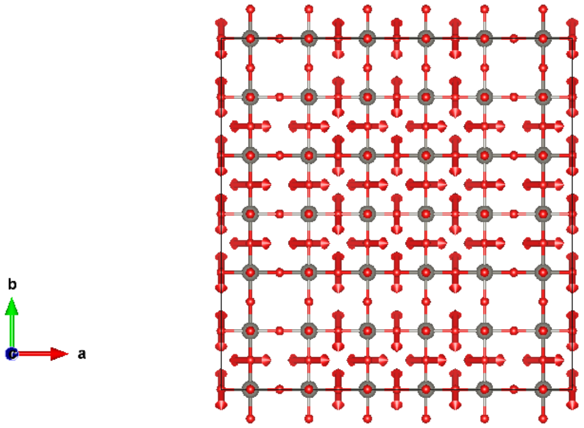

Fig. A.2: *T5(1) mode in the S6 supercell*

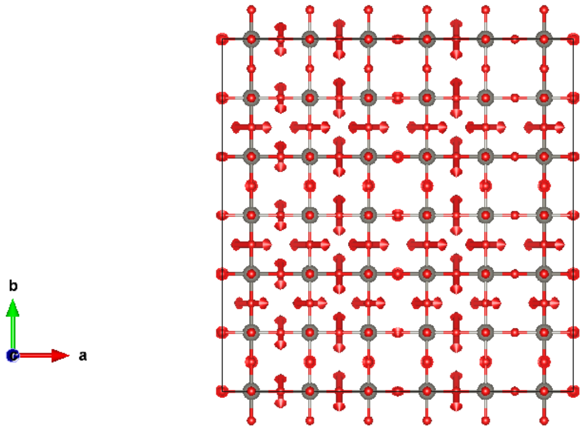

Fig. A.3: *T5(2) mode in the S6 supercell*

Among these new modes, we find the R5+ mode with an amplitude that is 37.5% of the amplitude of the T5 mode with the coordinates (1/2, 1/2, 1/3). Its atomic displacements are given by Fig. A.4, which shows distorted oxygen octahedral rotations along the [111] direction.

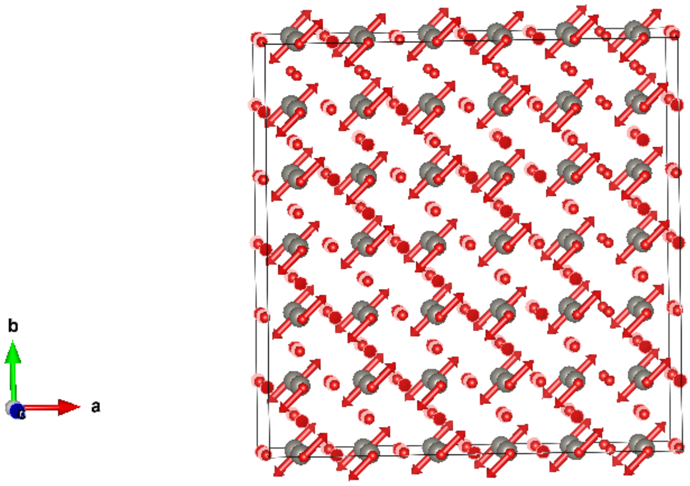

Fig. A.4: *R5+ mode in the S6 supercell*

The DT1 mode has the same irreducible representation for two different points in the Brillouin zone with coordinates (0, 1/6, 0) and (0, 1/4, 0) for the two S6 and S4 supecell, repetitively. The amplitude of DT1 mode with coordinates (0, 1/6, 0) is much larger than that of the coordinates (0, 1/4, 0) and it 30% of the amplitude of the T5 mode with the coordinates (1/2, 1/2, 1/3). Its atomic displacements are given by Fig. A.6, which shows the displacements of the tungstens only. The M5- mode has an amplitude which represents 27.5% of the amplitude of the T5 mode with the coordinates (1/2, 1/2, 1/3). The atomic displacements related to this mode is given by Fig. A.5, in which we can see similarity between its displacements and that for the T5 modes.

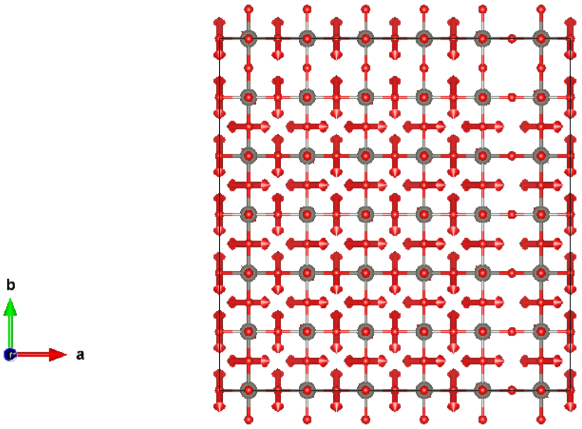

Fig. A.5: *M5- mode in the S6 supercell*

A polar Γ_4^- mode has been activated in all the supercells. Its amplitude is smaller compared with those of the triggered modes (3% of the amplitude of the T5 mode with the coordinates (1/2, 1/2, 1/3)); it reaches its maximum value for the S2 supercell with 25% of HF exchange and decreases with increasing supercell size. The minimum value of the amplitude of the Γ_4^- is achieved for the S6 supercell. This amplitude variation of the Γ_4^- mode is affected by the size of the supercell, as well as by the HF exchange value. The origin of the appearance of the polar mode can be understood and explained by different points of view, may be the most convincing one is through the coupling with the triggered modes. All the possible coupling with the Γ_4^- polar mode will be provided in the next section.

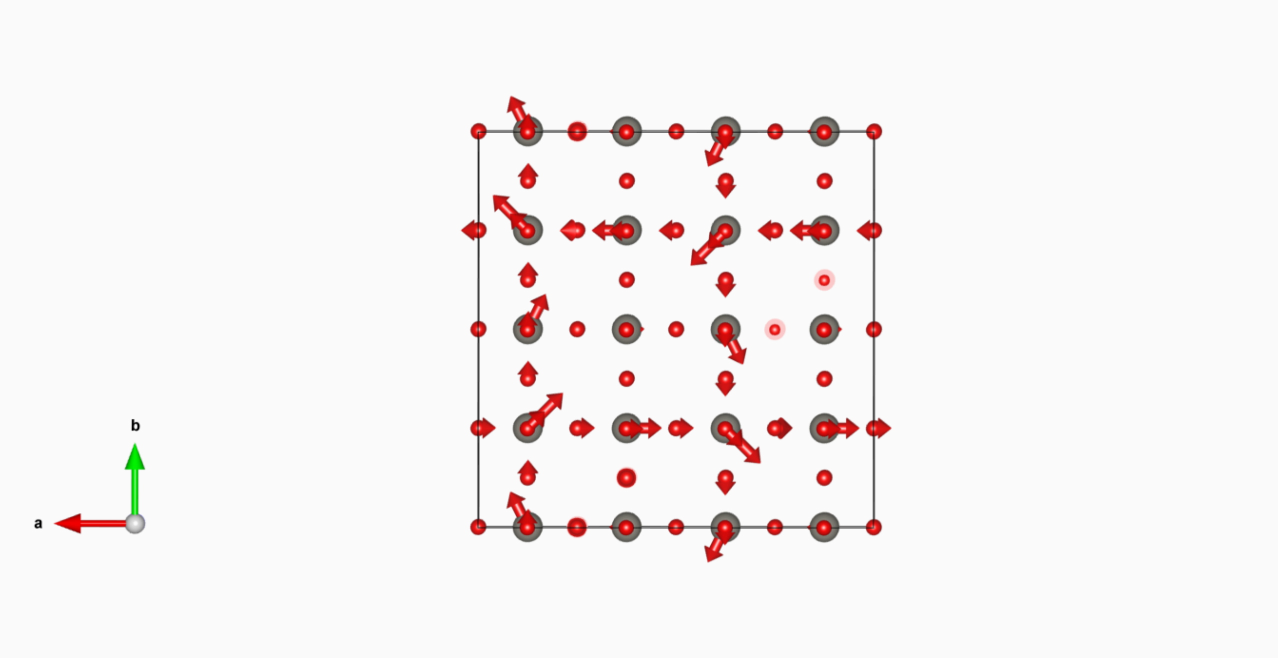

Fig. A.6: *DT5 mode in the S6 supercell*

A.0.1 Energy invariants

The pure monoclinic P2$_1$/c phase arises from the condensation of the R_4^+ and M_3^- two unstable modes (primary modes) of the cubic parent structure, which includes also the X_5^- additional mode (secondary modes) with significant amplitude. However, the appearance of some of the polaron modes with different amplitude can be traced back in their linear coupling either with the dominant polaron modes as T5 modes or with also additional modes. This can be justified from the existence in the energy expansion of the $Pm\bar{3}m$ phase of invariant terms of the form $\gamma Q_{s_k} \prod_{i=1}^{N} Q^i_{p_k}$ where Q_s is the amplitude of the secondary mode s and Q^i_p could be either the amplitude of the dominant polaron mode or a secondary mode i.

In order to clarify the origin of some polaron modes in the S6 P1 relaxed supercell of WO$_3$, we restrict ourselves here to the search of such multilinear invariant terms in the energy expansion around its cubic phase by using the INVARIANTS software [82]. In the last column of Table II we report these linear invariants up to the fourth order. The letters represent the mode amplitudes (Q^i) in the directions specified in the third column where the bold letters refer to the primary modes in the structure (Q_s) and the normal letters refer to secondary modes (Q_p^i). The Γ_4^- polar mode appears through trilinear and quadrilinear couplings. The most important coupling here is that for quadrilinear couplings with one component of the M_5^- mode and two components of M_3^- mode ($\mathbf{a}\mathbf{b}'\mathbf{c}'b''$ $+\mathbf{b}\mathbf{b}'\mathbf{c}'a''+\mathbf{c}\mathbf{a}'\mathbf{c}'a''+\mathbf{d}\mathbf{b}'\mathbf{c}'c''+\mathbf{e}\mathbf{a}'\mathbf{b}'c''+\mathbf{f}\mathbf{a}'\mathbf{b}'b''$ invariant in Table A.1). This polar mode can also appears through quadrilinear couplings with three components of the M_5^- mode or one component of the M_5^- mode and either two components of X_5^- or Z_3 or M_3^- modes (see Table A.1). In addition, the M_5^- appears also through a quadrilinear coupling with three components of the T_5 mode. This T_5 mode does not couple with any of the others polaron modes and has the largest amplitude compared to the rest of these particulars modes, this means that the T_5 mode is likely activated when the polaron is formed.

Table A.1: *Symmetry adapted modes decomposition and linear couplings of modes of the P1 S6 supercell phase. From the left to right columns, we show the mode label (Irrep.) of the symmetry adapted mode, the direction of the mode condensation, the corresponding subgroup, the amplitude of the distortion in the calculated and the linear coupling invariants of the most relevant modes where the letters correspond to the one given in the direction column (we highlight in bold the primary modes)*

Space group	Irrep.	Direction	Subgroup	Amplitudes (Å)	Linear Invariants
$P1$	$\mathbf{M}_5^-$	$(\mathbf{a},\mathbf{b},\mathbf{c},\mathbf{d},\mathbf{e},\mathbf{f})$	$P1$	0.11	$\mathbf{aa}'\mathrm{a}''-\mathbf{bb}'\mathrm{a}''+\mathbf{cc}'\mathrm{b}''-\mathbf{da}'\mathrm{b}''+\mathbf{eb}'\mathrm{c}''-\mathbf{fc}'\mathrm{c}^{P''}$
	$\mathbf{M}_2^+$	$(\mathbf{a}',\mathbf{b}',\mathbf{c}')$	$Immm$	0.0022	
	Γ_4^-	$(\mathrm{a}'',\mathrm{b}'',\mathrm{c}'')$	P1	0.012	
$P1$	$\mathbf{M}_5^-$	$(\mathbf{a},\mathbf{b},\mathbf{c},\mathbf{d},\mathbf{e},\mathbf{f})$	$P1$	0.11	$\mathbf{acf}\mathrm{a}''+\mathbf{ade}\mathrm{b}''+\mathbf{adf}\mathrm{c}''+\mathbf{bce}\mathrm{c}''+\mathbf{bdf}\mathrm{b}''+\mathbf{bde}\mathrm{a}''$
	Γ_4^-	$(\mathrm{a}'',\mathrm{b}'',\mathrm{c}'')$	P1	0.012	
$P1$	$\mathbf{M}_5^-$	$(\mathbf{a},\mathbf{b},\mathbf{c},\mathbf{d},\mathbf{e},\mathbf{f})$	$P1$	0.11	
	$\mathbf{X}_5^-$	$(\mathbf{a}',\mathbf{b}',\mathbf{c}')$	P-1	0.086	$\mathbf{ab}'\mathbf{c}'\mathrm{b}''+\mathbf{bb}'\mathbf{c}'\mathrm{a}''+\mathbf{cd}'\mathbf{e}'\mathrm{a}''+\mathbf{dd}'\mathbf{e}'\mathrm{c}''+\mathbf{ea}'\mathbf{f}'\mathrm{c}''+\mathbf{fa}'\mathbf{f}'\mathrm{b}''$
	Γ_4^-	$(\mathrm{a}'',\mathrm{b}'',\mathrm{c}'')$	P1	0.012	
$P1$	$\mathbf{M}_5^-$	$(\mathbf{a},\mathbf{b},\mathbf{c},\mathbf{d},\mathbf{e},\mathbf{f})$	$P1$	0.11	$\mathbf{ca}'\mathbf{e}'\mathrm{a}''+\mathbf{ab}'\mathbf{f}'\mathrm{b}''+\mathbf{db}'\mathbf{f}'\mathrm{c}''$
	$\mathbf{Z}_3$	$(\mathbf{a}',\mathbf{b}',\mathbf{c}',\mathbf{d}',\mathbf{e}',\mathbf{f}')$	P1	0.016	$+\mathbf{ec}'\mathbf{g}'\mathrm{c}''+\mathbf{ed}'\mathbf{h}'\mathrm{c}''+\mathbf{fc}'\mathbf{h}'\mathrm{b}''$
	Γ_4^-	$(\mathrm{a}'',\mathrm{b}'',\mathrm{c}'')$	P1	0.012	$+\mathbf{fd}'\mathbf{h}'\mathrm{b}''+\mathbf{da}'\mathbf{e}'\mathrm{c}''$
$P1$	$\mathbf{M}_5^-$	$(\mathbf{a},\mathbf{b},\mathbf{c},\mathbf{d},\mathbf{e},\mathbf{f})$	$P1$	0.11	$\mathbf{dc}'\mathrm{a}''-\mathbf{ec}'\mathrm{a}''$
	$\mathbf{M}_3^-$	$(\mathbf{a}',\mathbf{b}',\mathbf{c}')$	I222	0.26	$+\mathbf{ac}'\mathrm{b}''+\mathbf{ea}'\mathrm{b}''$
	M_2^+	$(\mathrm{a},\mathrm{b}'',\mathrm{c}'')$	$Immm$	0.0022	$+\mathbf{bb}'\mathrm{c}''-\mathbf{ca}'\mathrm{c}''$
$P1$	$\mathbf{T}_5$	$(0,0,0,0,\mathbf{a},\mathbf{b},\mathbf{c},\mathbf{d},\mathbf{e},\mathbf{f},\mathbf{g},\mathbf{h})$	$P1$	0.26	$\mathbf{a}^3\mathrm{c}''+3\mathbf{a}^2\mathbf{c}\mathrm{c}''-3\mathbf{ac}^2\mathrm{c}''+\mathbf{c}^3\mathrm{c}''-\mathbf{b}^3\mathrm{d}''-3\mathbf{b}^2\mathbf{d}\mathrm{d}''$
	M_5^-	$(\mathrm{a}'',\mathrm{b}'',\mathrm{c}'',\mathrm{d}'',\mathrm{e}'',\mathrm{f}'')$	P1	0.11	$-2\mathbf{efg}\mathrm{f}'+-2\mathbf{egh}\mathrm{f}'-2\mathbf{bcd}\mathrm{c}'-\mathbf{g}^2\mathbf{h}\mathrm{f}'-\mathbf{g}^2\mathbf{f}\mathrm{f}'$
$P1$	$\mathbf{M}_5^-$	$(\mathbf{a},\mathbf{b},\mathbf{c},\mathbf{d},\mathbf{e},\mathbf{f})$	$P1$	0.11	
	$\mathbf{M}_3^-$	$(\mathbf{a}',\mathbf{b}',\mathbf{c}')$	I222	0.26	
	Γ_4^-	(a'',b'',c'')	P1	0.012	$\mathbf{ab}'\mathbf{c}'b''+\mathbf{bb}'\mathbf{c}'a''+\mathbf{ca}'\mathbf{c}'a''+\mathbf{db}'\mathbf{c}'c''+\mathbf{ea}'\mathbf{b}'c''+\mathbf{fa}'\mathbf{b}'b''$

References

[1] T. Vogt, P. M. Woodward, and B. A. Hunter, "The High-Temperature Phases of WO3," *Journal of Solid State Chemistry*, vol. 144, no. 1, pp. 209–215, 1999.

[2] K. R. Locherer, I. P. Swainson, and E. K. H. Salje, "Phase transitions in tungsten trioxide at high temperatures - a new look," *Journal of Physics: Condensed Matter*, vol. 11, no. 35, p. 6737, 1999.

[3] C. J. Howard, V. Luca, and K. S. Knight, "High-temperature phase transitions in tungsten trioxide - the last word?," *Journal of Physics: Condensed Matter*, vol. 14, no. 3, p. 377, 2002.

[4] E.K.H.Salje, *"Polarons and bipolarons in tungsten oxide, WO3-x", Inorg.Chem vol 31, pp.805-821.* 1994.

[5] H. Hamdi, E. K. H. Salje, P. Ghosez, and E. Bousquet, "First-principles reinvestigation of bulk WO_3," *Phys. Rev. B*, vol. 94, p. 245124, Dec 2016.

[6] A. Katrusiak and A. Ratuszna, "Phase transitions and the structure of NaMnF3 perovskite crystals as a function of temperature and pressure," *Solid State Communications*, vol. 84, no. 4, pp. 435–441, 1992.

[7] G. Shirane, E. Sawaguchi, and Y. Takagi, "Dielectric properties of lead zirconate," *Phys. Rev.*, vol. 84, pp. 476–481, Nov 1951.

[8] R. M. D. Eberhard Engel. 2011.

[9] H. Fujishita, Y. Ishikawa, S. Tanaka, A. Ogawaguchi, and S. Katano, "Crystal Structure and Order Parameters in the Phase Transition of Antiferroelectric PbZrO3," *Journal of the Physical Society of Japan*, vol. 72, no. 6, pp. 1426–1435, 2003.

[10] G. Shirane, "Ferroelectricity and antiferroelectricity in ceramic pbzro$_3$ containing ba or sr," *Phys. Rev.*, vol. 86, pp. 219–227, Apr 1952.

[11] K. M. Rabe, *Antiferroelectricity in Oxides: A Reexamination*, pp. 221–244. Wiley-VCH Verlag GmbH and Co. KGaA, 2013.

[12] X. Gonze and *et al.*, "ABINIT: First-principles approach to material and nanosystem properties," *Computer Physics Communications*, vol. 180, no. 12, pp. 2582–2615, 2009.

[13] E. lje, "The electrochromic effect in polar wo3," *Optics Communications*, vol. 24, no. 2, pp. 231 – 232, 1978.

[14] G. A. Niklasson and C. G. Granqvist, "Electrochromics for smart windows: thin films of tungsten oxide and nickel oxide, and devices based on these," *J. Mater. Chem.*, vol. 17, pp. 127–156, 2007.

[15] S. K. Deb, "Opportunities and challenges in science and technology of wo3 for electrochromic and related applications," *Solar Energy Materials and Solar Cells*, vol. 92, no. 2, pp. 245 – 258, 2008. Selected Papers from the Seventh International Meeting on Electrochromism (IME-7)Seventh International Meeting on Electrochromism.

[16] R. Baetens, B. P. Jelle, and A. Gustavsen, "Properties, requirements and possibilities of smart windows for dynamic daylight and solar energy control in buildings: A state-of-the-art review," *Solar Energy Materials and Solar Cells*, vol. 94, no. 2, pp. 87 – 105, 2010.

[17] S.-H. Lee, R. Deshpande, P. Parilla, K. Jones, B. To, A. Mahan, and A. Dillon, "Crystalline wo3 nanoparticles for highly improved electrochromic applications," *Advanced Materials*, vol. 18, no. 6, pp. 763–766, 2006.

[18] A. Subrahmanyam and A. Karuppasamy, "Optical and electrochromic properties of oxygen sputtered tungsten oxide (wo3) thin films," *Solar Energy Materials and Solar Cells*, vol. 91, no. 4, pp. 266 – 274, 2007.

[19] C. Sella, M. Maaza, O. Nemraoui, J. Lafait, N. Renard, and Y. Sampeur, "Preparation, characterization and properties of sputtered electrochromic and thermochromic devices," *Surface and Coatings Technology*, vol. 98, no. 1-3, pp. 1477 – 1482, 1998. Papers presented at the Fifth International Conference on Plasma Surface Engineering.

[20] Y. Zhao, Z. C. Feng, Y. Liang, and H. W. Sheng, “Laser-induced coloration of WO_3,” *Applied Physics Letters*, vol. 71, pp. 2227–2229, Oct. 1997.

[21] A. Aird and E. K. H. Salje *Journal of Physics: Condensed Matter*, vol. 10, no. 22, p. L377, 1998.

[22] A. Aird, M. C. Domeneghetti, F. Mazzi, V. Tazzoli, and E. K. H. Salje, “Sheet superconductivity in WO_{3-x} : crystal structure of the tetragonal matrix,” *Journal of Physics: Condensed Matter*, vol. 10, no. 33, p. L569, 1998.

[23] E. Salje, “Structural phase transitions in the system WO3-NaWO3,” *Ferroelectrics*, vol. 12, no. 1, pp. 215–217, 1976.

[24] A. Shengelaya, S. Reich, Y. Tsabba, and K. Müller, “Electron spin resonance and magnetic susceptibility suggest superconductivity in Na doped WO3samples,” *The European Physical Journal B - Condensed Matter and Complex Systems*, vol. 12, no. 1, pp. 13–15.

[25] V. Barzykin and L. P. Gorkov, “Inhomogeneous Stripe Phase Revisited for Surface Superconductivity,” *Phys. Rev. Lett.*, vol. 89, p. 227002, Nov 2002.

[26] Y. Kim, M. Alexe, and E. K. H. Salje, “Nanoscale properties of thin twin walls and surface layers in piezoelectric wo3âĹŠx,” *Applied Physics Letters*, vol. 96, no. 3, 2010.

[27] Granqvist C.G, “Electrochromic tungsten oxide films: Review of progress 1993–1998,” *Solar Energy Materials and Solar Cells*, vol. 60, pp. 201–262, jan 2000.

[28] Gillaspie Dane T., Tenent Robert C., and Dillon Anne C., “Metal-oxide films for electrochromic applications: present technology and future directions,” *Journal of Materials Chemistry*, vol. 20, no. 43, pp. 9585–9592, 2010.

[29] E. Salje and K. Viswanathan, “Physical properties and phase transitions in WO_3,” *Acta Crystallographica Section A*, vol. 31, pp. 356–359, May 1975.

[30] E. Salje, “Lattice dynamics of WO_3,” *Acta Crystallographica Section A*, vol. 31, pp. 360–363, May 1975.

[31] K. R. Locherer, I. P. Swainson, and E. K. H. Salje, “Transition to a new tetragonal phase of wo3 : crystal structure and distortion parameters,” *Journal of Physics: Condensed Matter*, vol. 11, no. 21, p. 4143, 1999.

[32] E. K. H. Salje, S. Rehmann, F. Pobell, D. Morris, K. S. Knight, T. Herrmannsdlöfer, and M. T. Dove *Journal of Physics: Condensed Matter*, vol. 9, no. 31, p. 6563, 1997.

[33] M. Boulova, N. Rosman, P. Bouvier, and G. Lucazeau, "High-pressure raman study of microcrystalline wo 3 tungsten oxide," *Journal of Physics: Condensed Matter*, vol. 14, no. 23, p. 5849, 2002.

[34] R. Diehl, G. Brandt, and E. Salje, "The crystal structure of triclinic WO_3," *Acta Crystallographica Section B*, vol. 34, pp. 1105–1111, Apr 1978.

[35] P. Woodward, A. Sleight, and T. Vogt, "Structure refinement of triclinic tungsten trioxide," *Journal of Physics and Chemistry of Solids*, vol. 56, no. 10, pp. 1305 – 1315, 1995.

[36] P. Woodward, A. Sleight, and T. Vogt, "Ferroelectric tungsten trioxide," *Journal of Solid State Chemistry*, vol. 131, no. 1, pp. 9 – 17, 1997.

[37] S. Tanisaki, "Crystal structure of monoclinic tungsten trioxide at room temperature," *Journal of the Physical Society of Japan*, vol. 15, no. 4, pp. 573–581, 1960.

[38] B. O. Loopstra and P. Boldrini, "Neutron diffraction investigation of WO_3," *Acta Crystallographica*, vol. 21, pp. 158–162, Jul 1966.

[39] W. L. Kehl, R. G. Hay, and D. Wahl, "The structure of tetragonal tungsten trioxide," *Journal of Applied Physics*, vol. 23, no. 2, pp. 212–215, 1952.

[40] S. K. Deb, "Opportunities and challenges in science and technology of wo3 for electrochromic and related applications," *Solar Energy Materials and Solar Cells*, vol. 92, no. 2, pp. 245 – 258, 2008. Selected Papers from the Seventh International Meeting on Electrochromism (IME-7)Seventh International Meeting on Electrochromism.

[41] A. Aird, M. C. Domeneghetti, F. Mazzi, V. Tazzoli, and E. K. H. Salje, "Sheet superconductivity in : crystal structure of the tetragonal matrix," *Journal of Physics: Condensed Matter*, vol. 10, no. 33, p. L569, 1998.

[42] O. Schirmer and E. Salje, "The w5+ polaron in crystalline low temperature wo3 esr and optical absorption," *Solid State Communications*, vol. 33, no. 3, pp. 333 – 336, 1980.

[43] O. F. Schirmer and E. Salje, “Conduction bipolarons in low-temperature crystalline wo 3-x,” *Journal of Physics C: Solid State Physics*, vol. 13, no. 36, p. L1067, 1980.

[44] E. Salje, A. Carley, and M. Roberts, “The effect of reduction and temperature on the electronic core levels of tungsten and molybdenum in wo3 and wxmo1âĹŠxo3âĂŤa photoelectron spectroscopic study,” *Journal of Solid State Chemistry*, vol. 29, no. 2, pp. 237 – 251, 1979.

[45] E. Salje and B. GÃijttler, “Anderson transition and intermediate polaron formation in wo3-x transport properties and optical absorption,” *Philosophical Magazine Part B*, vol. 50, no. 5, pp. 607–620, 1984.

[46] S. K. Deb, “Opportunities and challenges in science and technology of {WO3} for electrochromic and related applications,” *Solar Energy Materials and Solar Cells*, vol. 92, no. 2, pp. 245–258, 2008. Selected Papers from the Seventh International Meeting on Electrochromism (IME-7)Seventh International Meeting on Electrochromism.

[47] F. Wang, C. Di Valentin, and G. Pacchioni, “Semiconductor-to-metal transition in WO_{3-x}: Nature of the oxygen vacancy,” *Phys. Rev. B*, vol. 84, p. 073103, Aug 2011.

[48] S. K. Deb, “Optical and photoelectric properties and colour centres in thin films of tungsten oxide,” *Philosophical Magazine*, vol. 27, no. 4, pp. 801–822, 1973.

[49] N. Bondarenko, O. Eriksson, and N. V. Skorodumova, “Polaron mobility in oxygen-deficient and lithium-doped tungsten trioxide,” *Phys. Rev. B*, vol. 92, p. 165119, Oct 2015.

[50] J. Heyd, G. E. Scuseria, and M. Ernzerhof, “Hybrid functionals based on a screened Coulomb potential,” *The Journal of Chemical Physics*, vol. 118, no. 18, pp. 8207–8215, 2003.

[51] J. Heyd and G. E. Scuseria, “Assessment and validation of a screened Coulomb hybrid density functional,” *The Journal of Chemical Physics*, vol. 120, no. 16, pp. 7274–7280, 2004.

[52] G. VENKATARAN, “Soft modes and structural phase transitions, bull. mater.sci., vol. 1, numbers 3 and 4, december 1979, pp. 129-170,” *Eur.J.Solid StateInorg.Chem.*, vol. 118, 2003.

[53] W. Cochran, "Crystal stability and the theory of ferroelectricity," *Advances in Physics*, vol. 9, no. 36, pp. 387–423, 1960.

[54] R. M. Pick, M. H. Cohen, and R. M. Martin, "Microscopic theory of force constants in the adiabatic approximation," *Phys. Rev. B*, vol. 1, pp. 910–920, Jan 1970.

[55] D. Orobengoa, C. Capillas, M. I. Aroyo, and J. M. Perez-Mato, "*AMPLIMODES*: symmetry-mode analysis on the Bilbao Crystallographic Server," *Journal of Applied Crystallography*, vol. 42, pp. 820–833, Oct 2009.

[56] M. E. Lines and A. M. Glass, *"Principles and Applications of Ferroelectrics and Related Materials", Book, 2011.* 1994.

[57] E. C. Subbarao, "Ferroelectric and antiferroelectric materials," *Ferroelectrics*, vol. 5, no. 1, pp. 267–280, 1973.

[58] C. Kittel, "Theory of antiferroelectric crystals," *Phys. Rev.*, vol. 82, pp. 729–732, Jun 1951.

[59] R. Blinc, *Soft Modes in Ferroelectrics and Antiferroelectrics, Blinc, R, North-Holland 1974.* 1994.

[60] U. V. Waghmare and K. M. Rabe, "Lattice instabilities, anharmonicity and phase transitions in PbZrO3 from first principles," *Ferroelectrics*, vol. 194, no. 1, pp. 135–147, 1997.

[61] B. D. Hongbo Liu

[62] K. Roleder, G. E. Kugel, J. Handerek, M. D. Fontana, C. Carabatos, M. Hafid, and A. Kania, "The first evidence of two phase transitions in PbZrO3 crystals derived from simultaneous raman and dielectric measurements," *Ferroelectrics*, vol. 80, no. 1, pp. 161–164, 1988.

[63] S. E. Reyes-Lillo, K. F. Garrity, and K. M. Rabe, "Antiferroelectricity in thin-film zro_2 from first principles," *Phys. Rev. B*, vol. 90, p. 140103, Oct 2014.

[64] Kohanoff, *Electronic Structure Calculations for Solids and Molecules, Book, 2006*, pp. 221–244. Wiley-VCH Verlag GmbH and Co. KGaA, 1994.

[65] D. I. Bilc, R. Orlando, R. Shaltaf, G.M Rignanese, J. Íñiguez, and Ph. Ghosez, "Hybrid exchange-correlation functional for accurate prediction of the electronic and structural properties of ferroelectric oxides," *Phys. Rev. B*, vol. 77, p. 165107, Apr 2008.

[66] M. Caus, R. Dovesi, C. Pisani, R. Colle, and A. Fortunelli, "Correlation correction to the Hartree-Fock total energy of solids," *Phys. Rev. B*, vol. 36, pp. 891–897, Jul 1987.

[67] D. Figgen, K. A. Peterson, M. Dolg, and H. Stoll, "Energy-consistent pseudopotentials and correlation consistent basis sets for the 5d elements hfâĂŞpt," *The Journal of Chemical Physics*, vol. 130, no. 16, 2009.

[68] F. Pascale, C. M. Zicovich-Wilson, F. López Gejo, B. Civalleri, R. Orlando, and R. Dovesi, "The calculation of the vibrational frequencies of crystalline compounds and its implementation in the CRYSTAL code," *Journal of Computational Chemistry*, vol. 25, no. 6, pp. 888–897, 2004.

[69] C. M. Zicovich-Wilson, F. Pascale, C. Roetti, V. R. Saunders, R. Orlando, and R. Dovesi, "Calculation of the vibration frequencies of Îś-quartz: The effect of Hamiltonian and basis set," *Journal of Computational Chemistry*, vol. 25, no. 15, pp. 1873–1881, 2004.

[70] R. D. King-Smith and D. Vanderbilt, "Theory of polarization of crystalline solids," *Phys. Rev. B*, vol. 47, pp. 1651–1654, Jan 1993.

[71] F. Wang, C. Di Valentin, and G. Pacchioni, "Semiconductor-to-metal transition in wo3-x: Nature of the oxygen vacancy," *Phys. Rev. B*, vol. 84, p. 073103, Aug 2011.

[72] M. Goffinet, P. Hermet, D. I. Bilc, and Ph. Ghosez, "Hybrid functional study of prototypical multiferroic bismuth ferrite," *Phys. Rev. B*, vol. 79, p. 014403, Jan 2009.

[73] A. Prikockyte, D. Bilc, P. Hermet, C. Dubourdieu, and Ph. Ghosez, "First-principles calculations of the structural and dynamical properties of ferroelectric $\mathrm{YMnO_3}$," *Phys. Rev. B*, vol. 84, p. 214301, Dec 2011.

[74] J. Varignon and Ph. Ghosez, "Improper ferroelectricity and multiferroism in $2H$-$\mathrm{BaMnO_3}$," *Phys. Rev. B*, vol. 87, p. 140403, Apr 2013.

[75] N. C. Bristowe, J. Varignon, D. Fontaine, E. Bousquet, and Ph. Ghosez, "Ferromagnetism induced by entangled charge and orbital orderings in ferroelectric titanate perovskites," *Nature Communications*, vol. 6, p. 6677, mar 2015.

[76] S. Tosoni, C. D. Valentin, and G. Pacchioni, "Effect of Alkali Metals Interstitial Doping on Structural and Electronic Properties of WO3," *The Journal of Physical Chemistry C*, vol. 118, no. 6, pp. 3000–3006, 2014.

[77] Y. Ping, D. Rocca, and G. Galli, "Optical properties of tungsten trioxide from first-principles calculations," *Phys. Rev. B*, vol. 87, p. 165203, Apr 2013.

[78] F. Wang, C. D. Valentin, and G. Pacchioni, "Electronic and Structural Properties of WO3: A Systematic Hybrid DFT Study," *The Journal of Physical Chemistry C*, vol. 115, no. 16, pp. 8345–8353, 2011.

[79] D. B. Migas, V. L. Shaposhnikov, V. N. Rodin, and V. E. Borisenko, "Tungsten oxides. I. Effects of oxygen vacancies and doping on electronic and optical properties of different phases of WO3," *Journal of Applied Physics*, vol. 108, no. 9, 2010.

[80] M. N. Huda, Y. Yan, S.-H. Wei, and M. M. Al-Jassim, "Exchange-induced negative-U charge order in N-doped WO_3: A spin-Peierls-like system," *Phys. Rev. B*, vol. 80, p. 115118, Sep 2009.

[81] M. N. Huda, Y. Yan, C.-Y. Moon, S.-H. Wei, and M. M. Al-Jassim, "Density-functional theory study of the effects of atomic impurity on the band edges of monoclinic WO_3," *Phys. Rev. B*, vol. 77, p. 195102, May 2008.

[82] B. Ingham, S. C. Hendy, S. V. Chong, and J. L. Tallon, "Density-functional studies of tungsten trioxide, tungsten bronzes, and related systems," *Phys. Rev. B*, vol. 72, p. 075109, Aug 2005.

[83] R. Chatten, A. V. Chadwick, A. Rougier, and P. J. D. Lindan, "The Oxygen Vacancy in Crystal Phases of WO3," *The Journal of Physical Chemistry B*, vol. 109, no. 8, pp. 3146–3156, 2005.

[84] A. D. Walkingshaw, N. A. Spaldin, and E. Artacho, "Density-functional study of charge doping in WO_3," *Phys. Rev. B*, vol. 70, p. 165110, Oct 2004.

[85] G. A. d. Wijs, P. K. d. Boer, R. A. d. Groot, and G. Kresse, “Anomalous behavior of the semiconducting gap in WO_3 from first-principles calculations,” *Phys. Rev. B*, vol. 59, pp. 2684–2693, Jan 1999.

[86] F. Corá, M. G. Stachiotti, C. R. A. Catlow, and C. O. Rodriguez, “Transition Metal Oxide Chemistry: Electronic Structure Study of WO3, ReO3, and NaWO3,” *The Journal of Physical Chemistry B*, vol. 101, no. 20, pp. 3945–3952, 1997.

[87] F. Corá, A. Patel, N. M. Harrison, R. Dovesi, and C. R. A. Catlow, “An ab Initio HartreeâĹŠFock Study of the Cubic and Tetragonal Phases of Bulk Tungsten Trioxide,” *Journal of the American Chemical Society*, vol. 118, no. 48, pp. 12174–12182, 1996.

[88] A. Hjelm, C. G. Granqvist, and J. M. Wills, “Electronic structure and optical properties of WO_3, $LiWO_3$, $NaWO_3$, and HWO_3,” *Phys. Rev. B*, vol. 54, pp. 2436–2445, Jul 1996.

[89] A. M. Glazer *Acta Cryst. B*, vol. 28, p. 3384, 1972.

[90] P. García-Fernández, S. Ghosh, N. J. English, and J. A. Aramburu, “Benchmark study for the application of density functional theory to the prediction of octahedral tilting in perovskites,” *Phys. Rev. B*, vol. 86, p. 144107, Oct 2012.

[91] W. Cochran, *Structural Phase Transitions and Soft Modes.* Proceedings of the NATO Advanced Study Institute, Universitetsforlaget, 1971.

[92] M. B. Johansson, G. Baldissera, I. Valyukh, C. Persson, H. Arwin, G. A. Niklasson, and L. Österlund, “Electronic and optical properties of nanocrystalline WO 3 thin films studied by optical spectroscopy and density functional calculations,” *Journal of Physics: Condensed Matter*, vol. 25, no. 20, p. 205502, 2013.

[93] P. P. González-Borrero, F. Sato, A. N. Medina, M. L. Baesso, A. C. Bento, G. Baldissera, C. Persson, G. A. Niklasson, C. G. Granqvist, and A. Ferreira da Silva, “Optical band-gap determination of nanostructured WO3 film,” *Applied Physics Letters*, vol. 96, no. 6, pp. –, 2010.

[94] H. Zheng, J. Z. Ou, M. S. Strano, R. B. Kaner, A. Mitchell, and K. Kalantar-zadeh, “Nanostructured Tungsten Oxide – Properties, Synthesis, and Applications,” *Advanced Functional Materials*, vol. 21, no. 12, pp. 2175–2196, 2011.

[95] P. Ghosez, E. Cockayne, U. V. Waghmare, and K. M. Rabe, "Lattice dynamics of BaTiO_3, PbTiO_3, and PbZrO_3: A comparative first-principles study," *Phys. Rev. B*, vol. 60, pp. 836–843, Jul 1999.

[96] F. Detraux, P. Ghosez, and X. Gonze, "Anomalously large Born effective charges in cubic WO_3," *Phys. Rev. B*, vol. 56, pp. 983–985, Jul 1997.

[97] N. A. Benedek and C. J. Fennie, "Why Are There So Few Perovskite Ferroelectrics?," *The Journal of Physical Chemistry C*, vol. 117, no. 26, pp. 13339–13349, 2013.

[98] D. Orobengoa, C. Capillas, M. I. Aroyo, and J. M. Perez-Mato, "*AMPLIMODES*: symmetry-mode analysis on the Bilbao Crystallographic Server," *Journal of Applied Crystallography*, vol. 42, pp. 820–833, Oct 2009.

[99] J. Young, A. Stroppa, S. Picozzi, and J. M. Rondinelli, "Anharmonic lattice interactions in improper ferroelectrics for multiferroic design," *Journal of Physics: Condensed Matter*, vol. 27, no. 28, p. 283202, 2015.

[100] E. Bousquet, M. Dawber, N. Stucki, C. Lichtensteiger, P. Hermet, S. Gariglio, J.M Triscone, and Ph. Ghosez, "Improper ferroelectricity in perovskite oxide artificial superlattices," *Nature*, vol. 452, pp. 732–736, apr 2008. 10.1038/nature06817.

[101] N.A Benedek, J. M Rondinelli, H. Djani, Ph. Ghosez, and Ph. Lightfoot, "Understanding ferroelectricity in layered perovskites: new ideas and insights from theory and experiments," *Dalton Trans.*, vol. 44, pp. 10543–10558, 2015.

[102] D. M. Hatch and H. T. Stokes, "*INVARIANTS*: program for obtaining a list of invariant polynomials of the order-parameter components associated with irreducible representations of a space group," *Journal of Applied Crystallography*, vol. 36, pp. 951–952, Jun 2003.

[103] N. A. Benedek, A. T. Mulder, and C. J. Fennie, "Polar octahedral rotations: A path to new multifunctional materials," *Journal of Solid State Chemistry*, vol. 195, no. 0, pp. 11–20, 2012.

[104] S. Amisi, E. Bousquet, K. Katcho, and Ph. Ghosez, "First-principles study of structural and vibrational properties of $SrZrO3_3$," *Phys. Rev. B*, vol. 85, p. 064112, Feb 2012.

[105] C. F. Pulvari, “Ferrielectricity,” *Phys. Rev.*, vol. 120, pp. 1670–1673, 1960.

[106] J. P. Perdew and A. Zunger, “Self-interaction correction to density-functional approximations for many-electron systems,” *Phys. Rev. B*, vol. 23, pp. 5048–5079, May 1981.

[107] A. D. Becke, “Density functional thermochemistry. III. The role of exact exchange,” *The Journal of Chemical Physics*, vol. 98, no. 7, pp. 5648–5652, 1993.

[108] D. I. Bilc, R. Orlando, R. Shaltaf, G.-M. Rignanese, J. Íñiguez, and P. Ghosez, “Hybrid exchange-correlation functional for accurate prediction of the electronic and structural properties of ferroelectric oxides,” *Phys. Rev. B*, vol. 77, p. 165107, Apr 2008.

[109] Z. Wu and R. E. Cohen, “More accurate generalized gradient approximation for solids,” *Phys. Rev. B*, vol. 73, p. 235116, Jun 2006.